Master Thesis

Hydrogen Propulsion: European Air Quality Along Aviation's Decarbonization Path

Written by **Timothy van der Duim**

Date December 20th 2021

Supervised by Prof. dr. Guus Velders

Second examiner Dr. Aarnout van Delden

Utrecht University

Universiteit Utrecht

Front page background extracted from teahub.io.

Abstract

The aviation sector - projected to double within the next 20 years - currently causes around 16,000 premature deaths globally per year through air pollution. This is mainly attributable to the direct or indirect emission of fine particulates (aerosols, $PM_{2.5}$), nitrogen oxides (NO_x), and ozone (O_3). To reduce aviation's impact on human health, two alternative propulsion techniques are looked at: hydrogen fuel cells - only emitting water - and hydrogen combustion - only emitting water and some NO_x (NO + NO_2). Simulations are performed for northwestern Europe during the first two weeks of June 2019 using the Weather Research and Forecasting Model coupled with chemistry (WRF-Chem). Changes in concentrations of $PM_{2.5}$, NO_2, and O_3 are analyzed based on four different aviation propulsion scenarios of which three involve hydrogen propulsion with varying technical feasibility until 2040, and one represents current (2019) aviation emissions. The model simulations show that current aviation has a limited effect on the air quality averaged over large parts of northwestern Europe. Curbing aviation emissions entirely leads to mean reductions in $PM_{2.5}$, NO_2, and O_3 concentrations of 8.1‰, 5.7‰, and 1.6‰, respectively. However, large air quality differences compared to the 2019 emissions case are seen locally in the vicinity of airports, particularly for NO_2 and O_3. At Eindhoven and Rotterdam-The Hague Airport, the distance from the airport in which concentrations are affected by air traffic is found around 6-7 km. This study shows that for the most promising yet technically feasible hydrogen scenario, the current contributions from aviation to background NO_2, O_3, and $PM_{2.5}$ concentrations are reduced by 57%, 91%, and 72%, respectively. Locations exceeding the 2021 guideline concentrations of the World Health Organization are barely affected between scenarios. For nine out of ten largest airports within northwestern Europe, (partial) hydrogen propulsion leads to reductions in local NO_2 and $PM_{2.5}$ concentrations. The same is observed for O_3 at three out of ten airports, but at the other seven airports, O_3 concentrations increase instead; a dichotomy which is shown to relate to the background ratio of volatile organic compounds and NO_x concentrations.

Acknowledgements

First and foremost, I would like to express my gratitude towards Guus Velders - my thesis supervisor. While leaving me free to develop my own ideas, his commitment, enthusiasm, and constructive criticism have been of great value throughout the research and writing process. Many hurdles had to be overcome, including technical issues and the challenges posed by the COVID-19 pandemic. I would like to thank Guus Velders and Utrecht University for their understanding and flexibility.

Also, I would like to thank my second examiner, Aarnout van Delden, for his willingness to be involved in this project. Another special thanks goes to my fellow student Emma Griffin, who offered modeling guidance and support at the beginning stages of this project. Moreover, I greatly thank my academic peer group chaired by Yo-Yi Pat for the weekly online meetings, the laughs, and the moral support during the long working days at home. To my friend Ardian de Kok, thank you for your careful review of parts of this manuscript, and for the suggestions that ensued.

I would like to emphasize the value of the relentless support of my family and closest friends, without whom I would have not been able to make it to this point. My mom Charlotte, who had to endure my frequent demand for feedback during this project, has been guiding and supporting me with seemingly infinite resilience throughout my entire life. Therefore, this victory is also hers.

This paragraph marks, at the time of writing, the end of my study career, and the start of a new chapter. I would like to finish by thanking all teachers and professors that have been fueling me with knowledge and inspiration over the past years, propelling my personal and professional development while showing me that the sky is the limit.

Contents

List of Symbols and Abbreviations

Abbreviations

Acronym	Description	Unit
ADEP	Airport at departure	[-]
ADES	Airport at destination	[-]
AEED	Aircraft Engine Emissions Databank	[-]
AEM	Advanced Emission Model	[-]
AQG	Air Quality Guideline	[-]
BADA	Base of Aircraft Data	[-]
CAM	Community Atmosphere Model	[-]
CBM-Z	Carbon Bond Mechanism version Z	[-]
CEIP	Centre on Emissions Inventories and Projections	[-]
CRMSE	Centered Root Mean Squared Error	[unit of var.]
d0x	designation of modeled domains (where x is 1, 2, 3, or 4)	[-]
DCMR	Dienst Centraal Milieubeheer Rijnmond	[-]
EEA	European Environment Agency	[-]
EMEP	European Monotoring and Evaluation Programme	[-]
EU	European Union	[-]
FL	Flight Level	[feet/100]
FLEM	FLights and Emission Model	[-]
FOCA	Federal Office of Civil Aviation	[-]
FOI	Swedish Defence Research Agency	[-]
GNFR	Gridding Nomenclature For Reporting	[-]
GOCART	Goddard Chemistry Aerosol Radiation and Transport	[-]
IATA	International Air Transport Association	[-]
ICAO	International Civil Aviation Organization	[-]
IOA	Willmott's Index of Agreement	[-]
KDE	Kernel Density Estimate	[-]
LSM	Land Surface Model	[-]
LTO	Landing and Take-Off	[-]
MACC	Monitoring Atmospheric Composition and Climate	[-]
MAD	Mean Absolute Deviance	[unit of var.]
MBE	Mean Bias Error	[unit of var.]
MM5	Revised Mesoscale Model	[-]
MOSAIC	Model for Simulating Aerosol Interactions and Chemistry	[-]
MOZART	MOdel for OZone And Related chemical Tracers	[-]
NCAR	National Center for Atmospheric Research	[-]
NCEP-FNL	National Centers for Environmental Prediction - FiNaL reanalysis	[-]
NCRMSE	Normalized Centered Root Mean Squared Error	[-]
NMBE	Normalized Mean Bias Error	[-]
NRMSE	Normalized Root Mean Squared Error	[-]
RAP	Radius of Airport Pollution	[km]
PBL(H)	Planetary Boundary Layer (Height)	[m]
RIVM	Rijksinstituut voor Volksgezondheid en Milieu	[-]
RMSE	Root Mean Squared Error	[unit of var.]
POCP	Photochemical Ozone Creation Potential	[-]
RP	Reduction Potential	[%]
Sc$_x$	Designation of scenarios (where x is I, II, III, or IV)	[-]
SNAP	Selected Nomenclature for sources of Air Pollution	[-]
VBS	Volatility Basis Set scheme	[-]

WHO	World Health Organization	[-]
WPS	WRF Pre-processing System	[-]
WRF	Weather Research and Forecasting Model	[-]
WRF-Chem	Weather Research and Forecasting Model coupled with Chemistry	[-]

Chemical names

Formula/Name	**Description**	**Unit**
CH_4	Methane	[μg m^{-3}]
CO	Carbon monoxide	[μg m^{-3}]
CO_2	Carbon dioxide	[μg m^{-3}]
DMS	Dimethyl sulfide	[μg m^{-3}]
H_2	Hydrogen	[μg m^{-3}]
H_2O	Water (vapor)	[μg m^{-3}]
H_2O_2	Hydrogen peroxide	[μg m^{-3}]
H_2SO_4	Sulfuric acid	[μg m^{-3}]
HC	Hydrocarbon	[μg m^{-3}]
HNO_3	Nitric acid	[μg m^{-3}]
HO_2	Hydroperoxyl	[μg m^{-3}]
N_2O_5	Dinitrogen pentoxide	[μg m^{-3}]
NH_3	Ammonia	[μg m^{-3}]
NO	Nitric oxide	[μg m^{-3}]
NO_2	Nitrogen dioxide	[μg m^{-3}]
NO_x	Nitrogen oxides	[μg m^{-3}]
O_2	Oxygen	[μg m^{-3}]
O_3	Ozone	[μg m^{-3}]
OH	Hydroxyl	[μg m^{-3}]
PAN	Peroxyacetyl nitrate	[μg m^{-3}]
PM	Particulate matter	[μg m^{-3}]
$PM_{2.5}$	Fine particulate matter	[μg m^{-3}]
PM_{co}	Coarse particulate matter	[μg m^{-3}]
RO	Alkoxy radical	[μg m^{-3}]
RO_2	Alkyl peroxy radical	[μg m^{-3}]
SO_2	Sulfur dioxide	[μg m^{-3}]
SO_x	Sulfuric oxides	[μg m^{-3}]
VOC	Volatile Organic Compound	[μg m^{-3}]

Mathematical symbols

Symbol	**Description**	**Unit**
η	Normalized pressure level (between 0 and 1)	[-]
σ	Standard deviation	[unit of var.]
d	Radial distance between concentric circles around airport	[km]
n_θ	Number of angular directions in which air quality is assessed	[-]
p_0	Sea-level pressure	[Pa]
p	Pressure level	[Pa]
p_{top}	Pressure level defining the top of modeled domain	[Pa]
r	Radius (from airport)	[km]
R	Pearson's correlation coefficient	[-]
U	Zonal wind velocity	[m/s]
V	Meridional wind velocity	[m/s]

1

Introduction

Since the 1970's, air quality has become a matter of rights within the European Union (EU). Ever since, the "right to clean air" has developed into a set of target concentrations and - legally binding - limit concentrations for air pollutants. Air pollutants include fine particulates ($PM_{2.5}$), nitrogen dioxide (NO_2), and ozone (O_3). They respectively caused 307,000, 40,400, and 16,800 premature deaths within Europe in 2019 according to the European Environment Agency, and are thereby the leading cause of premature deaths of environmental origin [EEA, 2021b; WHO, 2021]. $PM_{2.5}$ - also referred to as aerosol particles - are small particles with a diameter of less than 2.5 μm that are suspended in the air. They are known to impact the central nervous system, the reproductive system, and the respiratory tract upon inhalation, and are associated with e.g. chronic obstructive pulmonary disease (COPD), lung cancer, and cardiovascular diseases [EEA, 2021b]. Exposure to high NO_2 levels is associated with reduced lung functioning and negative impacts on the spleen, liver, and blood (e.g. hemoptysis) [Chen et al., 2018; EEA, 2021b]. High exposure to O_3 - a component of photochemical smog - is being associated with breathing problems and cardiovascular diseases [EEA, 2021b]. Additionally, numerous studies found a relation between exposure to ground-level O_3 and adverse neurological health effects, such as brain diseases, interference with cerebral blood vessels (oxygen intake), and suppression of neurotransmitters like serotonin [e.g. Bernardini et al., 2020; Jung et al., 2015].

New research emphasizes the urgency of compliance with limit concentrations and set the basis for a revised set of air quality guidelines (AQGs), recommended by the World Health Organization (WHO) in 2021 [WHO, 2021]. This is a follow-up on the AQGs from 2005. These updated guideline values are shown in Table 1.1 along with the current EU target and limit values for $PM_{2.5}$, NO_2, and O_3. EEA [2021b] states that if the annual EU limit value for $PM_{2.5}$ (25 μg m^{-3}) would have been reached everywhere in Europe in 2019, the number of $PM_{2.5}$-related premature deaths would not have changed. However, if the newest 2021 WHO guideline $PM_{2.5}$ concentration (5 μg m^{-3}) would have been reached everywhere, the number of premature deaths caused by $PM_{2.5}$ would have been 58% lower. One of the targets stated in EU's Green Deal "Zero pollution action plan" is to reduce the number of premature deaths due to air pollution by 55% in 2030 compared to 2005 [EC, 2021]. Similarly in January 2020, the Dutch government signed an agreement - the "Schone Lucht Akkoord" - with all Dutch provinces and several municipalities [Rijksoverheid, 2020]. In this agreement, the parties declare to strive for compliance with the 2005 WHO AQGs by 2030 to achieve rapid air quality improvements.

A threat to the aforementioned goals is the aviation sector, which is estimated by Yim et al. [2015a] to cause around 16,000 premature deaths a year globally. Aviation contributes mainly to air pollution by the direct emission of fine particulates (e.g. soot) and nitrogen oxides (NO_x[1]), the latter also being a precursor of ozone and nitrate aerosols. Sulfuric oxides (SO_x) and organic compounds[2] are also emitted, contributing to the formation of secondary aerosols and ozone through chemical processes in the atmosphere [Lee et al., 2021].

[1] NO_x is the sum of nitric oxide (NO) and nitrogen dioxide (NO_2).
[2] Most carbon-containing compounds are organic compounds.

Table 1.1. Overview of the 2021 WHO air quality guideline levels and the 2008 EU air quality limit values. Units are in micrograms of the pollutant per cubic meter of air (μg m^{-3}). Values are based on WHO [2021] and EEA [2021c].

		WHO	EU
$PM_{2.5}$	*Annual*	5	25[3]
	24 hours[4]	15	-
NO_2	*Annual*	10	40[3]
	24 hours[4]	25	-
	1 hour	-	200[3]
O_3	*8 hours*[5]	100	120
	Peak season[6]	60	-

EASA, EEA and EUROCONTROL [2019] report a 7% contribution of air traffic NO_x emissions to total NO_x emissions in Europe for the year 2015. Global air traffic movements have more than doubled between 2000 and 2019 [Airbus, 2019]. The International Civil Aviation Organization (ICAO) projects an average annual growth rate of 4.3% for the aviation sector in the coming 20 years [Fleming and De Lépinay, 2019]. This is opposed to a 1.16% per annum reduction in NO_x emissions per passenger-kilometer in ICAO's most optimistic technology and operational improvement scenario. In its best-estimate scenario, EUROCONTROL [2019] projects an annual growth rate of 1.9% for the aviation sector within European airspace in the coming 20 years. This is well below the global projection by the ICAO, but still implies a 50% increase in demand within 20 years. Additionally, aviation growth over the past decades showed strong resilience to external crises, e.g. the 1979 oil crisis and the 2008 financial crisis. It is considered likely that aviation's share in total anthropogenic emissions will increase in time - and thereby also aviation's share in air pollution and associated mortality - that is, if no action is undertaken.

This study focuses on the potential effect on air quality when replacing current air traffic propulsion techniques - based on fossil fuels - by hydrogen (H_2) propulsion techniques. H_2 is considered one of the most promising sustainable aviation fuels [FCH JU, 2020]. Flying on H_2 fuel is no science fiction, as the first aircraft on H_2 - the Tupolev Tu-155 - already entered into service in 1988 but was later taken out of service. Recently, ZeroAvia announced its plan to offer the first commercial flight powered by H_2 fuel between Rotterdam and London in 2024 [ZeroAvia, 2021]. Major challenges related to H_2 propulsion are the higher flammability and higher pressurization requirements, as well as the lower volumetric energy density (energy per unit volume) compared to currently used fuels which are kerosene-based [FCH JU, 2020]. This requires major modifications to currently flying air vehicles, including more fuel storage space and an adapted propulsion architecture. FCH JU [2020] presents two H_2 propulsion techniques: H_2 combustion and H_2 fuel cells, both having their advantages and disadvantages. Airbus' ZEROe concept is an example of a hybrid concept, combining H_2 combustion with fuel cells, to power a commercial aircraft with H_2 by 2035 [Airbus, 2020a].

Changes in $PM_{2.5}$, NO_2, and O_3 concentrations - referred to in this study as changes in air quality - between different aviation emission scenarios are studied. Those scenarios involve H_2 propulsion techniques. The aim is to quantify changes in air quality along a technically feasible decarbonization path for the aviation sector. This is done for northwestern Europe during two weeks in June 2019. The following research questions are formulated for this study:

- What is the short-term effect on European air quality of short-haul flights on H_2 fuel cells?
- What is the additional short-term effect on European air quality of medium and long-haul flights on H_2 combustion?

[3] Legally binding (limit value), not to be exceeded more than 18 hours per year for the hourly NO_2 limit [EEA, 2021c].
[4] 3-4 exceedances are allowed on a yearly basis (99th percentile) [WHO, 2021].
[5] The 8-hour guideline is defined as the maximum 8-hour mean concentration during the day. 3-4 exceedances are allowed on a yearly basis (99th percentile) for the WHO value and a 3-year average of 25 exceedances per year are allowed for the EU value (target value) [EEA, 2021c; WHO, 2021].
[6] The peak season is defined by the WHO as the "*average of daily maximum 8-hour mean O_3 concentrations in the six consecutive months with the highest six-month running-average O_3 concentration.*" [WHO, 2021].

- What is the effect of different aviation emission scenarios on the number of locations above WHO guideline concentrations?
- How do local changes in air quality around airports relate to overall changes in air quality between scenarios?

Chapter 2 elaborates more on 1) the environmental impact aviation currently has by discussing individual atmospheric compounds emitted by the sector, and 2) the implications on those emissions when using one of the H_2 propulsion technologies. The Weather Research and Forecasting Model, coupled with chemistry (WRF-Chem), is used to model changes in air quality. Even though the climatological impact of aviation is not explicitly assessed in this study, WRF-Chem incorporates the interplay between meteorology and chemistry. A description of the WRF-Chem model is given in Chapter 3. To quantify current aviation emissions on a high spatial and temporal resolution, data sets on flight movements are processed and used as an input for the Advanced Emission Model provided by EUROCONTROL [2021a]. Assumptions on the emissions when flying on H_2 fuel cell technology and H_2 combustion are applied to generate scenario-dependent data sets. More on the used methodology for this study is presented in Chapter 4. In Chapters 5 and 6 the modeling results and evaluation/validation are presented, respectively.

2

Research Background - Aviation and its Environmental Impact

Emissions from the aviation sector are the focus of this study. This chapter provides some context to air traffic emissions, currently resulting mainly from the combustion of kerosene-based jet fuels (see Section 2.1). Section 2.2 addresses the emissions using hydrogen as fuel, which is presented in this study as a feasible air pollution mitigation pathway by replacement of kerosene-based fuels.

2.1. Emissions from Conventional Jet Fuels

The vast majority of recent air traffic is propelled by combustion of petroleum-based fuels. Accordingly, pollutants coming from air traffic propulsion coincide closely with road transport emissions originating from e.g. cars [FAA, 2005]. Air traffic engine types can be divided into turboprop, turboshaft, turbofan, and piston engines, where the turbofan engines (see Figure 2.1) lead the market with a share of 71% in 2019 - a share that is expected to increase even further [FBI, 2020]. While piston engines are particularly operated using gasoline, turboprop, turboshaft, and turbofan engines are mainly operated using kerosene-based jet fuel. In the EU, more than 99% of currently used aviation fuels are kerosene-based [EC, 2019]. Those fuels are a mixture of various hydrocarbons (both saturated and unsaturated), sulfuric compounds, and additives such as corrosion inhibitors, which combine to a fit-for-purpose jet fuel [ATSDR, 1995].

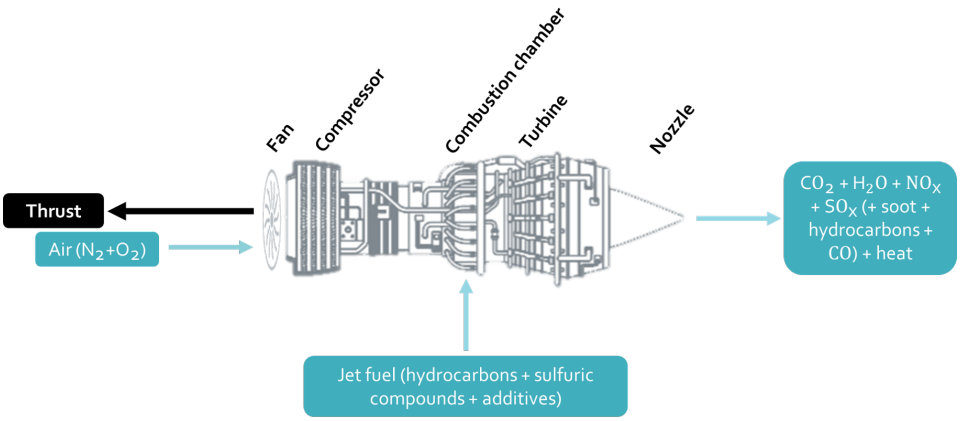

Figure 2.1. The workings of current kerosene-based jet fuel combustion in a turbofan engine. Air containing oxygen (O_2) and nitrogen (N_2) enters the gas turbine at the fan, after which it is compressed, mixed with jet fuel and combusted. The exhaust gases flow through the turbine - which drives the fan through a shaft - and are expelled at the nozzle, generating thrust. The exhaust gases contain carbon dioxide (CO_2), water vapor (H_2O), nitrogen oxides (NO_x), sulfuric oxides (SO_x), and in case of incomplete combustion also soot particles, hydrocarbons, and carbon monoxide (CO). Turbofan cross section from Roland Berger [2020].

Combustion of kerosene-based fuels results in the release of carbon dioxide (CO_2), nitrogen oxides (NO_x), water vapor (H_2O), and sulfuric oxides (SO_x), as shown in Figure 2.1 [Lee et al., 2009]. In the case of incomplete combustion, carbon monoxide (CO), hydrocarbons (HCs) or volatile organic compounds (VOCs), particulate matter (PM), and some other trace compounds are also being emitted [FAA, 2005]. Incomplete combustion occurs mainly at low engine settings when sub-optimal fuel-air mixing ratios occur [IPCC, 1999]. PM or aerosols, originating from the combustion of aviation fuels, are fine particles - either solid or liquid - suspended in air, and could be either of primary (directly emitted) or secondary (formed within the atmosphere after being emitted) nature. Primary PM consists mainly of soot, also called black carbon. NO_x emissions occur mostly during high thrust settings and are strongly influenced by the flame temperature and pressure in the combustion zone [EC, 2020; Schaefer and Bartosch, 2013]. Air traffic emissions are generally composed of about 70% CO_2, 25%-30% H_2O, and the remaining few percents of the other mentioned compounds [FAA, 2005].

The impact of aviation on the atmosphere is a complex conjunction of on one side the direct (instantaneous) emissions, and on the other side a combination of plume dynamics, microphysics and chemical reactions, radiation, and transport [Lee et al., 2021]. The main compounds emitted by aviation are shown in the high-level flow chart from Figure 2.2, together with the principal way in which they affect the atmospheric composition and the principal atmospheric processes that are involved. The purpose of this study is to determine changes in air quality. This mainly involves the compounds and atmospheric processes that are emphasized in Figure 2.2, encircled by solid lines. Radiative forcing is not explicitly assessed in this study, but due to its relation with meteorology it does affect chemistry, and thereby also air quality. The coupling between meteorology and chemistry is incorporated into this study as is further explained in Chapter 3. An explicit assessment of aviation's influence on radiative forcing is left as a recommendation for future work. As the focus lies on air quality (relating to health effects) and the study should be kept within computational time limits, the temporal study domain involves a short time scale of two weeks. Accordingly, methane (CH_4) and CO_2 are not considered in this study as is explained in Section 2.1.1 and 2.1.2, respectively. Furthermore, model limitations lead to the exclusion of H_2O in this study as will be further explained in Chapter 4. Contrails and clouds affect radiative forcing and are thus not explicitly focused on. The emitted compounds together with the involved atmospheric processes and changes in atmospheric composition will be briefly discussed below.

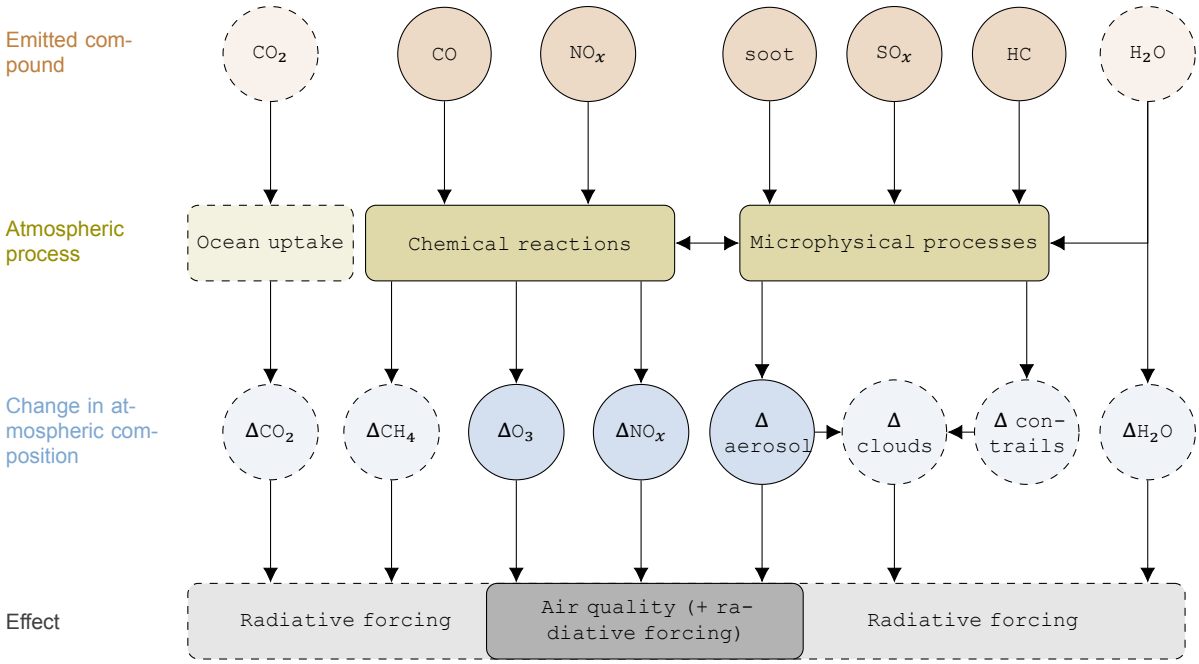

Figure 2.2. Generic flow chart of main pollutants from air traffic, and the atmospheric processes leading to changes in meteorology and chemical atmospheric composition. The dashed, light-colored nodes are ignored in this study. Modified from Lee et al. [2009].

2.1.1. Nitrogen Oxides

The nitrogen species that are emitted by current air traffic are nitric oxide (NO) and nitrogen dioxide (NO_2), where NO is the main emission source resulting from combustion. NO_x represents the sum of NO and NO_2. NO_x species play a central role within this research as they are relatively short-lived, chemically reactive gases that impair human health in various ways. Indirectly they also affect air quality, e.g. by the production/destruction of ozone (O_3). Besides having a strong warming potential, tropospheric O_3 belongs to one of the main air pollutants as it impairs plant growth and has a detrimental effect on the respiratory tract [Seinfeld and Pandis, 2016]. NO_x is also one of the main precursor gases in the formation of secondary inorganic aerosols, through its conversion to nitrate aerosols [Stocker et al., 2013]. Secondary inorganic aerosols dominate the presence of particulate matter (PM) in the Netherlands [Weijers et al., 2012]. NO_x concentrations are highly variable in space and time. Any local emissions can cause local changes in air quality (and radiative forcing) on short timescales. Emission effects of NO_x on longer time scales include changes in the lifetime of CH_4 (which is in the order of 10-12 years), as NO_x enhances the atmospheric concentration of the hydroxyl radical (OH), a major sink of CH_4 [Ponater et al., 2006; Seinfeld and Pandis, 2016]. Lee et al. [2009] states that this reduction in CH_4 atmospheric lifetime induces a small negative radiative forcing term in the radiative forcing budget. As this effect is expected to be seen on time scales in the order of years, this study does not focus on this aspect.

The principal formation of NO_x is the dissociation and subsequent reaction of nitrogen (N_2) and oxygen (O_2) contained in the air under influence of high temperature and pressure during combustion, which forms NO [EC, 2020]. However, the ratio between NO and NO_2 emissions from air traffic engine combustion is highly dependent on the combustor efficiency and power/thrust setting. Modern high by-pass turbofan engines with high combustor efficiencies operating in idle (< 10% thrust output) emit relatively more NO_2 [Masiol and Harrison, 2014]. NO emissions are favored during high-temperature combustion, i.e. at higher thrust settings. Measurements performed at sea-level show that for low engine thrust settings, total NO_x emissions can constitute up to 80% of NO_2 while for maximum thrust settings this could be merely 7% [Wormhoudt et al., 2007]. In a different study, measurements during taxi and take-off showed a contribution of NO_2 to total NO_x of around 30% [Herndon et al., 2004]. Uncertainties remain high due to rapid chemical reactions in the emitted plume in which NO can be converted to NO_2.

Globally, NO_x emissions from aviation are estimated at ~1.4 Tg N for the year 2018, roughly 3% of total anthropogenic NO_x emissions [EC, 2020]. For Europe, EASA, EEA and EUROCONTROL [2019] estimate a 7% contribution of aviation to anthropogenic NO_x in 2015. Even though NO_x emissions from aviation are currently lower than NO_x emissions from other large transportation modes (shipping and road traffic), aviation is responsible for the largest O_3 perturbation of all transportation modes [Hodnebrog et al., 2012]. This is due to the higher atmospheric lifetime of NO_x at higher altitudes, combined with higher O_3 concentrations in the upper troposphere compared to the lower troposphere, increasing the efficiency of catalytic O_3 transformation by NO_x [Hoor et al., 2009; KNMI, 2007].

The interconversion between NO and NO_2 occurs rapidly and reaches a steady state in the order of minutes. It involves a photochemical cycle in which O_3 is being produced (reaction 2.1b) and subsequently removed through reaction with NO. The chemical (chain) reactions presented in this chapter are based on Seinfeld and Pandis [2016].

$$NO_2 + h\nu \longrightarrow NO + O \tag{2.1a}$$

$$O + O_2 + M \longrightarrow O_3 + M \tag{2.1b}$$

$$O_3 + NO \longrightarrow NO_2 + O_2 \tag{2.1c}$$

Here $h\nu$ in reaction 2.1a indicates a (light) photon which has been absorbed by the NO_2 molecule to dissociate into NO and a single oxygen atom. ”M” in reaction 2.1b denotes an air molecule to which the excess energy upon collision between O and O_2 is lost - again upon collision - to form the reaction product. During nighttime, a lack of photons causes removal of NO_2 (reaction 2.1a) to stagnate while

O_3 keeps removing NO and converting this to NO_2 (reaction 2.1c). Therefore, almost all NO_x is in the form of NO_2 at nighttime.

Within this null cycle, no net O_3 or net NO_x is produced or destroyed. The principal removal of NO_x is the reaction with the hydroxyl radical (OH), which could form the reservoir species nitric acid (HNO_3), see reaction 2.2. Dinitrogen pentoxide (N_2O_5) and other reservoir species such as peroxyacetyl nitrate (PAN) can also be formed.

$$OH + NO_2 + M \longrightarrow HNO_3 + M \tag{2.2}$$

2.1.2. Carbon Oxides and Volatile Organic Compounds

The carbon oxides contained in the exhaust of air traffic engines are carbon monoxide (CO) and carbon dioxide (CO_2). CO_2 is unreactive and does therefore not affect atmospheric chemistry. Furthermore, background concentrations are high compared to the magnitudes emitted by aviation. The possible effect of changes in CO_2 emissions on air quality (through meteorological changes) can therefore only be seen on longer timescales than just a couple of weeks. Changes in CO_2 emissions by aviation are ignored in this study.

CO on the other hand results from incomplete combustion. It has an average tropospheric lifetime between 30 and 90 days [Seinfeld and Pandis, 2016]. Despite its average lifetime being longer than the temporal domain of this study, it is still discussed here together with volatile organic compounds (VOCs) because of their role in O_3 formation - one of the main air pollutants that is considered in this study.

Local tropospheric O_3 production is dominated by local atmospheric composition and short-scale chemistry. In the production of O_3, the OH radical plays a key role. CO and VOCs are, in combination with the previously discussed NO_x, one of the principle precursors of tropospheric O_3. VOCs are a collection of many carbon-containing compounds that easily evaporate (high vapor pressure). Many hydrocarbons (HCs) are VOCs. The hydroperoxyl radical, HO_2, is produced by oxidation of CO and VOCs. VOCs have a shorter lifetime than CO, which varies depending on the compound from a couple of hours to a couple of days. For CO, the oxidation reaction whereby a single hydrogen atom gets rapidly oxidized by O_2 is shown in reaction 2.3:

$$CO + OH \xrightarrow{O2} CO_2 + HO_2 \tag{2.3}$$

Hydrocarbon species also result from incomplete combustion and include species as toluene, xylene, and benzene. Considering a hydrocarbon (RH) as VOC, a similar reaction leads to alkyl peroxy radicals (RO_2). Those react with NO, creating an alkoxy radical (RO) which finally reacts with O_2 to produce HO_2.

$$RH + OH \xrightarrow{O2} H_2O + RO_2 \tag{2.4a}$$

$$RO_2 + NO \longrightarrow RO + NO_2 \tag{2.4b}$$

$$RO + O_2 \longrightarrow R'CHO + HO_2 \tag{2.4c}$$

In the presence of high NO_x concentrations, HO_2 reacts with NO to produce NO_2:

$$HO_2 + NO \xrightarrow{O2} NO_2 + OH. \tag{2.5}$$

Otherwise, when NO concentrations are low, HO_2 favors reaction with itself rather than with NO, by which a reservoir species, hydrogen peroxide (H_2O_2), is formed:

$$HO_2 + HO_2 \longrightarrow H_2O_2 + O_2. \tag{2.6}$$

The produced NO_2 molecule from reaction 2.5 is photolyzed and converted into an O_3 molecule as shown in reaction 2.1, which boils down to a net O_3 production cycle as no O_3 was required in the reaction of HO_2 earlier in the reaction chains.

While scaling linearly with CO concentrations, O_3 production is inversely proportional to NO_2 concentrations when termination reaction 2.2 dominates reaction 2.3; that is, when NO_x concentrations are significantly higher than CO concentrations. This can be explained by the looking at reaction 2.2. Increasing NO_x concentrations - where there already is NO_x present in abundance - increases the reaction rate of reaction 2.2 whereby both OH and NO_x are removed. This means there is less OH left to react with CO to form HO_2 (reaction 2.3) and eventually O_3. Restricting reaction 2.5 to happen inhibits the regeneration of the OH radical that keeps the oxidation cycle (and O_3 production) going. Increasing NO_x concentrations when NO_x concentrations are low results in longer OH cycles until an optimum is reached, after which OH is depleted again as NO_2 get so high that termination reaction 2.2 takes over again.

Within the context of VOCs, the VOC-OH reaction (reaction 2.4) has to compete with reaction 2.1c, which has a reaction rate constant about 5.5 times[1] higher than the VOC-OH reaction. Therefore, VOCs should be much more abundant than NO_x for the VOC-OH reaction to be favored, yielding O_3 production. The so-called VOC/NO_x ratio therefore plays an important role in O_3 formation. Generally stated, a decrease in NO_x concentrations in a VOC-limited (NO_x-limited) environment leads to an increase (decrease) in O_3 concentrations. The exact threshold which separates the VOC-limited from the NO_x-limited regime depends on the combination of VOCs considered. The dynamical response of O_3 formation to changes in NO_x and VOC concentrations are relevant for this study as O_3 is one of the main air pollutants, and aviation affects both atmospheric NO_x and VOC concentrations.

2.1.3. Soot, Sulfuric Oxides and Hydrocarbons

Soot (also called black carbon), sulfuric oxides (SO_x), and hydrocarbons (HCs) are discussed in conjunction as they are all particularly involved in microphysical processes resulting in aerosols or PM. Both soot and hydrocarbon emissions result from incomplete combustion of kerosene-based fuels.

SO_x, in the case of aircraft emissions nearly all in the form of sulfur dioxide (SO_2), forms by mixing of sulfur - an element found in fossil fuels - with oxygen during combustion [Kurniawan and Khardi, 2011]. Global sulfur emissions from aviation are estimated around 0.2 Tg S yr^{-1}, ~0.4% of total anthropogenic sulfur emissions [EC, 2020]. SO_2 plays part in the formation of sulfate aerosols, which are mainly composed out of sulfuric acid (H_2SO_4) and have a general cooling effect on climate due to their reflectivity of incoming solar energy [Lee et al., 2009; Rao et al., 2020; Von Glasow and Crutzen, 2014]. Dimethyl sulfide (DMS) is the principal precursor of H_2SO_4, but as it has a biogenic source it is not further addressed. The dominant reaction of gaseous SO_2 is with the hydroxyl radical (OH), which in the presence of water vapor (H_2O) produces H_2SO_4 through reaction scheme 2.7:

$$SO_2 + OH + M \longrightarrow HOSO_2 + M \tag{2.7a}$$

$$HOSO_2 + O_2 \longrightarrow HO + SO_3 \tag{2.7b}$$

$$SO_3 + H_2O + M \longrightarrow H_2SO_4 + M. \tag{2.7c}$$

The lifetime of SO_2 through reaction with the hydroxyl radical is approximately one week, indicating the fast reaction rate of reaction 2.7. This also the reason why the effect of SO_2 emissions on $PM_{2.5}$ concentrations and hence on air quality are expected to be seen on short timescales, and accordingly why those emissions are incorporated in this study.

The principal influence of soot and organic compounds, such as non-methane hydrocarbons, on radiative forcing is through their function as cloud condensation nuclei [Lee et al., 2009]. Water vapor can condense onto those cloud condensation nuclei to eventually form (in this case aviation-induced) clouds [Lee et al., 2009]. Besides its influence on cloud formation - which affects the radiative balance on Earth and thereby indirectly influences chemistry - those suspended particles form aerosols which

[1] This value varies depending on the exact composition of VOCs, but an average VOC mix yields 5.5.

may affect human health when residing near the surface. Finally, soot particles are associated with a small direct warming effect due to their high absorptivity, even though the scientific confidence level is low [EASA, EEA and EUROCONTROL, 2019; IPCC, 1999; Lee et al., 2009].

2.1.4. Water (Vapor)

Water - either in gaseous or liquid form - is, after CO_2, the most abundant species in aircraft exhaust plumes from kerosene combustion. Its emission scales linearly with fuel consumption, for which an emission factor of ~1.23 kg per kg of fuel applies [Lee et al., 2009; Schumann, 2002]. Water vapor is a greenhouse gas, whose direct impact on radiative forcing is highly dependent on the altitude at which it is emitted. Having a longer residence time at higher altitudes, the climatological impact of water vapor emissions during cruise phase is higher due to more accumulation [Rao et al., 2020; Schumann, 2002]. Various studies indicate that the direct effect of water vapor emissions on radiative forcing is small, or even negligible. The radiative forcing effect is about a factor of 10 (5) smaller than that of CO_2 (NO_x), as most water vapor is emitted in the troposphere where the emitted water vapor is quickly removed [Lee et al., 2009].

Another, more pronounced effect in which water vapor emissions are involved is in the formation of contrails, which may result in aircraft-induced clouds when persisting in the atmosphere. Soot particles and aerosols - that are either already present in the atmosphere or emitted by aircraft - work as condensation nuclei on which water vapor can condense to form aircraft-induced clouds or contrails. Even though there are strong indications that contrails and aircraft-induced clouds have a rather strong positive contribution to aircraft-induced radiative forcing, estimates are still highly uncertain [Lee et al., 2009]. Both the direct and indirect effects of water vapor on radiative forcing are local and take place on a timescale of days or less within the troposphere. Varying H_2O concentrations could affect air quality through its effect on meteorology (changes in cloud dynamics and temperatures), but these effects are considered to be small. Regardless, model limitations restrict the possibility to include H_2O in this study (see Chapter 4).

2.2. Emissions from H_2 Propulsion

Currently, two major implementations of hydrogen (H_2) as fuel in aviation are considered in industry: the use of H_2 fuel cells and the combustion of H_2 [FCH JU, 2020]. The discussion on technical, practical and financial implications of such implementations in aviation industry are out of the scope of this study. This study rather focuses on the environmental aspect of "flying on hydrogen", whereby the feasibility of such industry-wide transitions are reflected into the emission scenarios discussed in Section 4.4. Related changes in flight duration, flight frequency, and other operational considerations such as changes in flight levels are also neglected as uncertainties are currently too high. This section will briefly go into emissions resulting from fuel cell-based propulsion and H_2 combustion-based propulsion as both have distinct emission characteristics.

2.2.1. H_2 Fuel Cells

In a fuel cell-powered aircraft, the fuel cells are responsible for converting H_2 into electricity, which is then used to drive a fan or propeller to propel the air vehicle. The way a H_2 fuel cell works is illustrated in Figure 2.3a. Hydrogen enters through an anode, where the positively charged ions (protons) are separated from the negatively charged ions (electrons) through a catalytic reaction. On the cathode side, pure oxygen from the ambient air enters. The protons migrate through an electrolyte membrane. The electrons are forced to go around through an external circuit to reach the cathode, whereby an electric current is created. This electric current is then used to either charge a battery which drives an electric motor, or to directly drive an electric motor. This electric motor in turn drives a propeller or fan, creating thrust. At the cathode, the protons combine with the oxygen to create the waste product - water. The entire process is shown in Figure 2.3b.

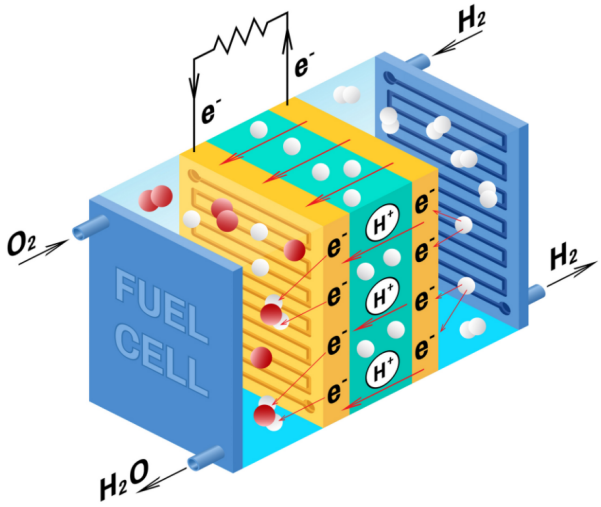

(a) Retrieved from Airbus [2020b].

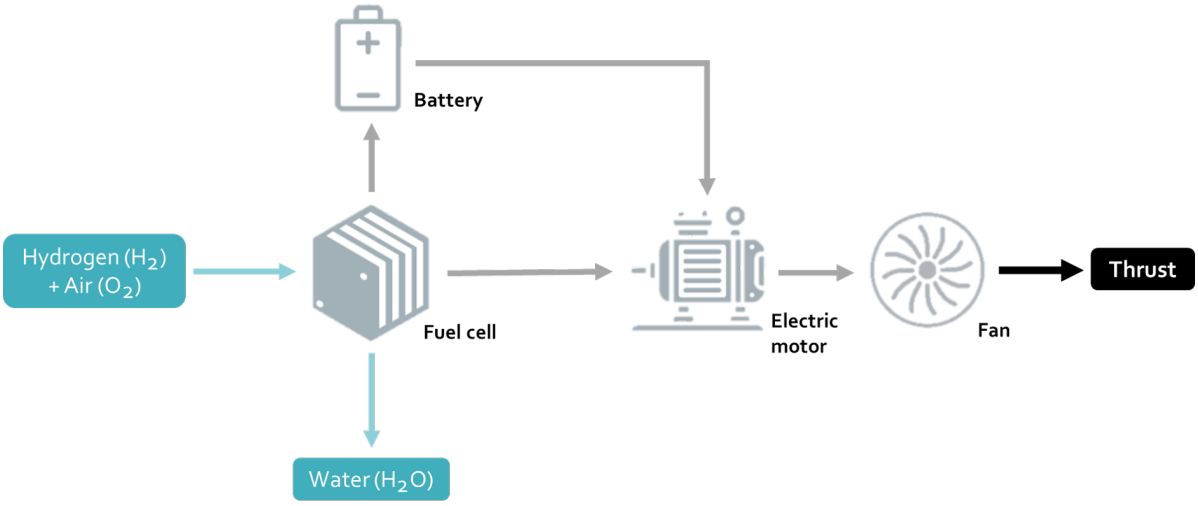

(b) Adjusted from Roland Berger [2020].

Figure 2.3. **(a)** The workings of a H_2 fuel cell and **(b)** the way this fuel cell is used in the propulsion architecture to create thrust.

The use of H_2 (and ambient air) to produce electricity from which the propulsion system is driven, eliminates the emission of carbonaceous compounds. Thereby the assumption is made that the production of H_2 is done in a ”green” way, i.e. without carbon emissions. Comparing fuel cell systems with the combustion products of kerosene-based fuels shown in Figure 2.1, CO_2, CO, soot, and HCs are not being emitted when using fuel cells. The absence of sulfur in H_2 furthermore eliminates SO_x emissions. The nitrogen component of nitrogen oxides is extracted from the air itself rather than being contained in carbon-based fuel. However, as fuel cells do not rely on combustion processes, no NO_x is emitted either. The only compound emitted in case of fuel cells is water vapor (H_2O). H_2-fueled air traffic would emit 2.55 times as much H_2O compared to kerosene fleets [FCH JU, 2020; Gauss et al., 2003]. The zero-carbon solution therefore does not provide a true-zero solution to in-flight climatological impact, as the emission of H_2O could still contribute to direct radiative forcing and indirect forcing through cloud formation. The high emission factor of H_2O for H_2-fueled air traffic would theoretically lead to more contrails and aircraft-induced clouds. However, research indicates the opposite might be true, as the number of nucleation sites which initiate ice crystal formation are reduced by constraining the emission of soot and other aerosol particles [Burkhardt et al., 2018]. Furthermore, the optical depth of existing contrails would likely be lower in the absence of aircraft-induced aerosols [Burkhardt et al., 2018; Lee et al., 2009]. Water emitted by H_2-fueled air traffic would merely condense onto ambient aerosol particles entrained into the exhaust plume, causing ice crystals that are smaller in number but larger in size, decreasing the optical depth and thereby lowering the radiative impact [Schumann, 2002]. The net ef-

fect on the contrail radiative forcing term remains uncertain, just as for kerosene-based fuels. FCH JU [2020] reports that the overall reduction in climate impact by using H_2 fuel cells would be 75%-90%, and potentially even higher if water vapor emissions can be conditioned [FCH JU, 2020]. Disregarding the potential effect on air quality via radiative forcing and via the atmospheric residence time of aerosols, the H_2 fuel cell technique has a true zero impact on air quality.

2.2.2. H_2 Combustion

H_2 combustion relies on the same concepts as currently used propulsion techniques where a fuel is being combusted with ambient air. In the case of H_2 combustion, H_2 is directly burned in a combustion chamber, where the combustion gases drive a turbine and are expelled, creating thrust, see Figure 2.4. As for fuel cell systems, the replacement of carbon-based fuels with H_2 eliminates any emission of carbonaceous or sulfuric compounds while enhancing the emission of H_2O. However, as the process involves combustion of a mixture with ambient air, the created combustor gases do contain nitrogen oxides. NO_x emissions resulting from a combustion process depend on the temperatures involved as stated before. As H_2 has a broader flammability range compared to kerosene, lower flame temperatures can be achieved, reducing NO_x emissions [FCH JU, 2020]. Also, faster fuel-air mixing and higher reaction rates increase the efficiency, again reducing NO_x emissions. FCH JU [2020] estimates that the NO_x emissions resulting from H_2 combustion are 65% lower than for the kerosene counterpart. Despite the large NO_x reduction compared to kerosene-based jet fuel combustion, NO_x emissions are a major drawback of H_2 combustion compared to H_2 fuel cells.

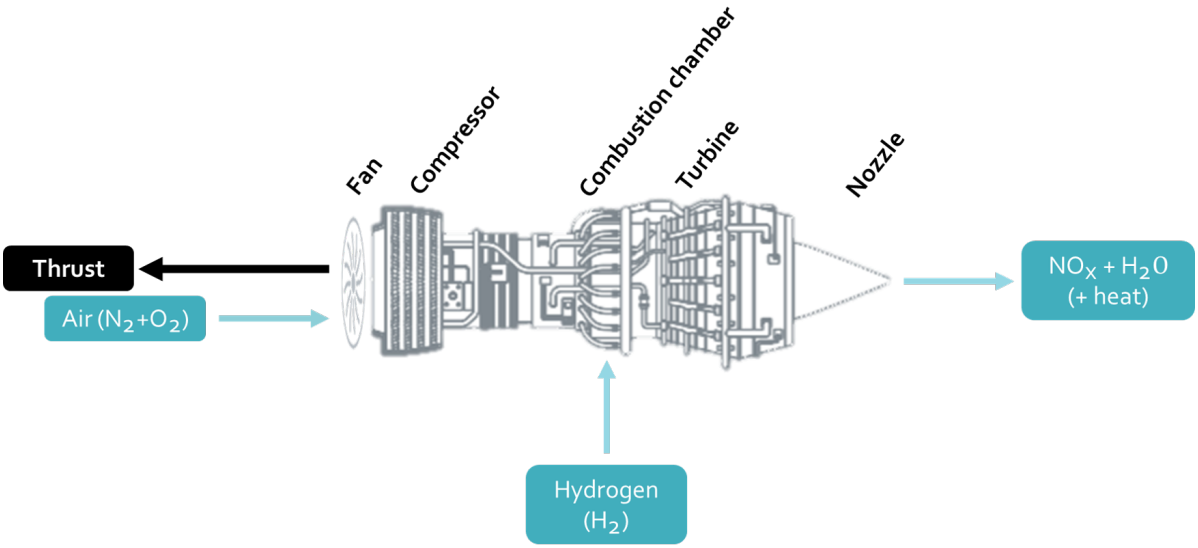

Figure 2.4. The workings of H_2 combustion. Air containing oxygen (O_2) and nitrogen (N_2) enters the gas turbine (turbofan engine) at the fan, after which it is compressed, mixed with hydrogen (H_2) and combusted. The exhaust gases flow through the turbine - which drives the fan through a shaft - and are expelled at the nozzle, generating thrust. The exhaust gases contain nitrogen oxides (NO_x) and water vapor (H_2O). Adjusted from Roland Berger [2020].

3

WRF-Chem Model Setup

The Weather Research and Forecasting model, coupled with chemistry (WRF-Chem, version 3.8.1), is used in this study to assess changes in air quality due to changes in emissions from aviation [Skamarock et al., 2008]. A brief description of the WRF-Chem model is provided in Section 3.1, based on Skamarock et al. [2008], followed by details on the study domain (Section 3.2). The configuration of WRF-Chem for this study is presented in Section 3.3, and this chapter ends by describing the handling of initial and boundary conditions for the study domain in Section 3.4.

3.1. Model Description

WRF-Chem is a fully compressible, non-hydrostatic model that solves explicitly for meteorological fields and that can therefore be used for real-time forecasting. The model could run without the chemistry component (referred to as WRF). However, by including the chemistry component, research possibilities related to atmospheric chemistry open up. The interdependence between meteorology and chemistry is captured by WRF-Chem by concurrently solving for both meteorology and chemistry, while incorporating processes such as photolysis, transport, deposition, absorption, radiation, and aerosol forcing effects. This configuration, whereby both gas-phase chemistry and aerosol mechanisms are included, provides an all-encompassing simulation model for the study of air quality (and meteorology) given different anthropogenic emission inputs. Furthermore, the WRF core incorporates topography effects, soil types, and other geographical variables into the simulations.

The potential of WRF-Chem to accurately reproduce the evolution of chemical concentrations and meteorology has been demonstrated in a large number of conducted studies, by comparing the output with satellite and in-situ observations. An example is Yerramilly et al. [2012] in a study on O_3 pollution in the Central Gulf Coast, or Sicard et al. [2021] where spatio-temporal variability on meteorological and chemical variables such as temperature, NO_2, and O_3 was researched on complex terrain in China.

A high-level system breakdown of the WRF-Chem model is shown in Figure 3.1 as used for this study. The WRF pre-processing system (WPS) uses terrestrial and meteorological data to generate domain-specific and time-specific meteorology input files that are used as input for the WRF-Chem core module. To process meteorological data, the newest version of the WPS system at the time of writing - V4.3 - is used. Real.exe generates domain-specific files in which data on chemistry, meteorology, and geography are aggregated. Those files prescribe initial and boundary conditions - see Section 3.4 - and provide the meteorology files used for nudging practises, see Section 3.3.2. Anthropogenic emission data - see Chapter 4 - are read in during the execution of the core module wrf.exe. Note that WRF-Chem provides many more options and modules than the ones shown in Figure 3.1, including the possibility to provide additional emission data (e.g. from biogenic sources, volcanic ash or fire). See Skamarock et al. [2008] for more information.

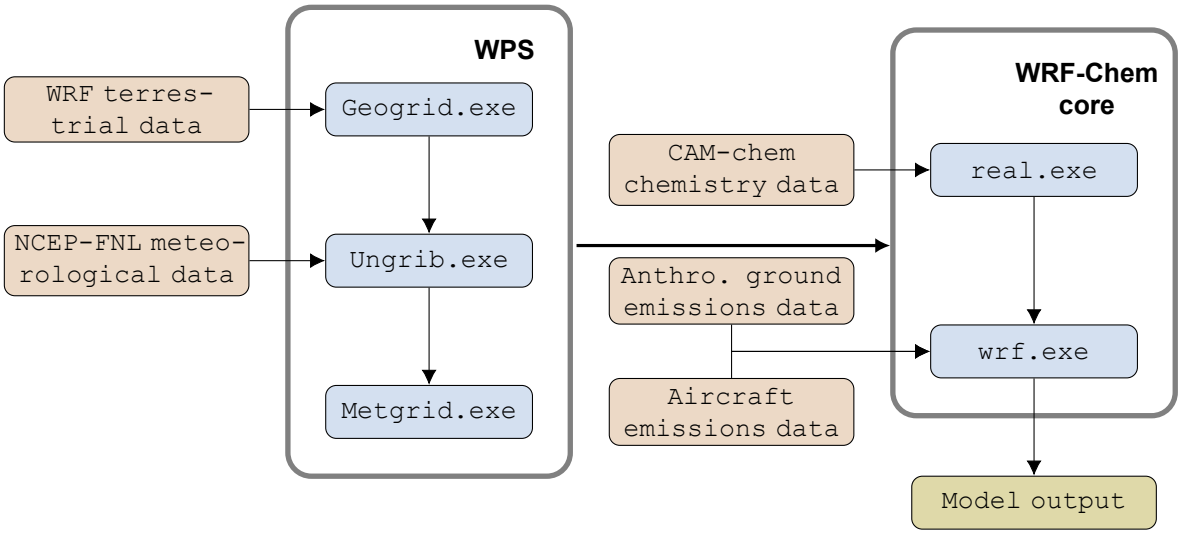

Figure 3.1. Flow chart showing the main subsystems of WRF-Chem and inputs provided to the model. Modified from Skamarock et al. [2008].

3.2. Spatial and Temporal Modelling Domain

For 2019, the ICAO reports a share of 26.8% for Europe in terms of global revenue passenger-kilometers[1] flown [ICAO, 2019]. This, combined with Europe's relatively small land area and high population density in the northwestern part of the continent, emphasizes the need to research aviation's impact on European air quality and potential mitigation pathways. This research therefore focuses on northwestern Europe, having the advantage that well-documented, open-source data on air traffic movements from EUROCONTROL is available for this region.

Figure 3.2 shows the domains used in this study, geolocated on the European map where each dot represents a node (grid cell center). The generic configuration is a parent domain - referred to as d01 - with three nested or child domains - d02, d03, and d04. The number of domains, together with the spatial extent of each domain and its resolution, have to be weighted against its computational cost. Lower spatial resolution allows for longer simulation times or a larger research area, but limits the spectrum of physical processes that can be explicitly solved by the model (processes on sub-grid scale may be missed), thereby decreasing the model accuracy.

With a resolution of $0.5° \times 0.5°$ (roughly 34×55 km) on d01 using a four domain configuration, d04 has a resolution of approximately 1.3×2.1 km - sufficient to explicitly solve for clouds present at horizontal mesoscale. Note that a parent-child resolution ratio of 1:3 is applied, which enhances computational efficiency and accuracy due to the grid structure that WRF-Chem uses (the Arakawa C-staggered grid, see Arakawa and Lamb [1977]). As largest model uncertainties can be expected near the domain boundaries, the child domains have been centered within their respective parent domains. The uncertainties near the domain boundaries particularly apply to d01, for which boundary conditions are supplied from an external (global) model. In Section 3.4 this is discussed in more detail.

As discussed previously, this study focuses on short-term air quality. A spatial configuration as such, with modeling parameters as discussed in Section 3.3, leads to a real simulation time of ~1 hour per 8 simulated hours. Within the available time window for this research, each model simulation spans 16 (simulated) days, from May 30th 2019 at midnight till Jun 15th 2019 at midnight. This includes two days that are used as spin-up time (May 30th and May 31st) to reduce the influence of initial conditions on the results. June 2019 is the most recent month for which air traffic data is available from the EUROCONTROL R&D Data Archive at the time of writing [EUROCONTROL, 2020]. Therefore, it best represents current air traffic density. Furthermore, June 2019 has been the warmest June in the Netherlands since the beginning of climate records in 1901, with anomalous sunshine hours (266 versus 201 normally) [Willemsen, 2020]. Under those conditions, changes in e.g. ozone, formed by

[1] The number of paying airline passengers multiplied by the total distance traveled, summed for all flights under consideration.

photolysis, should get exposed more clearly. Extreme months like June 2019 are expected to occur more frequently over the coming decades, which makes those weather conditions relevant to involve in this study.

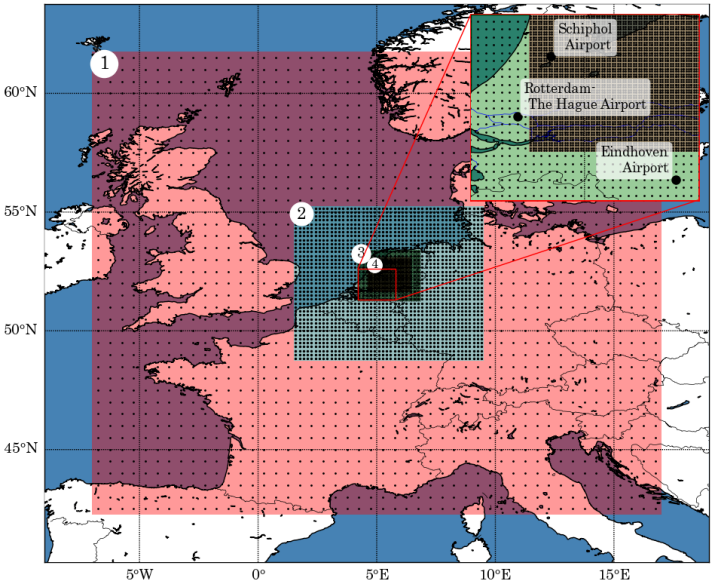

Figure 3.2. Four nested domains with the grid points shown as dots. An inset is made at the western boundary of the inner domain (d04), showing the location of Rotterdam-The Hague Airport and Eindhoven Airport within d03 and the location of Amsterdam Schiphol Airport within d04. Those airports will be studied in more detail, as is explained in Section 4.6.6. Details on the various domains can be found in Table 3.1.

Table 3.1. Overview of the nested domain configuration adopted in this study.

	d01	d02	d03	d04
Zonal resolution [degs (~km)]	0.5 (34.2)	1/6 (11.4)	1/18 (3.8)	1/54 (1.3)
Meridional resolution [degs (~km)]	0.5 (55.3)	1/6 (18.5)	1/18 (6.2)	1/54 (2.1)
Grid lines in west-east [-]	49	49	49	100
Grid lines in north-south [-]	40	40	40	79
Latitude range [min deg - max deg]	42.50-61.50	48.83-55.17	51.28-53.39	51.65-53.09
Longitude range [min deg - max deg]	-7.00-17.00	1.33-9.33	3.94-6.61	4.37-6.19
Surface area [km^2]	3,619,216	403,866	44,560	20,247

3.3. Model Parametrization

Through a namelist file, the main input and output parameters for the WRF-Chem core module can be defined. The namelist that is used for most of the performed simulations is shown in Appendix A.2. Some of the key namelist parameter settings from the *physics*, *fdda* (meteorology nudging), and *chem* group are further clarified below.

3.3.1. Physics

The WRF-Chem Morrison two-moment microphysics scheme (*mp_physics* in namelist) is used for this study for the simulation of cloud microphysics. This scheme, described by Morrison et al. [2009], predicts both mixing ratios and number concentrations of five main hydrometeorological variables involved in cloud dynamics - cloud droplets, rain, ice, snow, and graupel. This opposes the one-moment scheme where number concentrations are instead diagnostically determined, and is shown to be more realistic [Morrison et al., 2009]. Furthermore, the indirect effect that aerosols may have on Earth's radiative budget through microphysics is well represented using this scheme.

The short-wave (*ra_sw_physics*) and long-wave radiation (*ra_lw_physics*) parametrization should comply with the criteria to accurately resolve radiative changes in response to cloud optical properties and

ozone concentrations, in particular. The Community Atmosphere Model (CAM) radiation scheme provides those features as it considers trace gases and works with monthly mean pressure level data to compute ozone radiative forcing, compared to other solvers using single profiles [Collins et al., 2004]. In addition, CAM uses a year-dependent table of background concentrations for long-lived greenhouse gases like CO_2.

The Grell-3 scheme is used for the parametrization of cumulus clouds (*cu_physics*), which handles updrafts and downdrafts observed in deep convective clouds [Grell, 1993]. As those convections usually take place on scales of a couple of kilometers, a coarse grid (say $\Delta x > 3$ km) is not able to resolve these sub-grid phenomena, requiring a parametrization scheme. For the fine grid spacing of d04, the model dynamics is resolving the updrafts explicitly, which makes the use of a parametrization scheme redundant. Therefore this parameter is set to zero for d04, as is shown in Table 3.2. Shallow convective clouds forming at smaller horizontal scales (< 1 km) could yet be missed by the inner domain using this configuration. To tackle this, a shallow convection scheme (*shcu_physics*) is added for the inner domain. The Grell 3D ensemble scheme is used as it is compatible with the parametrization scheme of deep convective clouds [Grell and Dévényi, 2002].

The planetary boundary layer (PBL) parametrization scheme is closely coupled with the land surface and surface layer scheme, and the optimal choice for a specific simulation can not be determined a priori [Skamarock et al., 2008]. Nevertheless, the Yonsei University (YSU) PBL scheme in combination with the Unified Noah Land Surface Model (LSM) scheme and the Revised Mesoscale Model (MM5) scheme have been widely used and were shown to work satisfactorily [Hong et al., 2006; Jiménez et al., 2012; Skamarock et al., 2008; Zhuo et al., 2019]. The PBL scheme distributes surface fluxes with boundary layer (eddy) fluxes and computes the PBL dynamics. The LSM simulates variables such as soil moisture (both liquid and frozen), soil temperature, skin temperature, snowpack properties like its depth and canopy water content. Finally, the MM5 scheme resolves meteorological profiles and fluxes within the atmospheric surface layer - the lowest part of the boundary layer which is most affected by the planetary surface and which is characterized by large gradients in atmospheric variables.

Table 3.2 summarizes the discussed parametrization settings and chosen options for each of the four domains.

Table 3.2. Overview of main WRF-Chem configuration relates to the physics group.

Parametrization	Namelist key	Scheme (values between parentheses refer to the namelist value)			
		d01	d02	d03	d04
Cloud microphysics	mp_physics	Morrison two-moment (10)	Morrison two-moment (10)	Morrison two-moment (10)	Morrison two-moment (10)
Short-wave radiation	ra_sw_physics	CAM (3)	CAM (3)	CAM (3)	CAM (3)
Long-wave radiation	ra_lw_physics	CAM (3)	CAM (3)	CAM (3)	CAM (3)
Cumulus clouds/deep convection	cu_physics	Grell-3D (5)	Grell-3D (5)	Grell-3D (5)	- (0)
Shallow convection	shcu_physics	- (0)	- (0)	- (0)	Grell-3D ensemble (1)
Planetary boundary layer	bl_pbl_physics	YSU (1)	YSU (1)	YSU (1)	YSU (1)
Land surface	sf_surface_physics	Noah LSM (2)	Noah LSM (2)	Noah LSM (2)	Noah LSM (2)
Surface layer	sf_sfclay_physics	MM5 (1)	MM5 (1)	MM5 (1)	MM5 (1)

3.3.2. Meteorology Nudging

Meteorology nudging is used to relax the solution of a model, in this case WRF-Chem, on meteorological variables towards a physical reference state. The meteorological reference is observation-based. By applying meteo nudging after each defined time step - in this case every six hours - the model simulations remain in closer correspondence with observed quantities, giving a more realistic output. Within this study spectral nudging is applied, in which the relaxation procedure is applied on the base of equivalent wavelengths using a Fourier decomposition [Spero et al., 2018].

Meteo nudging in WRF-Chem can be done on temperature, moisture, geopotential height, and horizontal wind components (U and V). Spero et al. [2018] argues that spectral nudging performs best when

solely applied outside of the planetary boundary layer (PBL). Recommended nudging coefficients of 3×10^{-4} s^{-1} for temperature and horizontal wind speeds and 1.5×10^{-5} s^{-1} for moisture have been adopted [Spero et al., 2018; Stauffer and Seaman, 1994].

3.3.3. Chemistry

The chemistry settings used by the model involve the integration of anthropogenic (chemical) emissions which are added to the atmosphere at each time step. Sections 4.1 and 4.3 elaborate on the methodology of retrieving anthropogenic ground emissions and air traffic emissions, respectively. The emission files are four-dimensional - hourly emissions on a three-dimensional spatial domain. The vertical dimension consists of 21 levels, separated by 22 pressure levels which are defined through eta levels in the namelist. Eta levels are defined as follows:

$$\eta = \frac{p - p_{top}}{p_0 - p_{top}}, \tag{3.1}$$

where p is the pressure level corresponding with the eta level, p_{top} is the pressure at the top of the modeled domain, defined in the namelist[2], and p_0 is the pressure at sea-level (1013.25 hPa). Details on chosen eta levels are given in Appendix B. Section 4.3 further elaborates on the mapping of air traffic emissions to vertical layers. Anthropogenic ground emissions from TNO are all assigned to the lowest layer [van der Gon et al., 2014]. Those emissions are read in through auxiliary input port 5 in WRF-Chem [Skamarock et al., 2008]. Air traffic emissions are subsequently added to the anthropogenic ground emissions and by that means included in the simulations.

The aerosol modules and gas-phase chemical mechanisms, which dictate the speciation of species, is set through the *chem_opt* namelist parameter. The Carbon Bond Mechanism Version Z (CBM-Z), in combination with the Model for Simulating Aerosol Interactions and Chemistry (MOSAIC), are used in this study [Zaveri and Peters, 2008; Zaveri et al., 2008].

In short, CBM-Z is responsible for the simulation of gas-phase chemical processes in the atmosphere. To increase the computational efficiency of the model, certain organic species are 'lumped' together within the CBM-Z mechanism [Wang et al., 2019]. A clear disadvantage of this method is that in reality lumped species have distinct chemical reaction properties. Besides its computational efficiency, Balzarini et al. [2015] found that the CBM-Z mechanism reconstructs gaseous species, including ozone, with higher accuracy than its counterpart $RADM_2$. The motivates the choice for the CBM-Z scheme. In the particulate case of ozone, using the CBM-Z scheme over the $RADM_2$ scheme yields lower O_3 concentrations due to more efficient O_3-NO titration [Balzarini et al., 2015; Yang et al., 2018].

The MOSAIC module is responsible for the gas-to-particle partitioning and simulates the thermodynamics equilibrium, condensation, coagulation, and nucleation of aerosol species [Balzarini et al., 2015]. Aerosols are binned into four groups based on particle diameter - in the range 0.04–0.156 μm; 0.156–0.625 μm; 0.625–2.5 μm and 2.5–10 μm. The mechanism includes some aqueous reactions too. Yang et al. [2018] and Bucaram and Bowman [2021] show that the MOSAIC module brings along comparable biases and uncertainties compared to MADE/SORGAM - the aerosol module coupled with $RADM_2$.

Tropospheric photolysis rates are strongly affected by reflective surfaces within the atmosphere, particularly clouds and aerosol layers. The photolysis scheme adopted for this study is the Fast-J scheme, which is preferred over the TUV scheme because of its computational efficiency, yet producing accurate results [Wild et al., 2000]. A more computationally efficient scheme allows for a more frequent update of photolysis rates within the 3-D domain. The Fast-J scheme achieves higher computational efficiency by a reduced number of wavelength bins compared to the TUV scheme (17 versus 140 bins) and a simplified equation set. Nonetheless the calculated photolysis rate inaccuracies are generally maintained within 3% [Wild et al., 2000].

Dust emissions are included from the Goddard Chemistry Aerosol Radiation and Transport (GOCART) emissions inventory, together with dimethylsulfide (DMS) - the largest contributor to chemistry involving sulfuric species - emissions from the sea surface, and sea salt emissions [Ginoux et al., 2001;

[2] In this study $p_{top} = 100$ hPa, which corresponds to a height of approximately 16 km.

Seinfeld and Pandis, 2016]. Remaining namelist settings can be found in Appendix A. The discussed parametrization schemes are summarized in Table 3.3.

Table 3.3. Overview of main WRF-Chem configuration relates to the chemistry group.

Parametrization	Namelist key	Scheme (values between parentheses refer to the namelist value)			
		d01	d02	d03	d04
Gas-phase mechanism	chem_opt	CBM-Z (32)	CBM-Z (32)	CBM-Z (32)	CBM-Z (32)
Aerosol chemistry	chem_opt	MOSAIC using 4 aerosol bins (32)	MOSAIC using 4 aerosol bins (32)	MOSAIC using 4 aerosol bins (32)	MOSAIC using 4 aerosol bins (32)
Photolysis	phot_opt	Fast-J (2)	Fast-J (2)	Fast-J (2)	Fast-J (2)
Dust emissions	dust_opt	GOCART (1)	GOCART (1)	GOCART (1)	GOCART (1)
DMS emissions from sea surface	dmsemis_opt	GOCART (1)	GOCART (1)	GOCART (1)	GOCART (1)
Sea salt emissions	seas_opt	GOCART (2)	GOCART (2)	GOCART (2)	GOCART (2)

3.4. Initial and Boundary Conditions

Initial and boundary conditions are important when running simulations as they define the initial state within and the in- and outflow at the boundaries of the studied domain. With the configuration of nested domains, the in- and outflow of the inner domains - d02, d03, and d04 - can be solved explicitly by the model simulation, as the domain in which each inner domain is nested provides its boundary conditions. For the outer domain (d01), the boundary conditions cannot be retrieved within the simulation, as the concentrations outside the domain are not simulated in the model. Therefore, external boundary conditions have to be given to the model that describe - over the entire temporal domain - to what values the simulation has to converge at the boundaries.

The initial and boundary conditions relating to chemistry are provided from CAM, which has been coupled with the gas-phase MOZART-T1[3] chemical mechanism to create CAM-chem [Buchholz et al., 2019; Emmons et al., 2020]. Aerosol chemistry is taken care of by the Volatility Basis Set scheme (VBS), of which more details can be found in Tilmes et al. [2019]. CAM-chem is a component of the Community Earth System Model 2 and is maintained and provided by the National Center for Atmospheric Research (NCAR). CAM-chem creates global simulation output that can be applied as initial and boundary conditions for regional modelling as done in this study [Buchholz et al., 2019].

The CAM-chem model output used provides concentrations of chemical compounds on 56 vertical pressure levels, at a $0.9° \times 1.25°$ horizontal resolution. The vertical levels are reduced to a set of 27 pressure levels, shown in Appendix A.1 under *mod_levs*. those levels fall within the vertical simulation domain and assure that the WRF-Chem model convergences. Due to mismatches between species nomenclature in the MOZART-T1 mechanism and the CBM-Z mechanism (and similarly between VBS and MOSAIC), a mapping is done on the CAM-chem files to create compatible WRF-chem input files.

For meteorological variables, the National Centers for Environmental Prediction FiNaL reanalysis (NCEP-FNL) data product is used [FNL, 2000]. This product prescribes the initial conditions on which all four domains are initialized, together with the boundary conditions that apply to the outer domain (d01). NCEP-FNL yields model-based data sets, assimilated by observations from the Global Data Assimilation System which collects observational data. The parameters include surface and sea-level pressure, geopotential height, (sea surface) temperature, soil parameters, ice cover, relative humidity, horizontal wind components, vertical motion, vorticity, and ozone. The data product has a time resolution of six hours and is used every six hours within the WRF-Chem simulation to nudge meteorology, as is described in Section 3.3.2.

[3]MOZART stands for Model for Ozone and Related chemical Tracers and includes 151 gas-phase species. The more detailed speciation of compounds and oxidation of isoprene and terpenes has led to a significant improvement of e.g. ozone simulations compared to the previous MOZART-4 mechanism [Emmons et al., 2020].

4

Research Methodology

This chapter focuses on the research methodology adopted in this study, starting with a description of how anthropogenic ground emissions are generated (Section 4.1). The Advanced Emission Model (AEM) is discussed in Section 4.2. The AEM is used to estimate air traffic emissions, based on data sets on air traffic movements that are described in Section 4.3. The air traffic emission scenarios that are implemented into WRF-Chem are discussed in Section 4.4. The resulting air traffic emissions and their mapping to CBM-Z species are discussed in Section 4.5. Section 4.6 describes how the WRF-Chem output is assessed. Finally, Section 4.7 describes the evaluation metrics used to validate the modeling results with observations (Chapter 6).

4.1. Spatio-Temporal Anthropogenic Ground Emissions

The anthropogenic emission input to WRF-Chem is discussed in this section. The TNO-MACC-III data product[1] for the year 2014 is used as a starting point, as the data product for 2019 (the year that is simulated) is not available [van der Gon et al., 2014]. This product contains year-averaged anthropogenic European emissions data, gridded onto a $0.125° \times 0.0625°$ resolution. This data set contains nitrogen oxides (NO_x), sulfuric oxides (SO_x), ammonia (NH_3), non-methane volatile organic compounds, carbon monoxide (CO), fine particulate matter ($PM_{2.5}$), and coarse particulate matter (PM_{co}) emissions. The emissions are specified per so-called Selected Nomenclature for sources of Air Pollution (SNAP) sector, which is a subdivision of anthropogenic emission sources.

Additionally, European anthropogenic ground emissions are provided by the Centre on Emissions Inventories and Projections (CEIP) [Matthews and Wankmueller, 2021]. This data base, used in EMEP models[2], is an aggregate of year total national emissions data, specified per GNFR (Gridding Nomenclature for Reporting) sector. As the CEIP data sets are available both in 2014 and 2019, this source is used as a means of retrieving emission (scaling) factors between both years for specific pollutants, countries and emission sectors. As the SNAP sector subdivision differs from the GNFR sector subdivision, the mapping shown in Figure 4.1 is applied. For the 2019 data set, the ”H: Aviation” GNFR sector emission is made zero to exclude the contribution of the aviation sector to total anthropogenic emissions. Air traffic emissions are added to the emission inventory in a later stage, making use of EUROCONTROL data and AEM, as will be explained further in Section 4.4.

Finally, EMEP ISO2 codes are mapped to land/area codes. The resulting scaling factors are applied on the TNO data set for 2014 to obtain the anthropogenic emissions data set for 2019. Looking at the EMEP data, e.g. for the Netherlands, the year total anthropogenic NO_x emissions in 2014 sum to 255.8 kilotonnes - excluding shipping - versus 215.5 kilotonnes (-15.7%) in 2019. This is in close correspondence with the nationally reported emissions data by the Dutch Rijksinstituut voor Volksgezondheid en

[1] MACC or ”Monitoring Atmospheric Composition and Climate” was the precursor of the operational Copernicus Atmosphere Monitoring Service, in short CAMS [ECMWF, 2016].

[2] EMEP stands for European Monitoring and Evaluation Programme. Its models form the basis of an overarching cooperative program for the monitoring and evaluation of the transmission of air pollutants in Europe [Simpson et al., 2012b].

Milieu (RIVM), which reports 238.1 kilotonnes NO_x emissions within the Netherlands for the year 2014 [CLO, 2021].

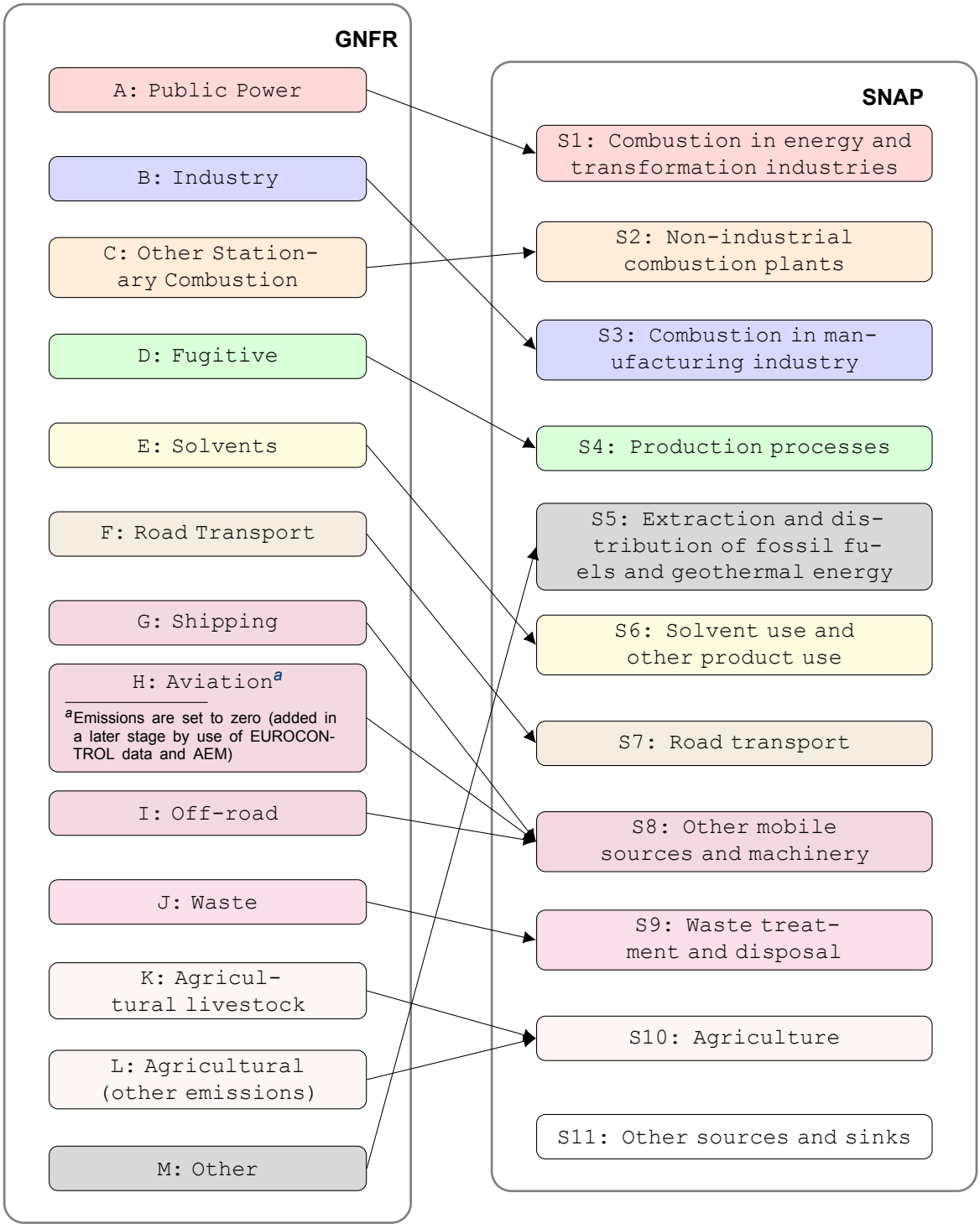

Figure 4.1. Used mapping from GNFR sectors to SNAP sectors.

To add temporal information of the emissions data, two additional emission factors are applied: one incorporating monthly variations in emissions per SNAP sector, and another one incorporating intra-daily variability. Those emission factors, obtained from Roberts et al. [2008], are shown in Figures 4.2 and 4.3.

Figure 4.2 shows that e.g. power generation and residential energy use (e.g. heating systems) are

higher during winter than during summer. Emissions from agricultural practises are much lower in winter and peak in spring, when conditions for cultivation of crops are most favorable. The relevant emission factors for this study related to June are indicated in Figure 4.2.

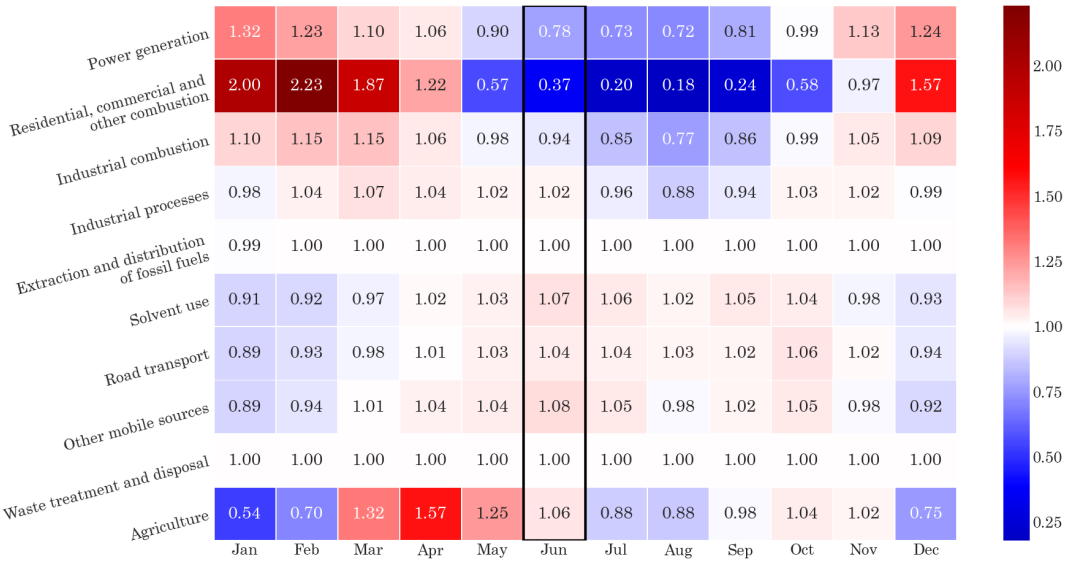

Figure 4.2. SNAP emission factors related to the month of the year. The color bar is centered at 1 (corresponding to year averaged emissions), with red color tones indicating above-average emissions and blue color tones below-average emissions.

The daily fluctuations in anthropogenic ground emissions are captured by the hourly emission factors shown in Figure 4.3. The SNAP sectors ”Extraction and distribution of fossil fuels”, ”waste treatment and disposal”, ”industrial processes”, and ”other mobile sources” show no intra-daily variability. For most sectors, emissions are higher during the day than during the night. Road transport emissions exhibit two rush-hour peaks. Emission variations on a daily time scale, e.g. between week days and weekend days, are neglected as those variations are smaller than the intra-daily and inter-monthly variations.

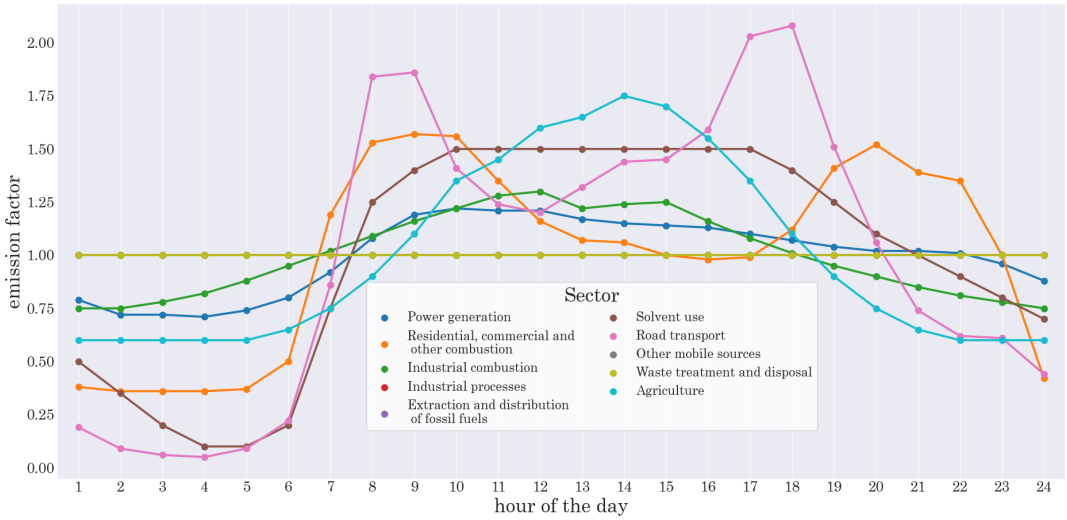

Figure 4.3. Intra-daily variability in anthropogenic ground emissions, shown as emission factor per SNAP sector as a function of time.

The aforementioned seven species that constitute the anthropogenic ground emissions data set should finally be mapped to the CBM-Z speciation. This is done by mapping 90% of NO_x emissions to NO and the remaining 10% to NO_2. SO_x is fully mapped to SO_2, i.e. with the assumption that all sulfuric oxides are being emitted in the form of sulfur dioxide. $PM_{2.5}$ is mapped for 20% to $PM_{2.5}$ in accumulation

mode (pm25i) and 80% to $PM_{2.5}$ in nuclei mode (pm25j). Mapping of aggregate non-methane volatile organic compound emissions to the specific compounds defined in the CBM-Z scheme - methanol, ethanol, ethane, propane, alkanes, ethenes, alkenes, propene, isoprene, toluene, xylenes, aldehydes, ketones, and organic acids - is done based on SNAP sector. In other words, the speciation of total non-methane volatile organic compound emissions is different for each SNAP sector. Values are taken from the EMEP MSC-W model [Simpson et al., 2012a].

Figure 4.4 shows three examples - one for NO_x, one for ammonia (NH_3), and one for ketones - of the resulting daily emission profiles as used for the WRF-Chem runs. It clearly shows that the intra-daily variability of NO_x is strongly dictated by road transport (see Figure 4.3), with a morning peak and an afternoon peak. NH_3 appears to follow the intra-daily pattern of agricultural emissions. This could be expected as a major source of NH_3 in the atmosphere is the loss of NH_3-based fertilizers of soils, together with animal waste [Seinfeld and Pandis, 2016]. Finally, ketones exhibit a highly comparable pattern with solvent use. Acetone, one of the most abundant ketones, is commonly used as cleaner and degreaser.

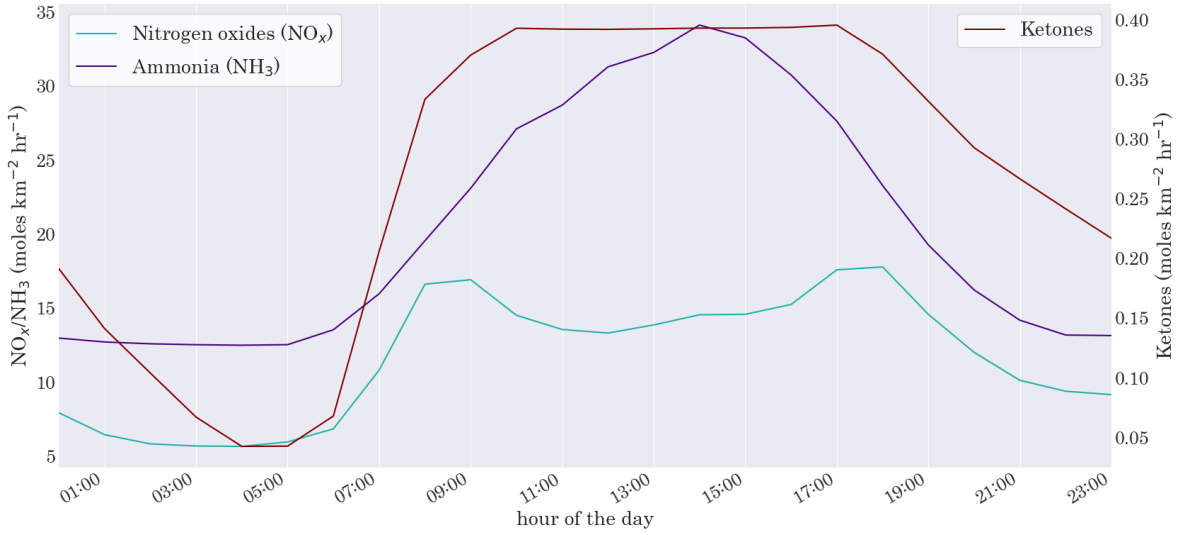

Figure 4.4. Daily emission profiles used as anthropogenic ground emission input for the WRF-Chem runs. Examples shown are NO_x, NH_3 and the ketones group (VOC). Emissions are total column emissions, averaged over d04 and normalized by the ground surface area.

4.2. The Advanced Emission Model

The Advanced Emission Model (AEM) is developed by EUROCONTROL with the aim to estimate the environmental impact aviation has, both now and in the future [EUROCONTROL, 2021a]. The model was developed in 2000 and has been under continuous development ever since. Passing the stress tests of the International Civil Aviation Organization (ICAO) in 2008-2009, AEM was included in the set of tools adopted by the ICAO's Committee on Aviation Environmental Protection - a technical committee that assists in the formulation of new policies concerning aircraft noise and emissions. Due to the maturity of the model in conjunction with its integrated use in policy making, the model is considered sufficiently reliable within this study for the assessment of air traffic emissions.

AEM assesses operational air traffic emissions on a flight-by-flight basis, whereby each flight is decomposed into nine flight phases. This is shown schematically in Figure 4.5. For each flight segment analyzed by AEM, the model estimates the total mass of fuel burned and the respective mass of - both gaseous and particulate - pollutants. Those pollutants include NO_x, CO_2, SO_x, H_2O, CO, HCs, acetaldehyde, acrolein, polycyclic aromatic hydrocarbons, styrene, 1,3-butadiene, benzene, ethylbenzene, formaldehyde, propianaldehyde, toluene, xylene, particulate matter with an aerodynamic diameter of less than 2.5 and 10 micrometres ($PM_{2.5}$ and PM_{10}), volatile, volatile sulfuric, and non-volatile particulate matter.

- AEM assumes the landing and take-off cycle (LTO cycle) takes place between ground level and

3,000 ft (roughly 900 meters) and formally includes the taxi out, taxi in, take-off, climb out, approach, and landing phases. The landing and approach phases are assumed to be operated with the same engine setting (called ”approach”), and similarly both the taxi in and taxi out phase are assumed to be operated in idle. Therefore, the total LTO cycle includes four engine operation settings. Relative to the maximum certified engine thrust output, idle corresponds to 7% thrust output, approach to 30%, climb-out to 85%, and take-off to 100%. Fuel flow and emission factors are sought for by AEM for each segment. This is done based on the engine setting and the engine type, the latter taken as the main engine type of the corresponding aircraft type (could be multiple). AEM integrates several sources providing fuel flow and emission factors given a certain aircraft (engine) type:

  - For turbojet and turbofan engines, the ICAO Aircraft Engine Emissions Databank (AEED) is used [ICAO, 2021].
  - For piston engines, the Federal Office of Civil Aviation (FOCA) databank is used [FOCA, 2021].
  - For turboprops, the Swedish Defence Research Agency (FOI) databank is used [FOI, 2021].
- Emissions during the remaining three flight phases above 3,000 ft - climb, cruise and descent - are calculated using EUROCONTROL’s Base of Aircraft Data (BADA) in conjunction with the AEED [ICAO, 2021; Nuic et al., 2010].

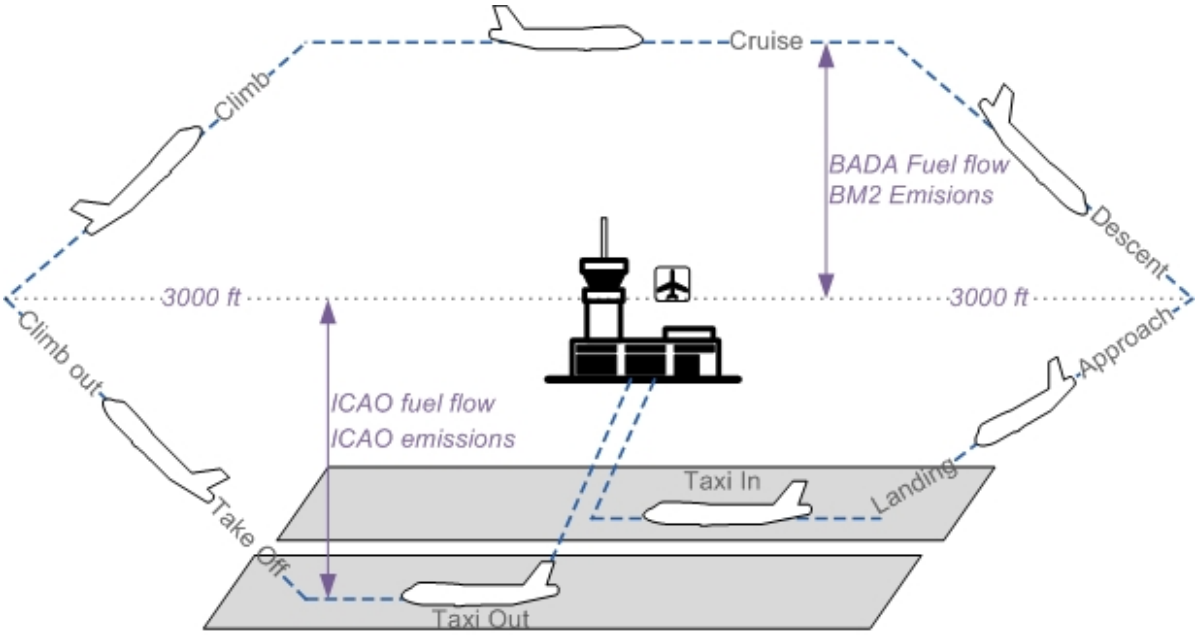

Figure 4.5. Flight phases as distinguished by AEM. Schematic retrieved from EUROCONTROL [2021b].

Once the mass of the burned fuel is estimated, the SO_x emissions can be determined as SO_x emissions are directly proportional to the burned fuel mass with a proportionality factor based on the sulfuric content of the burned fuel. H_2O and CO_2 can also be assumed to be proportional to the burned fuel mass, as they directly result from the oxidation of combusted carbon and H_2 with atmospheric oxygen [EUROCONTROL, 2021b]. Their emission factor in kilograms per burned kilogram of fuel is 1.237 kg/kg for H_2O and 3.155 kg/kg for CO_2.

A more sophisticated method, where the emission factor estimation additionally involves flight speed, engine thrust setting and ambient atmospheric conditions as a function of altitude, is used primarily to estimate the emission of NO_x, CO, and some HCs that show a strong dependence on aforementioned variables. Given some reference (sea-level) emission factors that are provided by e.g. BADA, the factors are adapted using the semi-empirical Boeing Fuel Flow Method 2 technique that incorporates flight speed, thrust setting, and ambient atmospheric conditions [DuBois and Paynter, 2006; Nuic et al., 2010]. The emission of VOCs - also resulting from incomplete combustion - can be deduced from the mass of emitted HCs by means of a proportionality factor, just as other organic gases and particulate

matter [EUROCONTROL, 2021b].

Once the burned fuel mass and the emission factors are determined for a certain flight segment, they are multiplied by the number of engines to obtain the total mass of each pollutant emitted during that flight segment. It boils down to the following equation:

$$E(C, seg) = FF(T) \cdot EF(C, V, T, h) \cdot t(seg) \cdot N, \tag{4.1}$$

where E is the emitted mass (kg) of compound C on segment seg, FF is the fuel flow (kg/s, per engine) which depends on the thrust setting T, EF is the emission factor (kg/kg, per engine) which depends on the compound C (and - depending on the compound - on the thrust setting T, flight speed V, and flight level h), t is the time spent in the considered segment (seconds), and N is the number of engines. The masses per flight segment are the output of the model.

In Figure 4.6, the AEM kernel is shown schematically. The generation of the flight profile data file that provides the external input to AEM is described further in Section 4.3.

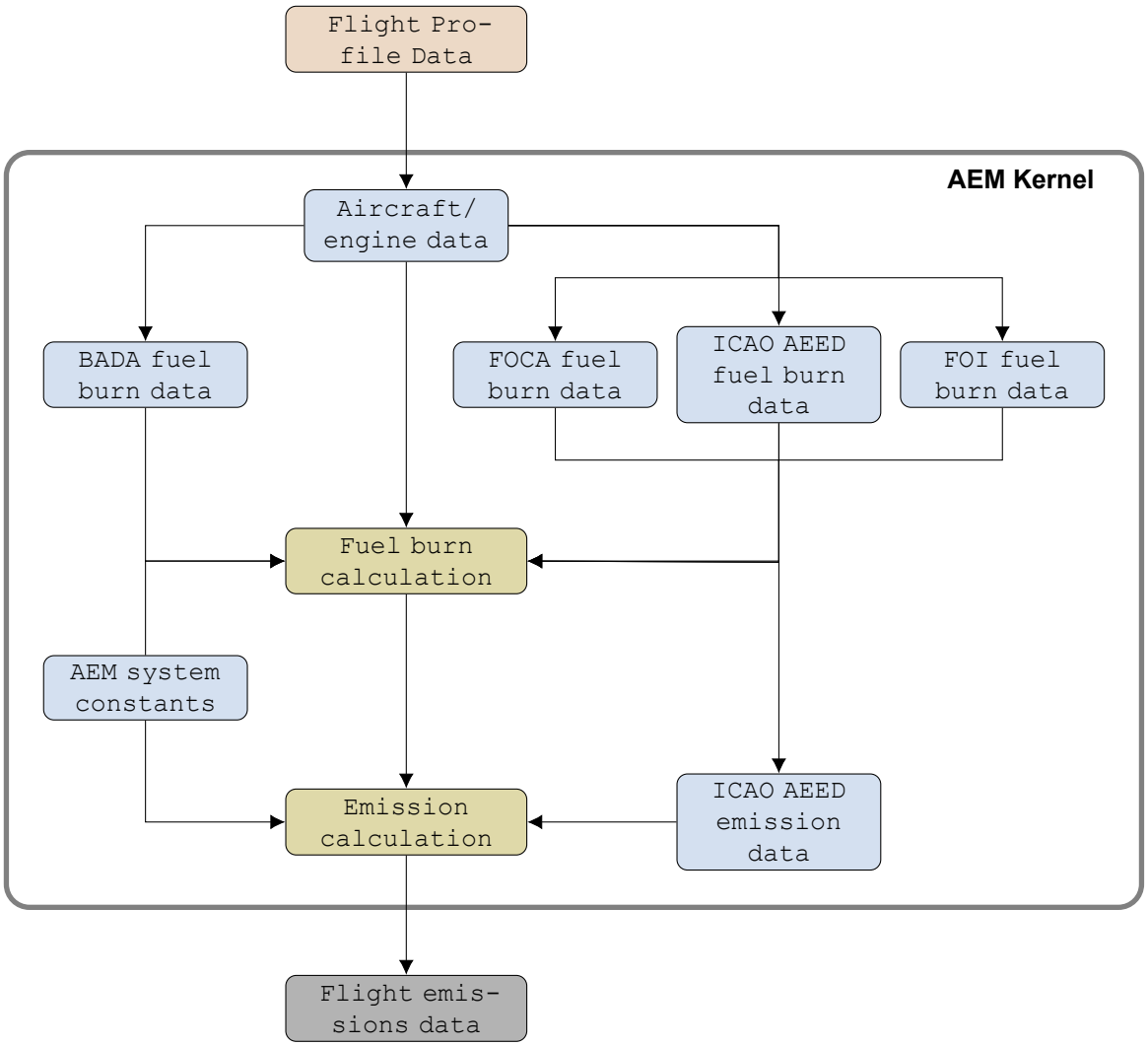

Figure 4.6. AEM Kernel system model flow chart.

4.3. Spatio-Temporal Air Traffic Emissions

For each air traffic emission scenario that will be discussed in Section 4.4, air traffic emissions are added to the anthropogenic ground emission files from Section 4.1. This section discusses how spatio-temporal air traffic emission profiles are generated for the year 2019.

As the manager of European air traffic network, EUROCONTROL keeps track of all commercial flights in and over European airspace. Those data sets are constructed from flight plans and are supplemented with radar data, data from air navigation service providers' flight data systems, and Automatic Dependent Surveillance-Broadcast[3] datalink communications. At the time of writing, the R&D data archive provides those data sets for the months March, June, September, and December during the years 2015-2018 and for March and June 2019 [EUROCONTROL, 2020].

Key data on each individual flight registered by EUROCONTROL are documented in a *Flights* data set, accompanied with its unique EUROCONTROL identifier - ECTRL ID. Each row represents one unique flight. On average those monthly *Flights* data sets contain around 800,000 rows, meaning about 800,000 flights are registered by EUROCONTROL on a monthly basis. Furthermore, each flight is given a unique identifier, referred to as 'ECTRL ID'. An abstraction of such a data set for June 2019 is shown in Table 4.1.

Table 4.1. First three rows of a *Flights* data set showing three flights taking place on the 1st of June 2019.

Index	ECTRL ID	ADEP	ADEP Latitude	ADEP Longitude	ADES	ADES Latitude	ADES Longitude	Filed Off Block Time	Filed Arrival Time	...
0	230520350	EGSS	51.885	0.235	EGAA	54.6575	-6.21583	01-06-2019 00:00:00	01-06-2019 01:15:51	...
1	230520351	LMML	35.8575	14.4775	OERK	24.9667	46.7	01-06-2019 00:00:00	01-06-2019 04:22:02	...
2	230520352	KATL	33.6333	-84.4333	EGLL	51.4775	-0.46139	01-06-2019 00:00:00	01-06-2019 07:45:23	...

...	Actual Off Block Time	Actual Arrival Time	AC Type	AC Operator	AC Registration	ICAO Flight Type	STATFOR Market Segment	Requested FL	Actual Distance Flown (nm)
...	31-05-2019 23:59:00	01-06-2019 01:02:00	B734	AWC	GPOWP	S	Traditional Scheduled	320	300
...	31-05-2019 23:50:00	01-06-2019 04:11:52	E35L	LNX	GSPCY	N	Business Aviation	390	1930
...	01-06-2019 00:00:00	01-06-2019 07:50:39	A333	VIR	GVINE	S	Traditional Scheduled	370	3748

The *Flight Points* data sets, of which an abstraction for the first flight in Table 4.1 is shown in Table 4.2, contains the time and position of the respective flight at various instances This allows for a reconstruction of the four-dimensional trajectory of each flight.

Table 4.2. First three and final three rows of flight 230520350 from London Stansted Airport, UK (EGSS) to Belfast International Airport, Northern Ireland (EGAA), contained in the *Flight Points* data set.

Index	ECTRL ID	Sequence Number	Time Over	Flight Level	Latitude	Longitude
0	230520350	0	2019-06-01 00:07:00	0	51.885	0.235
1	230520350	1	2019-06-01 00:08:21	30	51.8344	0.15889
2	230520350	2	2019-06-01 00:09:05	50	51.8583	0.09611
...	...	...	...	...	...	...
22	230520350	22	2019-06-01 00:52:32	98	54.5183	-5.4525
23	230520350	23	2019-06-01 00:59:45	23	54.7056	-6.03695
24	230520350	24	2019-06-01 01:02:00	0	54.6575	-6.21583

The trajectory of the flight from Table 4.2 is shown on a map in Figure 4.7b, where the vertical profile

[3]A technique by which aircraft can automatically downlink their location on a high temporal frequency.

is shown in Figure 4.7a. Each adjacent pair of data points forms a flight segment. Each flight trajectory is linearly interpolated on fixed one-minute time intervals. This is done to obtain a more detailed discretization of the flight path so that emissions can be more accurately determined. Not interpolating could cause the algorithm to completely miss certain flight segments. Processing those data sets on one-minute intervals resulted to be the maximum a single processing unit could handle. An algorithm is developed to assign a flight phase - taxi in/out, take off, climb out, climb, cruise, descent, approach or landing - to each flight segment. This algorithm uses the average flight level during the trajectory and climb/descent rates to estimate the flight phase (e.g. a zero climb rate at the defined cruise level would be classified as ”cruise”). The fuel flow (and thereby the emission) during a flight segment depends on the flight phase as is shown in Figure 4.9a.

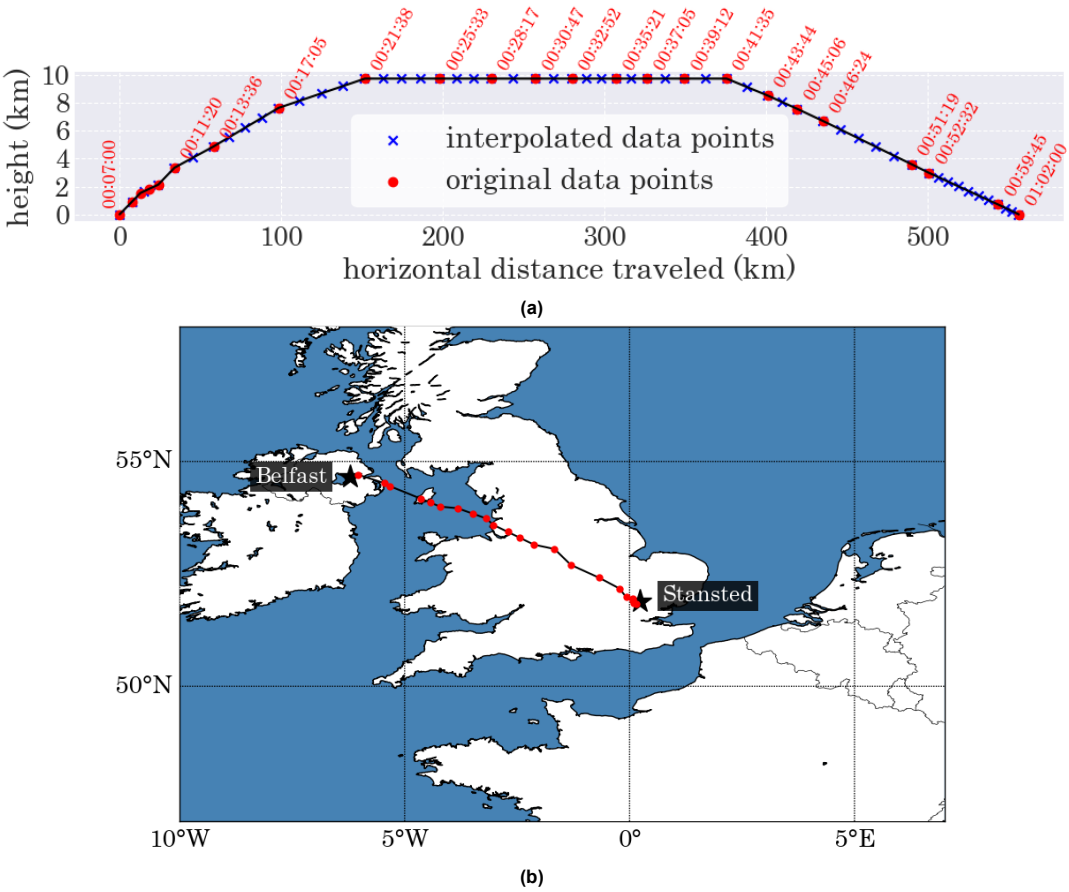

Figure 4.7. Flight 230520350, **(b)** shown on a map with **(a)** the vertical flight profile (flight level in kilometers) versus traversed horizontal distance. Red dots in both subplots indicate the original data points from the EUROCONTROL *Flight Points* data set. The interpolated data points are shown as blue crosses in **(a)**.

The interpolated data set, merged with the *Flights* data set and complemented with the flight phase for each segment, is manipulated as such that it can be read by AEM, described in Section 4.2. AEM requires each flight segment (flight segment ID, start/end time, and start/end 3-D position) to be defined on a single row, complemented with the traversed distance within the segment and the flight phase, along with other information on the flight (aircraft type, flight ID, etc.), all in a specified format. The created AEM input file is returned by AEM in a similar format, extended with the emitted mass (in kgs) of various species (see Section 4.2). Post-processing is done on this data set, after which the emissions per species are gridded onto the four domains with a temporal resolution of one hour, in line with the anthropogenic ground emissions. The data wrangling process from EUROCONTROL air traffic data to air traffic emission profiles is summarized in Figure 4.8.

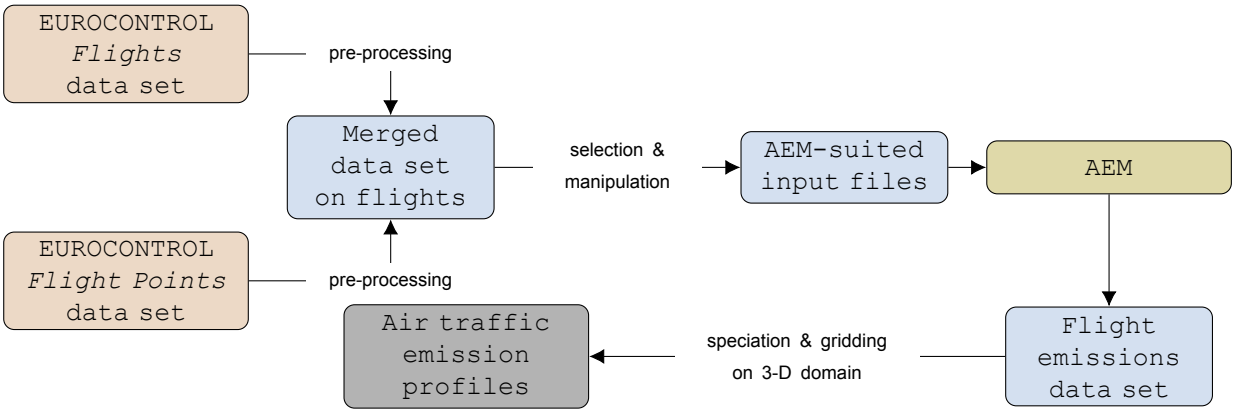

Figure 4.8. The process from raw air traffic data to air traffic emission profiles.

Figure 4.9a shows the fuel flow extracted from the AEM output file, grouped by flight phase. Taxi-in and taxi-out are lumped together, just as approach and landing. Discriminating between those flight phases would significantly complicate the algorithm, while differences in fuel burn are negligible.

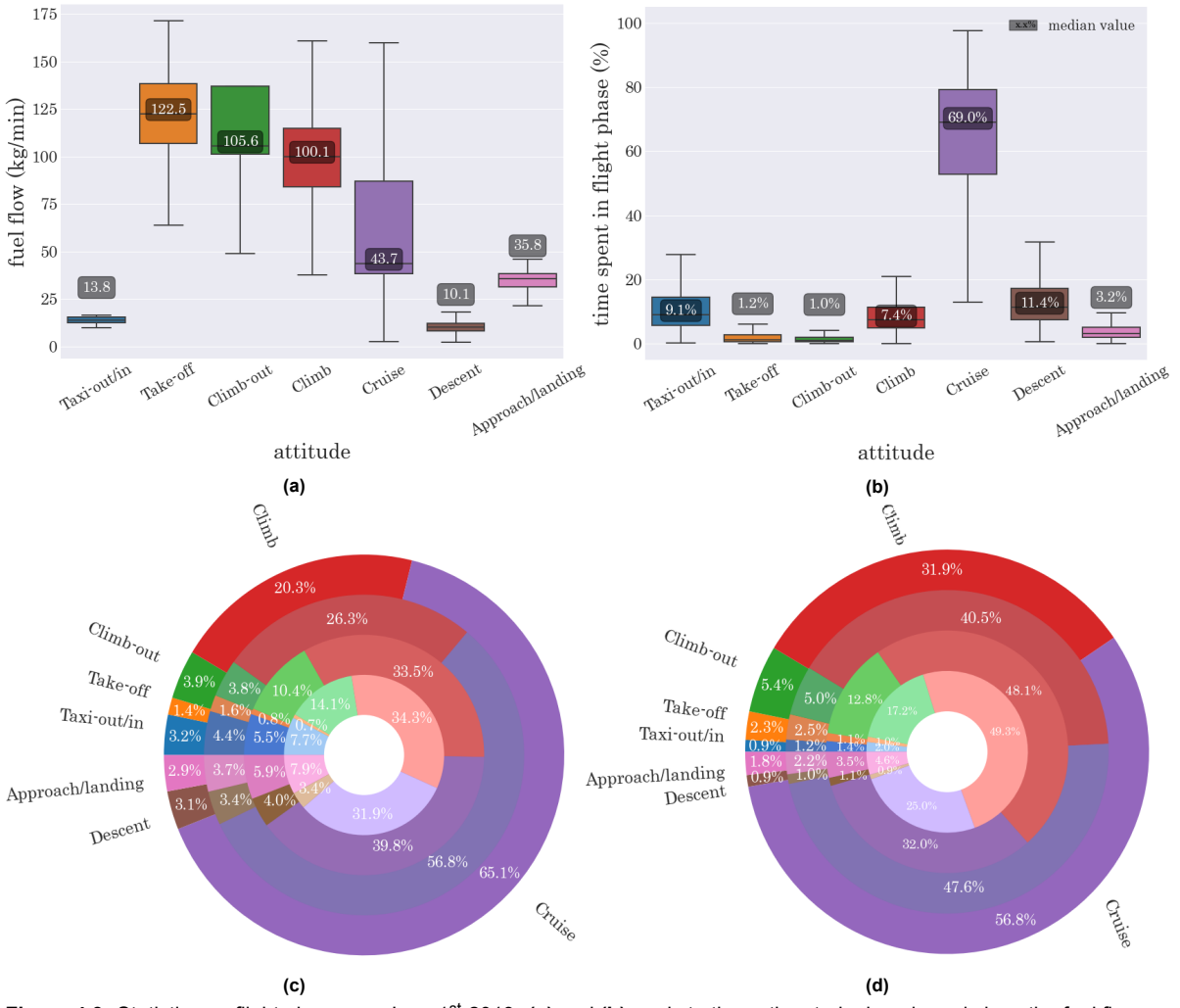

Figure 4.9. Statistics on flight phases on June 1st 2019. **(a)** and **(b)** apply to the entire study domain and show the fuel flow as a function of flight phase **(a)** and the time spent in each flight phase **(b)** for a random collection of 10,000 flights. Whiskers show the 1.5× inter-quartile range deviation from the corresponding box edges. The labels show median values. **(c)** and **(d)** show the total fuel burned and total emitted NO_x, respectively, per flight phase from Figure 4.5 and per domain. The outer ring corresponds to d01, the second outer ring to d02, etc.

Clearly, fuel rates are highest during the ascending phase of operations. Air traffic spend a majority of their operational time in cruise phase, as can be seen in Figure 4.9b. Combining this with the moderate fuel flow during cruise leads to the highest quantity of pollutants being emitted in cruise phase out of all flight phases, mostly at a height of 10-12 km. This can be seen in Figure 4.9c, which shows the distribution of fuel mass burned for all flight phases within the four nested domains. Within d01 almost three quarters of fuel consumption takes place in the cruise phase. This proportion declines within the inner domains, where the climb phase becomes the flight phase in which most fuel is being burned of all flight phases. This is relevant as emissions taking place lower in the atmosphere are expected to have more impact on ground-level air quality. Comparing Figures 4.9c and 4.9d, it can be seen that there is no one-to-one correspondence with fuel mass burned and NO_x emissions. On average, the NO_x released per unit mass of fuel burned during climb is relatively high while being relatively low during taxiing. This is because of thrust settings being relatively high during climb, leading to higher temperatures (and pressure) in the combustion zone by which NO_x emissions are enhanced (see Chapter 2). For d04, almost half of all NO_x emissions are emitted during climb.

Emissions are binned vertically on 21 vertical levels, i.e. separated by 22 pressure levels, as was briefly mentioned in Section 3.3.3. The (geopotential) height of pressure levels, as defined in Appendix B, is affected by topography and by temperature. Under colder conditions, isobars are squeezed closer together, resulting in thinner vertical layers. For the mapping of anthropogenic ground emissions to pressure levels no issues arise, as all emissions are assigned to the bottom layer and the time averaged layer thickness of the first layer is merely 54 meters, see Table 4.3. However, for higher levels the horizontal variation in layer thickness increases. For the 18th layer - a typical cruise level for air traffic between roughly 10.7 and 12 km - the spatial variation in layer thickness is maximum 210 meters. Yet those variations are mainly imposed by high mountains of Norway, the Alps and the Pyrenees, as can be seen in Figure B.2 in Appendix B. As ground level air quality is most affected by emissions in the lower vertical layers, air traffic emissions are vertically binned to layers that are uniform in horizontal direction. This saves computational time. Amsterdam is taken as the reference for the layer intersections. The resulting vertical bins are shown in Table 4.3.

Table 4.3. Vertical bins, displayed in whole meters above ground level and by flight level (hundreds of feet), by taking time averaged (geopotential) heights for a run on May 30th 2019, as used to bin air traffic emissions in the vertical.

Layer	Altitude range	Flight level	Layer (cont'd)	Altitude range	Flight level
1	[0, 54]	[0, 2]	12	[3,289; 4,117]	[108, 135]
2	[54, 92]	[2, 3]	13	[4,117; 5,113]	[135, 168]
3	[92, 186]	[3, 6]	14	[5,113; 6,344]	[168, 208]
4	[186, 327]	[6, 10]	15	[6,344; 7,778]	[208, 255]
5	[327, 528]	[10, 17]	16	[7,778; 9,211]	[255, 302]
6	[528, 792]	[17, 26]	17	[9,211; 10,510]	[302, 345]
7	[792; 1,122]	[26, 37]	18	[10,510; 11,638]	[345, 382]
8	[1,122; 1,527]	[37, 50]	19	[11,638; 12,831]	[382, 421]
9	[1,527; 2,014]	[50, 66]	20	[12,831; 14,340]	[421, 470]
10	[2,014; 2,596]	[66, 85]	21	[14,340; 16,335]	[470, 536]
11	[2,596; 3,289]	[85, 108]			

The daily air traffic volume (number of flights passing over European airspace) varies between 29,030 and 34,083 between June 1st 2019 and June 14th 2019. Inter-daily variations in air traffic emissions are assumed to be negligibly small and hence ignored in the simulations. June 1st 2019 is used as average day representing this period. Air traffic emission profiles are constructed for this day, analogous to the anthropogenic ground emission profiles. The same emission profile is implemented into WRF-Chem on each day of the simulation.

4.4. Air Traffic Emission Scenarios

This section presents four air traffic emission scenarios that are investigated in this study. For the sake of this analysis, flight operations are segmented into short-haul, medium-haul, and long-haul flights. Feasibility studies regarding hydrogen propulsion lead to different conclusions for each segment [FCH JU, 2020]. There is no general definition of this segmentation that has been agreed on in aviation industry. Frequently used metrics are aircraft type - each having a design range - or flight duration. Another metric is flight distance, which is used for this study as the traversed distance of each flight can be deduced from the EUROCONTROL data sets. Combining different sources that assume short-haul flights spanning less than 3 hours and medium-haul flights spanning between 3 and 6 hours, leads to the following definitions for short, medium, and long-haul flights [EUROCONTROL, 2015; FCH JU, 2020]:

- Short-haul flights: a flight distance up to 1,500 km. This involves commuter, regional, and other small aircraft accounting for nearly 40% of the total flown distance on June 1st 2019 within the study domain (see Figure 4.10). Most occurring aircraft types in this segment are the Airbus A320, Boeing B737-800, and Airbus A319, covering 25%, 20%, and 18% of flights within the short-haul segment, respectively.
- Medium-haul flights: a flight distance between 1,500 and 4,000 km accounting for nearly 50% of the total flown distance on June 1st 2019 within the study domain. The Boeing B737-800 (38%), Airbus A320 (22%), and Airbus A321 (10%) are the most frequent flyers in the medium-haul segment. As can be seen, aircraft types within this segment overlap with aircraft types in the short-haul segment. This is not considered of major importance for this study as flight destination plans for aircraft types would presumably be altered, if not taken out of service, by the time hydrogen propulsion would be used on a large scale in aviation industry. Moreover, flight distance is considered a more stringent factor in designing emission scenarios than aircraft type as new technologies such as H_2 fuel cells can only be used on certain flight ranges.
- Long-haul flights: a flight distance of more than 4,000 km. They contribute to the remaining 10% of flown kilometers within the study domain. The Boeing B777-300 Extended Range (14%), Boeing 787-900 (9%), and Airbus A330-300 (9%) are the most occurring aircraft types in this segment.

Those segments are used as building blocks to construct spatio-temporal air traffic emission profiles for each scenario. Section 2.2 addressed H_2 fuel cell technology and H_2 combustion as two feasible options to replace kerosene-based jet fuels. Within each scenario, each air traffic segment is assigned to either a ”propelled by conventional jet fuels” case, a ”propelled by H_2 combustion” case or a ”propelled by fuel cells” case. In practise, H_2 fuel cell propulsion might correspond to true zero emissions if the created water (vapor) is retained [Roland Berger, 2020]. As this would yield a large weight penalty to flight operations, it is more probable that H_2O emissions are conditioned as such that its climatological impact is the same as the current climatological impact of H_2O emitted by combusting conventional jet fuel. This can be done for example by adjusting the flight level at cruise to lower altitudes, where the climatological impact of each emitted unit mass of H_2O is smaller than at current cruise levels (due to a lower atmospheric lifetime). This assumption is adopted in this study as the WRF-Chem model does not provide an input for water vapor emissions.

Figure 4.10 shows the relative contribution of the short, medium, and long-haul flight segments to total mileage, burned fuel, $PM_{2.5}$, NO_x, SO_x, CO, and HC emissions resulting from the AEM output (assuming conventional jet fuel combustion). Despite the fact that the long-haul segment only contributes $\sim$10% to the total number of flown kilometers, nearly a quarter of all burned fuel by aviation is coming out of this segment. This can be reasoned by larger engines used, having a higher fuel flow. Figure 4.10 shows that the shares of different segments to fuel burned and sulfuric oxide emissions are the same. This reflects the use of a fixed sector-wide assumption by AEM on the sulfuric fuel content, and the linear scaling between fuel burn and sulfuric oxide emissions as discussed before. The share of long-haul flights in the total emission of incomplete combustion products - being primary $PM_{2.5}$, CO, and HCs - is lower than its share in total burned fuel. This indicates generally higher fuel burn efficiencies for engines mounted on air traffic flying long-haul distances. However, the share of NO_x emissions to total NO_x emissions is higher than the share of burned fuel for long-haul flights, possibly relating to relatively higher combustion pressure and temperatures. Overall, Figure 4.10 shows the non-linearity

between flown distance or fuel burn and the emission of specific compounds, which can be attributed to differences in engine properties.

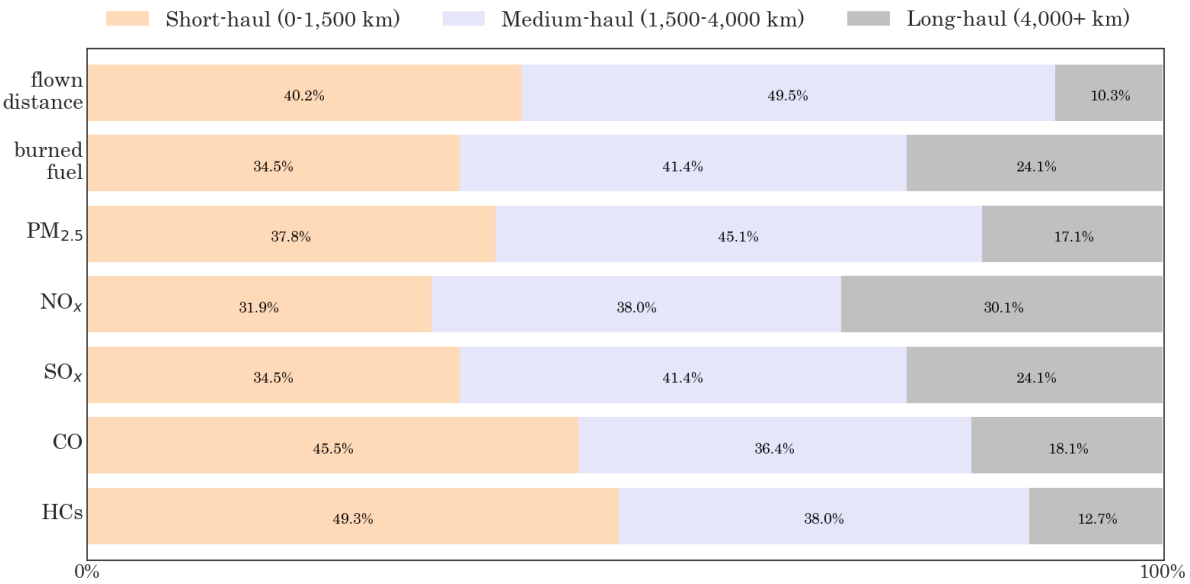

Figure 4.10. Share of flown kilometers, burned fuel, fine particulates ($PM_{2.5}$), nitrogen oxides (NO_x), sulfuric oxides (SO_x), carbon monoxide (CO), and hydrocarbons (HCs) emissions for three market segments - short, medium, and long-haul flights.

Table 4.4 shows an overview of the emission scenarios. Subsequent sections describe each scenario more elaborately.

Table 4.4. Scenarios as implemented in this study. Emission cases - A_1 represents the "propelled by fuel cells"/"zero emission" case, A_2 the "propelled by H_2 combustion" case, and B the "propelled by conventional jet fuels (kerosene-based)" case - are prescribed to each segment.

Scenario	Short-haul	Medium-haul	Long-haul
I	B	B	B
II	A_1	B	B
III	A_1	A_2	A_2
IV	A_1	A_1	A_1

4.4.1. Scenario I: 2019 Aviation Emissions

The current impact of air traffic on regional short-term climate and air quality should be assessed to provide a context for possible climate adaptations and air quality effects when flying on H_2 fuel. Therefore, in this scenario, 2019 aviation emissions - largely originating from conventional jet fuels - as interpreted by AEM are implemented into WRF-Chem. This scenario is referred to in this study as the baseline scenario.

4.4.2. Scenario II: H_2 Fuel Cells & Conventional Jet Fuel

According to FCH JU [2020], fuel cell technology in powering air traffic shows greatest potential for commuter, regional, and short-range air traffic, all lumped together in the short-haul category (flights spanning up to 1,500 km) in this study. For larger aircraft flying longer distances, fuel cell cooling requirements would be too heavy. Also economically fuel cell systems are more feasible on short-haul flights than on medium or long-haul flights. Therefore, scenario II assumes short-haul flights powered by fuel cells, while medium/long-haul air traffic remains flying on conventional jet fuels. This scenario is used to investigate potential emission reductions when sustainable flying is merely achieved on flights traversing short distances[4], keeping all of the rest the same, which corresponds to the first research question discussed in Chapter 1.

[4]With "short distances", distances below 1,500 km are meant, which more or less corresponds to the flight distance between Amsterdam, the Netherlands, to Madrid, Spain (2:30 hours flight time).

4.4.3. Scenario III: H_2 Fuel Cells & H_2 Combustion

Analogous to scenario II, short-haul air traffic is assumed to fly solely on fuel cell technology within scenario III. Now, conventional jet fuel is replaced by (liquid) H_2 for medium and long-haul flights. For those aircraft sizes and ranges, H_2 combustion results to be more feasible than the use of fuel cells, even though fuel cell technology might still be used on those flights as auxiliary power unit [FCH JU, 2020]. Comparing this scenario with scenario II should give more insight in potential effects of medium/long-haul air traffic replacing conventional jet fuel by H_2-based propulsion, which corresponds to the second research question discussed in Chapter 1.

4.4.4. Scenario IV: No Aviation Emissions

This scenario corresponds to the total exclusion of air traffic emissions, which in the context of cryogenic[5] air traffic propulsion corresponds to a scenario where all air traffic would be propelled using H_2 fuel cells. Thereby the emission of water (vapor) is disregarded, as this cannot be implemented into the model. An assumption imposed within this framework is that the emitted water vapor is captured or conditioned, at least to such an extent that flying on H_2 does not result into more atmospheric water vapor compared to flying on conventional jet fuels. Even though an entire aviation sector flying on H_2 fuel cells seems unrealistic with current knowledge, inclusion of this scenario is still considered worthwhile. It can be used to quantify the total impact of 2019 aviation emissions on air quality (by comparison with scenario I) and shows the potential of a zero-emission aviation sector.

4.5. Air Traffic Emissions Mapping

AEM provides emission data on various chemical species, as discussed in Section 4.2. The emissions of those species have to be mapped to the corresponding species defined in the CBM-Z scheme. A similar strategy as for anthropogenic ground emissions (Section 4.1) is used to achieve this. That is, NO_x is mapped for 90% to NO and the remaining 10% to NO_2, SO_x is fully mapped to SO_2, fine particulate matter ($PM_{2.5}$) is mapped for 20% to $PM_{2.5}$ in accumulation mode (pm25i) and for 80% to $PM_{2.5}$ in nuclei mode (pm25j) for the conventional jet fuel case.

Table C.1 in Appendix C shows all factors by which AEM species masses are mapped to the respective CBM-Z species, for each emission case described in Section 4.4 (case A_1/case A_2/case B). E.g. emissions of aldehydes (E_ALD in CBM-Z) are mapped by taking 100% of acetaldehyde emissions, 100% of propianoldehyde and 50% of acrolein emissions for case B (jet fuel combustion), whereas for cases A_1 and A_2 no aldehydes are mapped (aldehydes result from burning of organic material). The factors of 0.315 and 0.035 by which air traffic NO_x emissions are mapped to NO and NO_2 for case 2 (H_2 combustion), respectively, result from an analogous 90%/10% split and a subsequent multiplication by 0.35 (0.9×0.35 = 0.315 and 0.1×0.35 = 0.035). This 0.35 represents the fraction of NO_x emitted by combusting H_2 instead of conventional jet fuel, and was taken from FCH JU [2020].

Figure 4.11 shows the outcome of the described procedure for air traffic emissions mapping for NO_x and $PM_{2.5}$. Those maps show the emission densities resulting from segment-wise mapping of the total AEM emission output to specific emission cases (see Table 4.4). Subsequent addition of the segment-dependent emissions yields the total emission profile for each scenario. Figure 4.11 shows that differences in NO_x and $PM_{2.5}$ emission densities are clearly larger between scenario III and scenario I than between scenario II and scenario I. Moreover, comparing Figure 4.11a with Figure 4.11e and Figure 4.11b with Figure 4.11f shows that whereas all $PM_{2.5}$ emissions are curbed in scenario III (Figures 4.11b and 4.11f are identical), not all NO_x emissions are curbed in scenario III, even though reductions are large.

[5] Hydrogen-based

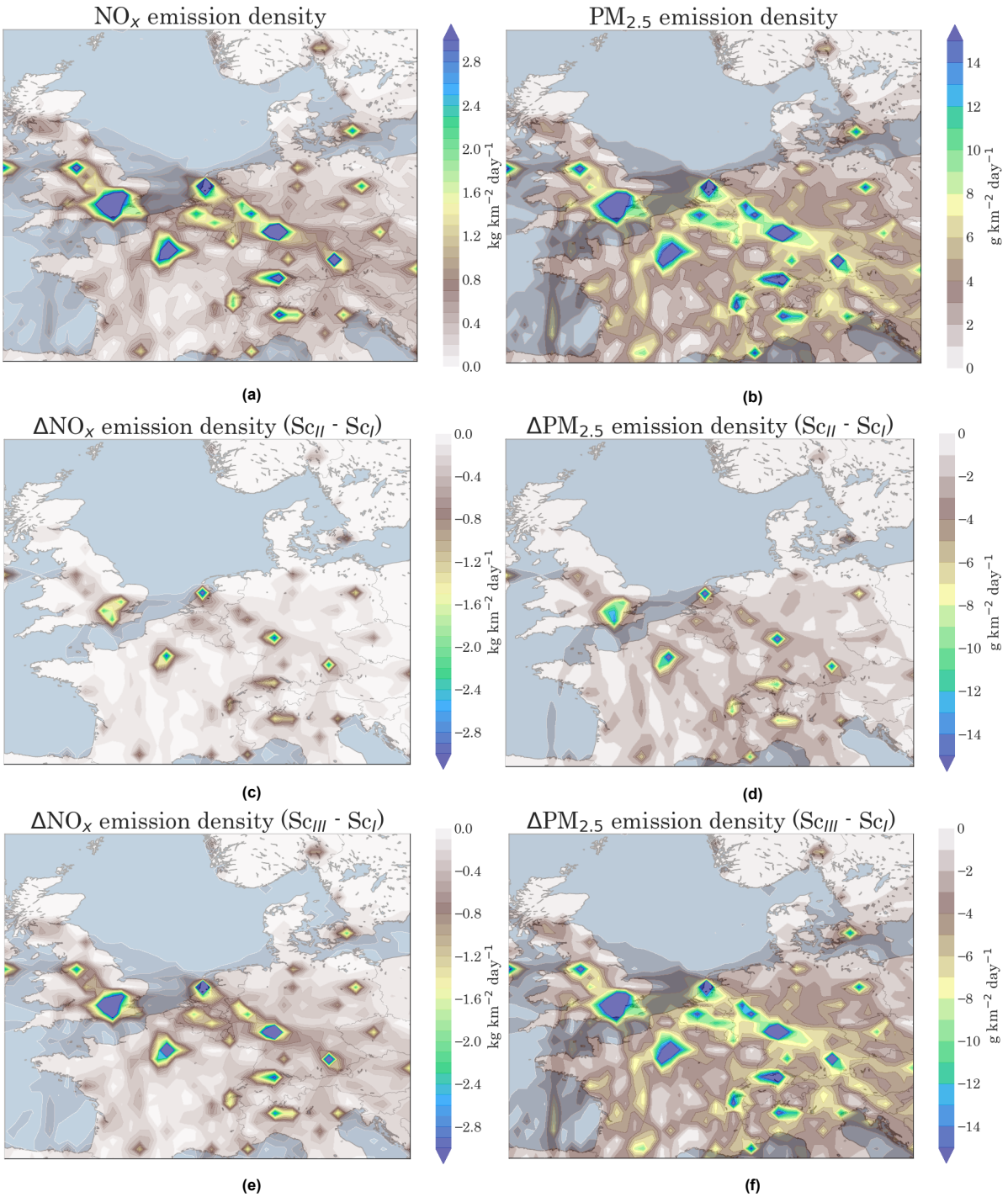

Figure 4.11. Spatial, column-total, NO_x (left) and $PM_{2.5}$ (right) air traffic emission density in kg km^{-2} day^{-1}. Figures **(a)** and **(b)** show absolute the emission density for scenario I (2019 aviation emissions). Figures **(c)** and **(d)** show the relative differences between scenarios I and II, visualizing the spatial effect of using electric fuel cell propulsion on short-haul flights (modeled as zero emissions). Figures **(e)** and **(f)** show the relative differences between scenarios I and III, visualizing the aggregate effect of using electric fuel cell propulsion on short-haul flights and H_2 combustion on medium and long-haul flights. Scenario IV is left out for convenience as there are no air traffic emissions associated with.

4.6. Air Quality Assessment

This section describes the followed approach in attaining the results described in Chapter 5. The setup of the WRF-Chem output evaluation is addressed in terms of:

- The way the scenarios from Section 4.4 are compared amongst each other (see Section 4.6.1).

The simulation of four scenarios leads to $\frac{4!}{2!(4-2)!} = 6$ pairs of scenarios of which the model output could be compared. Section 4.4 explains which of those scenario pairs is focused on to keep the results comprehensive and informative.

- The output variables that are used as a measure of air quality (see Section 4.6.2). Based on those variables conclusions can be drawn regarding air quality.
- Handling of the spatial domains described in Section 3.2 (see Section 4.6.3). Not all variables can be assessed on the same domains as some variables require higher spatial resolutions to be accurately resolved, and having a non-uniform grid in space yields biases as regions with more grid cells are weighting heavier in domain-wide statistics.

Finally, Sections 4.6.4, 4.6.5 and 4.6.6 describe the used metrics and techniques in assessing air quality.

4.6.1. Scenario Intercomparisons

The main purpose of this study is to quantify effects of H_2 propulsion on air quality. For this purpose, the scenarios described in Section 4.4 are used. Scenario I is referred to as the baseline scenario as it presents the aviation sector as it was in 2019. Scenario IV, with no air traffic emissions, has two use cases: a) it serves as the ideal situation in which aviation is disregarded or not causing any emissions, and b) it can be interpreted as a complete transition to flying on H_2 fuel cells where the amount of water emitted is constrained to the conventional jet fuel-case (scenario I). It should be noted achieving this scenario with H_2 fuel cells is currently considered infeasible [FCH JU, 2020]. Scenarios II and III are interpreted as intermediate steps towards a zero-emissions aviation sector, and are technically feasible according to FCH JU [2020]. The comparison between scenarios I and II quantifies the effect of only implementing H_2 fuel cell propulsion on short-haul flights, the comparison between scenarios II and III quantifies the additional effect of implementing H_2 combustion on the remaining sector (medium and long-haul flights), and the comparison between scenarios I and III quantifies the total effect of those two.

Table 4.5. Yield of intercomparison different scenarios for the purpose of this study.

	Scenario I	Scenario II	Scenario III	Scenario IV
Scenario I	-	**Air quality effect H_2 fuel cells for short-haul aviation**	**Air quality effect H_2 fuel cells for short-haul aviation & H_2 combustion medium & long-haul aviation**	**Maximum achievable air quality change from aviation**
Scenario II	**Air quality effect H_2 fuel cell propulsion for short-haul aviation**	-	Air quality effect H_2 combustion medium & long-haul aviation	Air quality impact of medium & long-haul aviation
Scenario III	**Air quality effect H_2 fuel cells for short-haul aviation & H_2 combustion medium & long-haul aviation**	Air quality effect H_2 combustion medium & long-haul aviation	-	Air quality impact of H_2 combustion propulsion for medium & long-haul aviation vs. no emissions
Scenario IV	**Maximum achievable air quality change from aviation**	Air quality impact of medium & long-haul aviation	Air quality impact of H_2 combustion for medium & long-haul aviation vs. no emissions	-

The information gained from the scenario intercomparisons are shown in Table 4.5. The intercomparisons in bold are the ones that are presented in the results (Chapter 5), as the other comparisons then become redundant. That means that scenarios II, III, and IV are compared with the 2019 emissions case - scenario I. Moving from scenario I towards scenario IV can be conceptually seen as a step-wise excursion from conventional jet fuel-based propulsion to cleaner H_2-based propulsion, whereby the directly emitted air pollutants are reduced at each step and the share of hydrogen fuel increases at each step.

4.6.2. Measure of Air Quality

Effects on air quality are analyzed looking at three compounds - the concentrations of nitrogen dioxide (NO_2), ozone (O_3), and fine particulate matter ($PM_{2.5}$) - in the lowest model layer. For convenience the mass concentrations of those compounds are converted from parts per billion volume to μg m^{-3}, using a molar mass of 46.01 g/mol for NO_2 and 48 g/mol for O_3. Assessment of air quality changes between scenarios are done both on the domain-wide scale as on local/regional scales. On the domain-wide scale, O_3 and $PM_{2.5}$ concentrations are evaluated on the entire study domain, while NO_2 is evaluated on the two inner domains with the highest resolution (d03 and d04). This is done because of the locality in NO_2 concentration peaks, related to its shorter atmospheric lifetime (order of minutes/hours). O_3 and $PM_{2.5}$ have longer lifetimes in the order of weeks and days, respectively, making particularly the detection of air quality guideline exceedances less sensitive to the modeling resolution as concentration peaks are less local. Vertically, only the concentrations in the lowest model layer, between 0 and 54 meters above the ground (see Table 4.3), are considered, as changes in this layer are most relevant to human health.

VOCs are evaluated additional to NO_2, O_3, and $PM_{2.5}$, due to their central role in the formation of ground level ozone (Section 2.1.2). Individual VOC species are part of the WRF-Chem output, of which a manageable selection is gathered and aggregated to get an approximation of the total VOC concentration. Thereby care is taken to select the most abundant VOC species, and those with the highest photochemical ozone creation potential (POCP), which is an indicator of the ozone concentration increment following an increment in the considered VOC species' concentration, relative to ethene [Altenstedt and Pleijel, 2000]:

$$\mathrm{POCP}_c = \frac{\Delta \mathrm{O}_{3_{\Delta c}}}{\Delta \mathrm{O}_{3_{\Delta ethene}}}. \tag{4.2}$$

Here c is the VOC species for which the POCP value is calculated. The following VOCs are included: acetaldehyde (C_2H_4O), benzaldehyde (C_7H_6O) and higher aldehydes, ethanol (C_2H_5OH), methanol (CH_3OH), dymethyl sulfide (C_2H_6S) and its oxidants, formaldehyde (CH_2O), hydrogen chloride (HCl), ketones ($R_2C{=}O$ group), methylglyoxal ($C_3H_4O_2$), isoprene (C_5H_8), ethene (C_2H_4) and other alkenes, acetic acid (CH_3COOH), toluene (C_7H_8), and xylene (C_8H_{10}).

4.6.3. Domain Aggregation and Regridding

As explained in Section 3.2, the model output is calculated for four nested domains, all with a different spatial resolution. For the sake of an unweighted domain-wide analysis that is better manageable, the data from each of those domains are aggregated, where the parameters at each location are defined by the most inner grid in which the location resides[6], and are subsequently regridded uniformly. In order not to lose information provided by the original grids, the entire study domain is interpolated onto the highest modeled resolution, belonging to d04 ($\sim 0.0158 \times 0.0158°$), yielding a grid of 1296×1026 cells for the full domain.

4.6.4. Time-Mean Output Analysis

Due to the variability of concentrations over time, driven not only by emissions and local chemistry but also by meteorological variability and transport, time-mean local concentrations are used mainly. This reduces some of the variability induced by meteorology and draws a clearer picture of the chemistry. Two-week mean concentrations are determined domain-wide, along with the spatial variations therein. In order not to rely on the underlying data distribution, which might not be Gaussian, the mean absolute deviance (MAD) is used as a measure of spatial variability instead of e.g. the standard deviation. The MAD is calculated as follows:

$$\mathrm{MAD} = \frac{\sum |x_i - \tilde{x}|}{N}, \tag{4.3}$$

[6] E.g. for a location in d04 where data from d01, d02, and d03 are also available, the data from d04 is used and the rest is omitted.

where N is the number of locations/grid cells, x_i is the mean concentration at location i and $\bar{x}$ is the mean concentration over the study domain. The sign of the change in MAD between one of the H_2 scenarios and the baseline scenario hence gives some information on whether alternative propulsion techniques accentuate spatial differences in air quality or rather relax those differences, which can be relevant for local compliance with air quality guidelines. The expectation is that most air pollution from aviation happens in the vicinity of airports, positively correlating with (densely) populated areas where more-than-average air pollution is expected. Therefore it is hypothesized that lower aviation-induced air pollution reduces spatial (domain-wide) air quality differences, possibly improving air quality at those locations where it is most needed.

In addition, local time-mean air quality is compared with the 2021 WHO air quality guidelines (AQGs) stated in Table 1.1. The WHO AQGs are considered instead of the EU guidelines as the WHO AQGs pose stronger demands on air quality and have been updated more recently. Time-mean concentrations on the simulation time length are compared with the annual NO_2 and $PM_{2.5}$ guidelines. An evaluation of intra-annual air quality variability to put this into perspective is presented in Section 6.3. Furthermore, short-term air quality is assessed comparing 24-hour WHO guideline concentrations for NO_2 and $PM_{2.5}$ with the daily average (14 for each location) concentrations from the model output. Also, maximum daily 8-hour mean O_3 levels are tested for compliance with the WHO guideline concentration of 100 μg m^{-3}. This is done by computing the 8-hour running mean ozone concentration at each location, filtering out the time windows that fall within a single (calendar) day, and comparing the daily maximum values with the WHO guideline concentration.

4.6.5. Reduction Potential

Related to the scenario intercomparison of time-mean air quality, differences in air quality will put the overall effect of aviation on air quality into a broad perspective. Besides this, this study aims to evaluate the possible gain of flying on H_2 on air quality changes that can be achieved looking only at the aviation sector. Therefore, a parameter referred to as the Reduction Potential (RP) is used in this study to quantify the change in time-mean concentrations for scenarios II and III, relative to scenario I, projected onto a scale defined by the difference in concentrations between scenario I and scenario IV. This difference is regarded as the ”maximum attainable air quality change” induced by the aviation sector, as it involves the difference between the most polluting case (scenario I) and the case without aviation emissions (scenario IV). Formally the concentrations corresponding with scenarios I and IV have a RP value of 0% and 100%, respectively. The RP values for scenarios II and III are calculated as follows for scenario s and compound c:

$$\mathrm{RP}_{s,c} = \frac{\bar{x}_{s=\mathrm{I},c} - \bar{x}_{s,c}}{\bar{x}_{s=\mathrm{I},c} - \bar{x}_{s=\mathrm{IV},c}} \cdot 100(\%), \tag{4.4}$$

where $\bar{x}$ once again represents the time-mean concentration over all locations. A RP between 0% and 100% for scenarios II and III thus indicate that the mean concentrations for those scenarios are in between those of scenarios I and IV, which is expected beforehand. The closer to 100%, the larger is the air pollution reduction of the respective scenario for the considered compound.

4.6.6. Assessment Local Air Quality

Based on Figures 4.11a and 4.11b, air traffic emissions are highly clustered around airport hubs within the aviation network. Accordingly, most changes in air quality are to be expected around those locations. Filtering out the 12 locations where the emitted mass of aviation fuel exceeds 70 tonnes per day within the lowest model layer[7] leaves 10 regions, see Figure 4.12. The selected regions have been assigned to airports in the same grid cell or in the direct vicinity. The names of the airports are indicated in Figure 4.12 by their International Air Transport Association (IATA) codes, which are linked with their respective airport name in Table 4.6. Local changes in NO_2, O_3, and $PM_{2.5}$ concentrations are evaluated at all of those locations. Total burned fuel mass is reported, to which the burned fuel mass in adjacent grid cells is added as not all burned fuel associated with an airport may fall exactly within one single grid cell.

[7] Under the influence of vertical transport, the associated ground air quality can not be purely assigned to emissions taking place within this lowest layer. Nevertheless only the emissions in the ground layer are considered for the selection of locations, as this is the simplest method together with the expectation that locations will not vary when incorporating the layers above as well.

Allocating the modeled changes in air quality and the burned fuel magnitudes strictly to the reported airports is assumptive, as aviation movements from other airports/platforms nearby may be intertwining. E.g. the burned fuel mass associated in this study with London Heathrow may contain for a part burned fuel mass from air movements to/from London Stansted or London Luton. For the analysis this is not relevant, and the reported airports should be regarded more as indicators of the geolocation than as effects strictly associated with that particular airport.

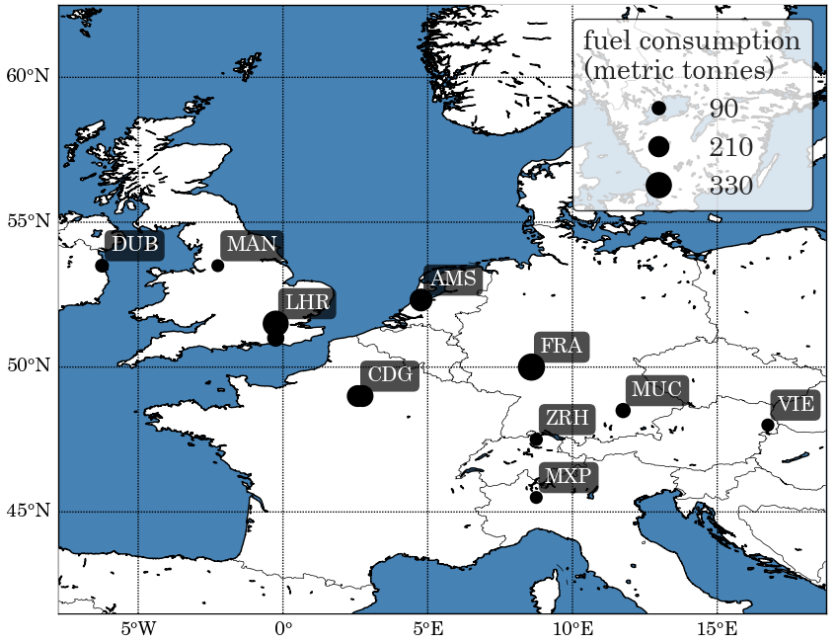

Figure 4.12. Grid cells within the study domain with the highest burned fuel mass (> 70 tonnes) within the lowest layer (0-54 m). Locations have been labeled with the corresponding airport responsible for majority of the fuel consumption. For the encircled grid cells, the fuel consumption is added as those are adjacent cells which complement to the total emissions and air quality near the associated airports.

Table 4.6. IATA airport code to airport name.

IATA	Airport
ZRH	Zurich
FRA	Frankfurt
MUC	Munich
MAN	Manchester
LHR	London Heathrow
AMS	Amsterdam Schiphol
DUB	Dublin
MXP	Milan Malpensa
CDG	Paris Charles de Gaulle
VIE	Vienna

Various studies have been conducted addressing the effect of air traffic on air quality in the vicinity of airports. Riley et al. [2021] reports that a vast majority of conducted studies finds clear airport signatures on local air quality within 20 km from the airport, and Yim et al. [2015b] found that about one-third of premature deaths caused by aviation is attributable to exposure of mainly O_3 and $PM_{2.5}$ within 20 km from an airport. The inner domains - d03 and d04 - have been designed such that changes in air quality in the vicinity of airports can be evaluated as a function of distance from the airport. Major concentration peaks are expected to be resolved on the respective spatial resolutions, while the grid cells of d01 and d02 are around or larger than 20 km. This assessment is done on the largest airports within d03 and d04 - Amsterdam Schiphol, Eindhoven, and Rotterdam-The Hague Airport.

Conversion Cartesian to Polar grid

Converting the Cartesian grid obtained from the model output to a Polar grid, centered at the airport from which air quality changes are assessed, aids in the representation of air quality changes as a function of distance (radius) from the airport. In this way, all locations in a circumference with radius r from the airport are defined by grid points. This polar grid takes five input arguments: the center location P (longitude and latitude), radius r, radial distance between nodes d, and the number of angular directions n_θ in which nodes are defined. An example is shown in Figure 4.13a for $n_\theta = 5$, $d = 3$ km, and $r = 15$ km, centered at Eindhoven Airport. A more continuous picture of local air quality centered around P is created when $d \to 0$ and $n_\theta \to \infty$, even though the original resolution poses a limit on the gain from a reduction (increase) of d (n_θ). Figure 4.13b shows the used case with $n_\theta = 500$ and $d = 1$ km, where additionally the difference in time-mean NO_2 concentrations between scenarios I and IV are projected onto the grid points. At each node distance from the center, the mean change in air pollutant concentrations is computed together with the 95% confidence interval of the mean, in order to draw conclusions on air quality changes as a function of the distance from the airport.

Radius of Airport Pollution (RAP)

The distance from the airport at which the airport signature on air quality can be seen is referred to in this study as the radius of airport pollution (RAP). The RAP is influenced by more factors than merely by local aviation-induced emissions, such as atmospheric transport, and chemistry that is not (directly) related to the activity at the considered airport. The RAP is determined both visually and relying on statistical analysis. Statistical analysis tools are used that quantify the probability of finding deviating concentration differences from the mean difference (domain-wide) at a certain distance from each airport. First, the data distributions of air quality changes on a respective area including the airport are tested for normality by generating Quantile-Quantile plots (visual inspection) and by performing the Shapiro-Wilk test and the D'Agostino's K^2 test, with the null hypothesis being that the concentration distributions are Gaussian. Both tests are conducted as they have different underlying parametrizations that might result in different conclusions regarding the null hypothesis. When the area passes the normality tests, the mean concentration difference within the area is defined as the background concentration difference. Successive deviations from this background mean concentration difference that are statistically significant, starting at the airport and moving away from it, define the statistically-based RAP. "Significant deviations" depends on a set significance level, for which 0.2 is chosen. The mean concentration difference at locations at a fixed distance from each airport are converted to a Z-score, indicating the number of standard deviations from the mean. Those Z-scores are then converted to p-values assuming a Gaussian distribution, which are compared with a set significance level. The distance at which the p-value first exceeds the 0.2 significance level (one-tailed for NO_2 and $PM_{2.5}$, two-tailed for O_3) - starting at each airport - is used as a definition of the RAP.

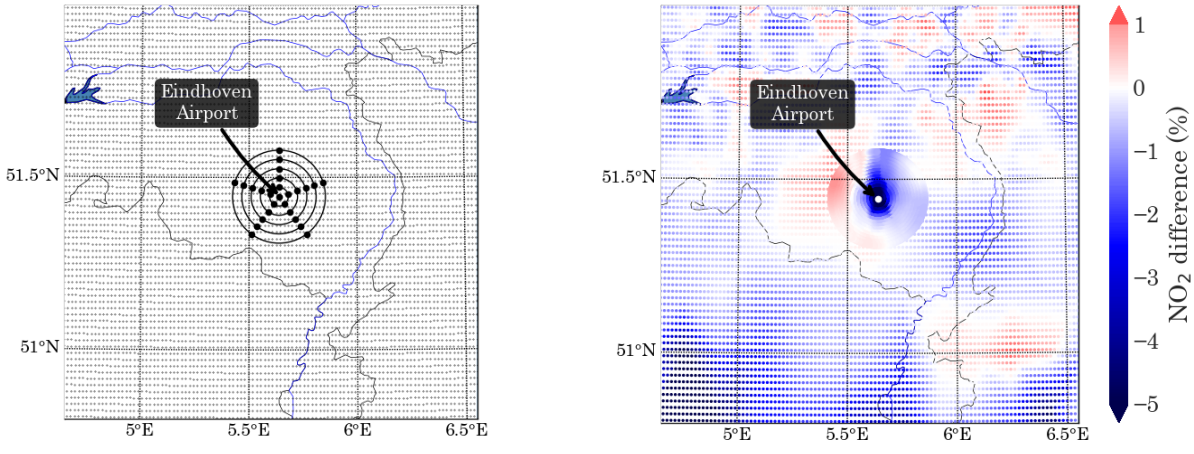

(a) $n_\theta = 5$, $d = 3$ km, $r = 15$ km

(b) $n_\theta = 500$, $d = 1$ km, $r = 15$ km

Figure 4.13. Conversion from a Cartesian grid (small dots) to a polar grid (large dots), centered at a defined location - Eindhoven Airport in this example. The right plot **(b)** shows the relative difference (%) in NO_2 concentrations between scenarios I and IV mapped on a color scale in addition to a higher polar grid density.

4.7. Model Evaluation Metrics

This section presents the validation approach of the simulated results with in-situ observational data. The model validation is presented in Chapter 6. Because of the countless metrics that exist to evaluate model performance and the number of variables evolved in the presented validation, a combination of metrics is sought for that can be graphically and textually combined and that allow for a direct comparison on model accuracy between variables. Taylor [2001] proposed the use of a so-called Taylor Diagram to graphically show Pearson's correlation coefficient (R) and the centered root mean squared error (CRMSE) between model and observations, along with the standard deviations (σ) of model and observations. The utility of the Taylor diagram will be shown next.

The model output and observational data (at each location) is denoted here by M and O, respectively. E.g. $\bar{O}$ represents the mean of the observational data. The root mean squared error (RMSE) is used to quantify the deviation of the model output from the observations:

$$\text{RMSE} = \sqrt{\frac{\sum_{n=1}^{N}(M_n - O_n)^2}{N}}, \tag{4.5}$$

Where N is the number of observations at each location. Locations with less than 50 hourly observations during the fortnight simulation period are excluded. The RMSE can be decomposed into a part explaining differences in means between observations and model output, referred to as bias, and a part explaining differences in the patterns from both data sets. The bias is expressed as the mean bias error (MBE) and is calculated as follows:

$$\text{MBE} = \frac{\sum_{n=1}^{N}(M_n - O_n)}{N} = \bar{M} - \bar{O}. \tag{4.6}$$

The difference in the pattern between model output and observations, which can be seen as the RMSE corrected for bias, is referred to as the CRMSE:

$$\text{CRMSE} = \sqrt{\frac{1}{N}\sum_{n=1}^{N}\left(\left(M_n - \bar{M}\right) - \left(O_n - \bar{O}\right)\right)^2}. \tag{4.7}$$

And hence $\text{RMSE}^2 = \text{MBE}^2 + \text{CRMSE}^2$. In addition, Pearson's correlation coefficient R is a normalized metric between -1 and 1 indicating how well the modeling results co-vary (linearly) with the observational data. A R of 1 (-1) indicates a perfectly linear correlation (anti-correlation), while 0 indicates no correlation. It is calculated dividing the covariance by the product of the standard deviations:

$$R = \frac{\frac{1}{N}\sum_{n=1}^{N}(M_n - \bar{M})(O_n - \bar{O})}{\sigma_M \sigma_O}. \tag{4.8}$$

The Taylor diagram is based on the fixed relationship between the CRMSE, R, σ_M and σ_O as can be mathematically derived from Equations 4.7 and 4.8:

$$\text{CRMSE}^2 = \sigma_M^2 + \sigma_O^2 - 2\sigma_M \sigma_O R, \tag{4.9}$$

which shows a similarity with the law of cosines ($c^2 = a^2 + b^2 - 2ab\cos\phi$). This shows that the magnitudes of the CRMSE, σ_M, and σ_O can be represented graphically by a length/distance and R by an (azimuthal) angle, see Figure 4.14.

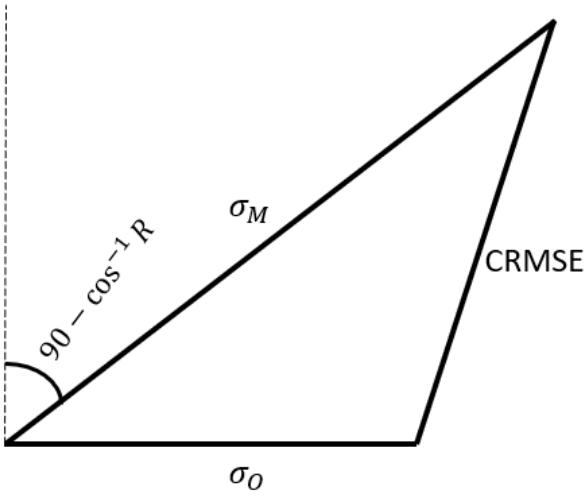

Figure 4.14. Geometric representation of CRMSE, R, σ_M, and σ_O. Modified from Taylor [2001].

Usually, Taylor diagrams contain one data point for the observation and one data point for each model, by which different models could be compared. The Taylor diagrams shown in Chapter 6 are however used to show one single model performance, at different locations within the study domain which are each represented by one point in the Taylor diagram (and whereby each point has its corresponding set of observational data). Thereby the Taylor diagram is normalized by σ_O, such that 1) all observation points coincide at a distance of unity on the x-axis (σ_O/σ_O), 2) the y-axis represents the ratio of the standard deviations (σ_M/σ_O) and 3) the distance between the observational data points at ($r = 1$, $\theta = \pi/2$) and each point/location is the normalized CRMSE (NCRMSE):

$$\text{NCRMSE} = \frac{\text{CRMSE}}{\sigma_O} = \frac{1}{\sigma_O}\sqrt{\frac{1}{N}\sum_{n=1}^{N}\left(\left(M_n - \bar{M}\right) - \left(O_n - \bar{O}\right)\right)^2} = \sqrt{\left(\frac{\sigma_M}{\sigma_O}\right)^2 + 1 - 2\frac{\sigma_M}{\sigma_O}R}. \tag{4.10}$$

The use of those normalized Taylor diagrams, also referred to as modified Taylor diagrams, follow the approach set in Elvidge et al. [2014] and are used to visually represent the correlation coefficient R (Equation 4.8), the NCRMSE (Equation 4.10), and the ratio of spread (standard deviation) of observations and model output at all locations where measurements are available and for all variables. The error component that the modified Taylor diagram fails to represent is the model bias (and the total error), which is reported separately by means of the MBE (Equation 4.6) and RMSE (Equation 4.5). To visually compare those errors among variables, the normalized versions of those metrics are preferred, for which is it common practise to use the mean of the observational data (in absolute terms) as was done by Kärnä and Baptista [2016]:

$$\text{NMBE}(\%) = \frac{\sum_{n=1}^{N}(M_n - O_n)}{\sum_{n=1}^{N}|O_n|} \cdot 100(\%) = \frac{\bar{M} - \bar{O}}{\bar{O}} \cdot 100(\%), \tag{4.11}$$

$$\text{NRMSE}(\%) = \sqrt{\frac{\sum_{n=1}^{N}(M_n - O_n)^2}{\sum_{n=1}^{N}|O_n|}} \cdot 100(\%). \tag{4.12}$$

A final notion relates to R, which can indicate the level of covariance between observations and modeling results but does not indicate the similarity in magnitude of both time series [Duveiller et al., 2016]. Duveiller et al. [2016] propose the use of a dimensionless, symmetric quantity called Willmott's Index of Agreement (IOA), bounded between 0 and 1, that does incorporate the relative magnitudes of the modeled and observed data [Willmott, 1981]. A value of 0 indicates no agreement between both, a value of 1 indicates perfect agreement. It is computed by Equation 4.13. This metric is considered principally to

assess the model output quality, even though R is more useful from a visualization perspective (Taylor diagram). In addition, the R metric indicates anti-correlations[8] whereas IOA does not. Therefore, both R and IOA are reported.

$$\mathrm{IOA} = 1 - \frac{\sum_{n=1}^{N} \left(M_n - O_n\right)^2}{\sum_{n=1}^{N} \left(\left|M_n - \bar{M}\right| + \left|O_n - \bar{O}\right|\right)^2}. \tag{4.13}$$

In summary, R, σ_M/σ_O, and NCRMSE are presented in modified Taylor diagrams, and NMBE and NRMSE are presented graphically aside to show the model bias. The MBE, CRMSE, and RMSE are reported textually to quantify the absolute errors, and IOA is reported to indicate the overall agreement between model and observations.

[8] Even though a negative correlation would lead to conclude a poor model performance, just as for a low (positive) correlation.

5

Results

The intercomparison between the output of the four WRF-Chem runs discussed in Section 4.4 are presented in this chapter, adhering to the methodology discussed in Section 4.6. The time mean, spatial-variant model output is discussed in Section 5.1, which includes a domain-wide assessment of time mean local air quality to WHO guidelines (Sections 5.1.2, 5.1.3, and 5.1.4). Local air quality changes in the vicinity of major airports within the study domain (Section 5.2.1) and at Rotterdam-The Hague, Eindhoven, and Amsterdam Schiphol Airport (Section 5.2.2) are discussed in Section 5.2. To where applicable, the graphical output relating to scenario I is consistently shown in (dark)grey, whereas the H_2 scenarios - II, III, and IV - are displayed in steel blue, deep sky blue/cyan, and dark blue, respectively, unless stated otherwise.

5.1. Time mean Air Quality Assessment

An intercomparison of two-week mean air quality between scenarios is presented in Section 5.1.1. Time mean data over specific time windows are used to compare short-term air quality with WHO guidelines, which is described in Sections 5.1.2, 5.1.3, and 5.1.4.

5.1.1. Two-Week Mean NO_2, O_3, and $PM_{2.5}$ Concentrations

The two-week mean - from June 1st till June 14th 2019 - nitrogen dioxide (NO_2), ozone (O_3) an fine particulate matter ($PM_{2.5}$) concentrations are shown in Figure 5.1 for all scenarios. The concentrations are also presented in Table 5.1 accompanied between parentheses with the relative change in time mean concentration compared to scenario I (2019 aviation emissions). domain mean differences between scenarios are small and are limited to a couple of permilles, which shows the limited mean effect of aviation on overall air quality. As will be shown later, much larger air quality differences are seen locally between scenarios. Still, for all three compounds, domain-wide, time mean air quality improvements are achieved consistently when moving from the baseline scenario to short-haul flights on H_2 fuel cells (scenario II), to short-haul flights on H_2 fuel cells and medium and long-haul flights on H_2 propulsion (scenario III), to all flights on H_2 fuel cells (scenario IV), in that order. This can be most clearly seen in Figure 5.1 where concentrations along aviation's decarbonization path monotonically decrease for all three compounds. Having modified only the air traffic-related emissions between scenarios, make it convincing that those consistent reductions in air pollutants are attributable to air traffic.

Table 5.1. Time mean, domain mean concentration (μg m^{-3}) per scenario. The entire (aggregated and interpolated) study domain is taken.

	NO_2	O_3	$PM_{2.5}$
Sc_I	8.686	75.259	8.249
Sc_{II}	8.667 (-2.3‰)	75.216 (-0.6‰)	8.233 (-1.9‰)
Sc_{III}	8.658 (-3.3‰)	75.146 (-1.5‰)	8.202 (-5.8‰)
Sc_{IV}	8.636 (-5.7‰)	75.135 (-1.6‰)	8.183 (-8.1‰)

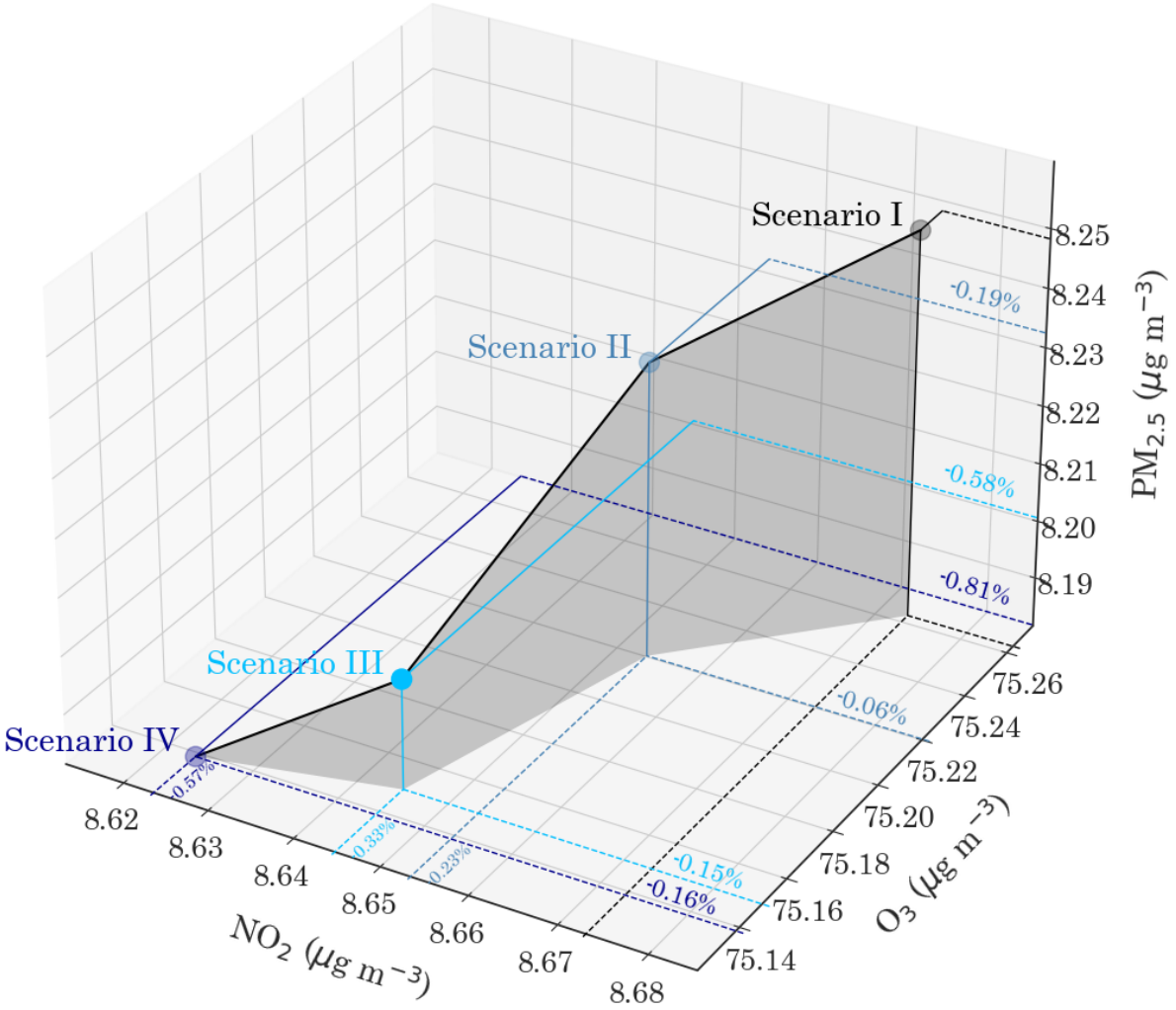

Figure 5.1. The decarbonization path of the aviation sector shown graphically. Absolute concentrations are shown on the axes, with relative differences in concentrations (%) between the hydrogen scenarios and the baseline scenario shown within the graph.

Figure 5.2 shows the time mean concentrations of all three compounds for scenario I (Figures 5.2a, 5.2c, and 5.2e) on a spatial map and the difference between scenarios I and IV (Figures 5.2b, 5.2d, and 5.2f). The latter plots are not included for scenarios II and III but show a highly similar spatial pattern, with slightly lower magnitudes than for scenario IV.

Figure 5.2a shows the locality of NO_2 concentrations, with elevated concentrations at the west coast of the Netherlands and Belgium, extending to London, and at the Ruhr area in Germany, one of Europe's largest industrial and metropolitan areas. The metropolitan region of Paris, together with the Swedish city Gothenburg (an industrial city with one of Europe's largest freight ports) also stand out. Finally, high NO_2 concentrations are found at Stuttgart-Frankfurt - Germany's financial center with high traffic density and the heart of the automotive industry. The mentioned regions are the ones where largest reductions in NO_2 concentrations are observed too, except from Gothenburg where low-level air traffic emissions are much smaller. Comparing Figure 5.2b with Figures 5.2d and 5.2f (color scales are identical) clearly shows that differences in NO_2 concentrations remain much more local than changes in O_3 and $PM_{2.5}$. This can be attributed to the longer atmospheric lifetime of O_3 (order of hours to weeks) and the longer residence time of $PM_{2.5}$ (order of days) compared to NO_2 (order of minutes to hours), making NO_2 less subject to long-range transport. To show the locality in NO_2 concentrations, it is found that 50% of the total variation in NO_2 concentrations between scenario I (2019 aviation emissions) and scenario IV (no aviation emissions) is taking place within a 25 km perimeter from the 50 airports where aviation emissions are highest. Those surface areas sum to merely 2.7% of the total study area. In other words,

Sc_I: baseline (2019 emissions), Sc_{II}: H_2 fuel cells & jet fuel combustion, Sc_{III}: H_2 fuel cells & H_2 combustion, Sc_{IV}: H_2 fuel cells

in 2.7% of the study area, 50% of the NO_2 variations are seen between scenarios.

Local time mean O_3 concentrations (see Figure 5.2c) are highly varying within the study domain, ranging from below 50 μg m^{-3} to above 100 μg m^{-3}, with elevated concentrations in some more remote areas around the borders of the study domain (the Alps, Mediterranean Sea and the Atlantic). Local minima in O_3 arise in highly industrialized areas such as Paris and main parts of England, where there is an apparent anti-correlation between O_3 and NO_2. This anti-correlation is even more clearly visible when comparing Figures 5.2d and 5.2b, which are anti-correlated with a correlation coefficient R of -0.77. Thereby, 59% of the perceived spatial variation in changes of O_3 concentrations can be explained by changes in NO_2 concentrations. The remaining variation can be attributed to changes in other chemical compounds - mainly carbon monoxide (CO) and volatile organic compounds (VOCs) - as well as meteorology. Section 5.2 elaborates on this matter.

Time mean background ground-level $PM_{2.5}$ concentrations and spatial differences in ground-level $PM_{2.5}$ concentrations are shown over the study domain in Figures 5.2e and 5.2f, respectively. The mean wind field is shown on top of those figures to illustrate the dependence of the wind field on local $PM_{2.5}$ concentrations. The relatively high concentrations in Eastern Europe and particularly above the Italian peninsula can be associated with the near-stagnant wind circulation in those regions (see Figure 5.2e), in combination with a low planetary boundary layer height (PBLH) (see Figure 5.3), conditions known for the north of Italy [Vecchi et al., 2004]. Those factors obstruct horizontal and vertical mixing of pollutants, respectively, leading to ground-level accumulation. Figure 5.2f shows that differences in $PM_{2.5}$ concentrations between scenarios I and IV coincide with regional changes in the wind field. The net convergence (divergence) of the wind, caused by e.g. increases (decreases) in wind speed more downstream (upstream) or even complete turning of the wind vector induce relative accumulation (dispersion) of air pollutants.

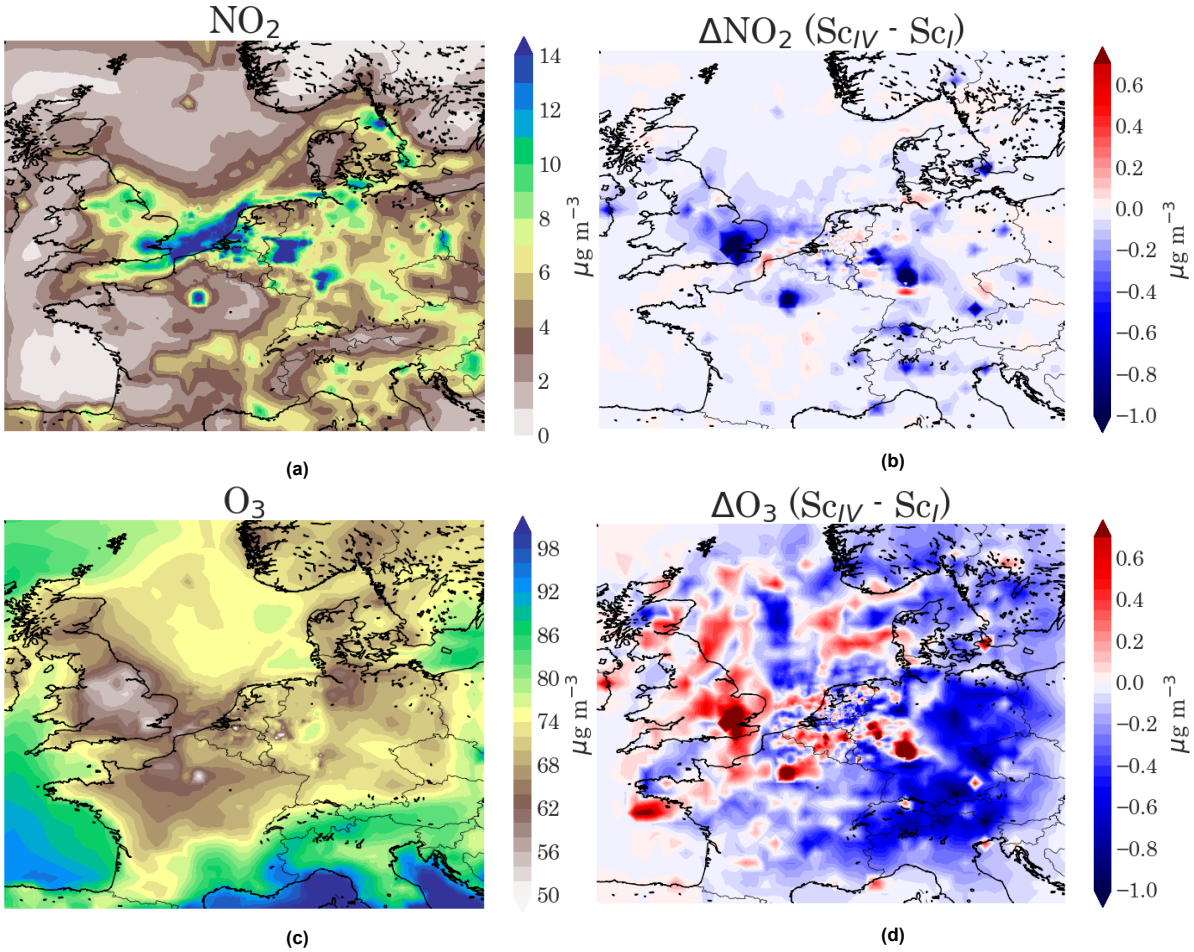

Figure 5.2. cont'd on next page

Sc_I: baseline (2019 emissions), Sc_{II}: H_2 fuel cells & jet fuel combustion, Sc_{III}: H_2 fuel cells & H_2 combustion, Sc_{IV}: H_2 fuel cells

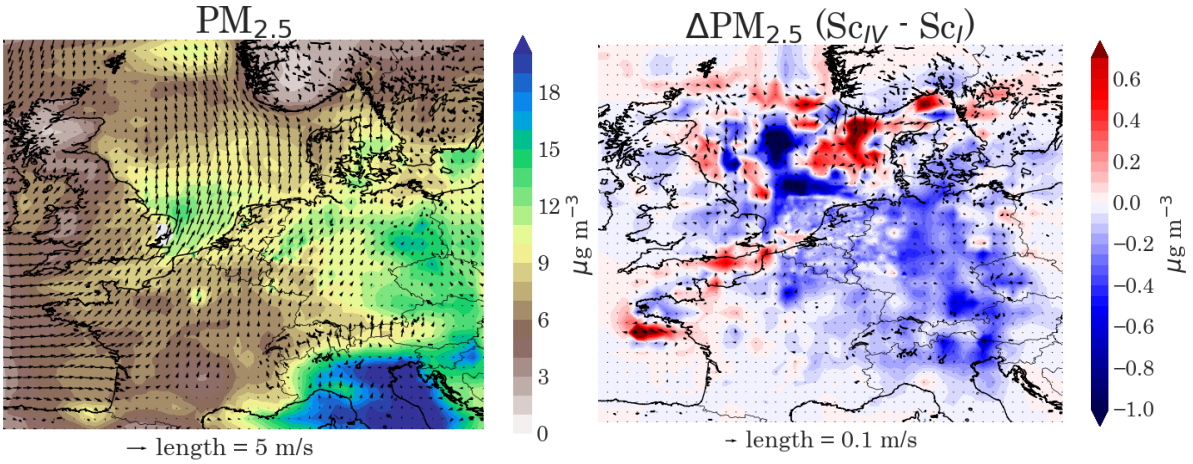

Figure 5.2. Time mean air quality at ground level (0-54 m), evaluated by nitrogen dioxide (**a** and **b**), ozone (**c** and **d**) and fine particulate matter (**e** and **f**). Left: time mean concentrations for scenario I (2019 aviation emissions). Right: difference in time mean concentrations between scenario IV (no aviation emissions) and scenario I. The entire study domain is shown, interpolated onto a uniform grid with the highest spatial resolution from d04. **e** and **f** additionally show time mean wind vectors indicating the direction and magnitude of the wind, for scenario I and for scenario IV relative to scenario I, respectively. Plots comparing scenario II and scenario III with scenario I are highly similar and therefore not shown.

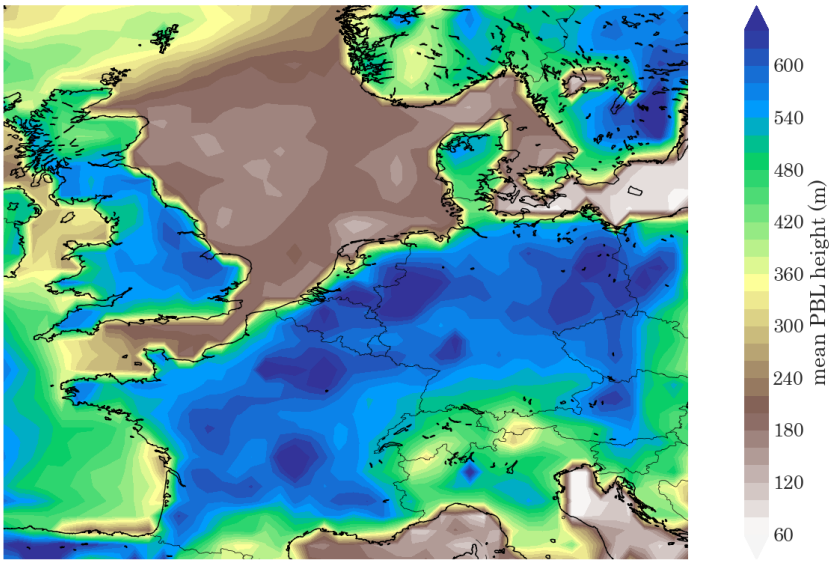

Figure 5.3. Time mean Planetary Boundary Layer Height (PBLH) for scenario I. Units are in meters.

From Figure 5.2 it can be deduced that 2019 air traffic can be held responsible for local increases in NO_2 concentrations, local accumulation/destruction of O_3 through atmospheric chemistry (further reduction of O_3 in O_3-depleted regions such as London and Paris) and changes on larger spatial scales through atmospheric transport, and regional changes in fine particulates, driven by transport. The mean absolute deviance (MAD) - representing the mean absolute deviance from the time mean, domain mean concentrations - clearly show that spatial gradients of time mean concentrations get smaller for NO_2 and $PM_{2.5}$ when curbing air traffic emissions (see Table 5.2). For O_3, the domain mean differences between scenarios are negligible.

Table 5.2. Mean Absolute Deviance (MAD) of time mean concentration (μg m^{-3}) per scenario.

	NO_2	O_3	$PM_{2.5}$
Sc_I	2.116	6.825	3.001
Sc_{II}	2.104 (-5.3‰)	6.820 (-0.7‰)	2.983 (-5.8‰)
Sc_{III}	2.090 (-12.3‰)	6.832 (+1.1‰)	2.964 (-12.4‰)
Sc_{IV}	2.083 (-15.4‰)	6.825 (-0.0‰)	2.954 (-15.4‰)

The observed differences in the distribution of considered species' concentrations can be reasoned from the fact that air traffic is responsible for local increases in NO_2 at places where concentrations may already be high (generally major airport hubs are located within or near large cities with high pollution rates), thereby increasing the mean deviance from the domain-wide mean and contributing to more extreme pollution events. Aviation adds to the total concentration of $PM_{2.5}$ which can locally accumulate or disperse, mainly driven by the wind field. The overall sign of O_3 changes is less clear than for NO_2 and $PM_{2.5}$ due to local chemical conditions (as will be discussed later). From Table 5.1 it is also observed that the time mean, domain mean differences in O_3 concentrations between scenarios are smaller compared to NO_2 or $PM_{2.5}$. This can also be attributed to the fact that O_3 locally increases whereas it decreases at other locations.

The Reduction Potential (RP) is used as a metric to show the relative effect of H_2 propulsion on air quality compared to the no aviation emissions case, as explained in Section 4.6. The feasible H_2 scenarios - scenarios II and III - are projected onto the range of mean concentrations between the most extreme scenarios - 2019 aviation emissions (scenario I) and no aviation emissions (scenario IV). This results in the RP values shown in Figure 5.4. The fact that NO_x is still being directly emitted in scenario III, while direct emissions of $PM_{2.5}$ and VOCs (another precursor of O_3 together with NO_x) are no longer emitted in scenario III, possibly explains why the RP value for NO_2 is lower for scenario III (57%) than for O_3 and $PM_{2.5}$ (91% and 72%, respectively). This also explains the difference in RP for all three compounds between scenarios II and III. In scenario II, 31.9% of all NO_x emissions are curbed originating from short-haul flights (see Figure 4.10). Of the remaining 68.1% NO_x emissions from the medium and long-haul segments, 65% is curbed in scenario III by combusting H_2 instead of conventional jet fuel. Hence, the total reduction in NO_x emissions in scenario III is 76.1%. Figure 4.10 shows that $PM_{2.5}$ and HC (relevant for O_3) emissions from aviation are reduced by 37.8% and 49.3% in scenario II, respectively. However, in scenario III there are no $PM_{2.5}$ or HC emissions. The larger difference in reduction potential of O_3 and $PM_{2.5}$ than of NO_2 in scenario III compared to scenario II can thus be reasoned from the fact that differences in emission reductions are larger for $PM_{2.5}$ and the precursors of O_3 than for NO_2 between the two scenarios. Even though there are no direct emissions of $PM_{2.5}$ from aviation in scenario III, the emission of NO_x by the H_2 combustion process might still contribute to the formation of secondary aerosols (nitrates). This explains why the RP for scenario III is found to be around 72% instead of (near) 100%. Yet, a large improvement of nearly half the scale between scenarios I and IV is made going from scenario II to III. Similarly, the emission of NO_x in scenario III still contributes to some photochemical O_3 production.

Sc_I: baseline (2019 emissions), Sc_{II}: H_2 fuel cells & jet fuel combustion, Sc_{III}: H_2 fuel cells & H_2 combustion, Sc_{IV}: H_2 fuel cells

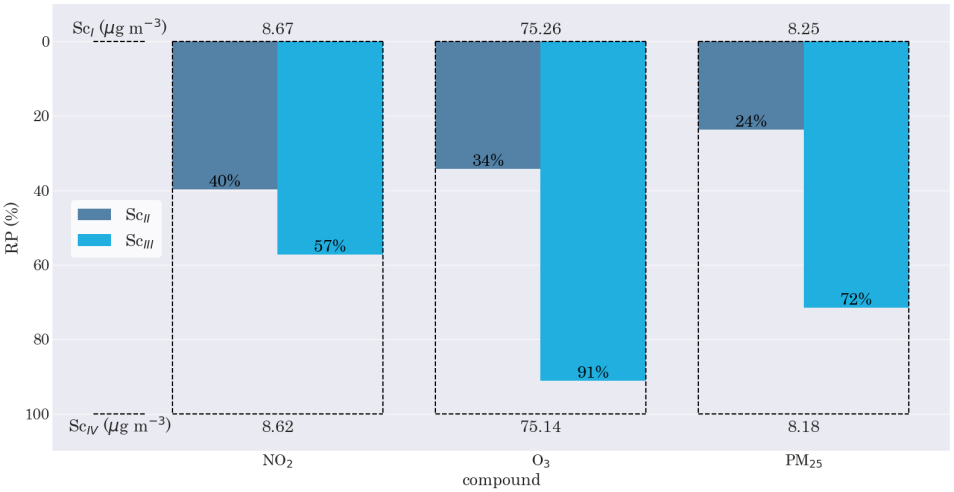

Figure 5.4. Two-weekly mean concentrations of nitrogen dioxide, ozone and fine particulate matter compared for different scenarios, using the Reduction Potential (RP) metric. The 0% and 100% RP scores correspond to the time mean concentrations from scenario I and scenario IV, respectively.

Figure 5.5 zooms in further onto the various compounds constituting fine particulate matter. Black carbon (or soot), organic carbon, nitrate, sulfate, sodium, ammonium, and other inorganics add up to on average 77% of the total $PM_{2.5}$ mass. The remainder is grouped under the name ”other fine PM”. Even though the differences between scenarios of individual contributions to $PM_{2.5}$ are minor, and the indicated percentages should be taken as indicative, Figure 5.5 clearly exposes the compounds that are involved in aviation emissions and those that are not. Organic carbon and sodium concentrations do not show any statistically significant variation between scenarios, where the negative percentages associated with the RP values for scenarios II and III are deceiving due to minor absolute differences in mean concentrations between scenarios. Both compounds are of biogenic origin and are hence not associated with aviation emissions. The other compounds, having RP values within the 0-100% window, are mainly of anthropogenic origin. In line with the aforementioned explanation involving the emission of NO_x in both scenario II and scenario III, the smallest air quality improvements are seen on the nitrate compound in Figure 5.5.

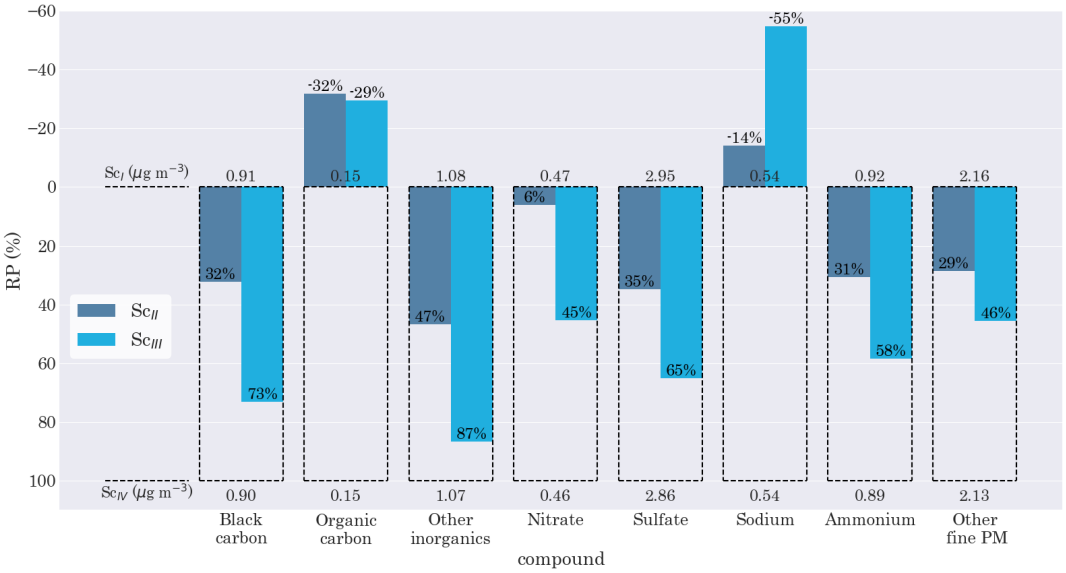

Figure 5.5. Time mean concentrations of individual fine particulate matter compounds compared for different scenarios, using the Reduction Potential (RP) metric. The 0% and 100% RP scores correspond to the time mean concentrations from scenario I and scenario IV, respectively. The absolute time mean, domain mean concentrations are shown correspondingly along the horizontal.

5.1.2. Two-Week Mean NO_2 and $PM_{2.5}$ Concentrations versus WHO Guidelines

The discussed time mean concentrations in Section 5.1.1 are discussed further in this section by looking at individual locations and comparing those local time mean values with WHO guideline concentrations [WHO, 2021]. More precisely, the two-week mean concentrations for NO_2 and $PM_{2.5}$ are compared with the annual WHO guideline concentrations, being 10 μg m^{-3} for NO_2 and 5 μg m^{-3} for $PM_{2.5}$ as stated in Table 1.1. As the two-week simulation time is much shorter than the annual time scale on which the annual WHO guideline concentrations are based and concentrations might fluctuate intra-annually, Section 6.3 elaborates on this aspect.

Figure 5.6 shows a kernel density estimate of the time mean distribution of NO_2, where the proportion of locations exceeding the 10 μg m^{-3} annual WHO guideline concentration is hatched. Those data only span the two inner domains (d03 and d04), as the spatial resolution of those domains are considered sufficiently high to resolve the highly local concentration patterns observed for NO_2. In around 32% of locations within the study domain, the WHO guideline concentration is exceeded by the two-week mean concentration, with slight differences up to a couple of permilles between scenarios, decreasing with lower air traffic emissions as could be expected. Yet, differences between scenarios are small. The mode and median concentrations are well below the WHO guideline concentration. The rug plot on the bottom of each plot shows the mean values at individual locations, indicating the two-week mean concentrations extend to approximately 30 μg m^{-3} in the most extreme cases. As can be seen from Figure 5.8a, the regions responsible for the most extreme NO_2 concentrations are the cities of Rotterdam and Antwerp - both industrial hubs with large harbors - and the western edge of the Ruhr. In none of those locations aviation is the main source of air pollution. In fact, concentrations found within those regions are hardly affected by different scenarios except the direct vicinity of airports. The green locations indicated in Figure 5.8a show which locations exceeded the WHO guideline concentration in scenario I, while remaining below the guideline concentration in scenario IV. The background concentration at those locations are all found to be close to 10 μg m^{-3} in the 2019 emissions case. Those are the locations explaining the differences in locations exceeding WHO guideline concentrations between scenarios. Local NO_2 concentrations at Amsterdam Schiphol and Rotterdam-The Hague Airport in scenario I are far above the NO_2 guideline (14.2 and 17.6 μg m^{-3}, respectively), while at Eindhoven Airport the NO_2 concentration is well below the guideline (8.6 μg m^{-3}). At all those locations the WHO guideline concentration is either exceeded - in case of Amsterdam Schiphol and Rotterdam-The Hague - or met - in case of Eindhoven - both in scenario I and in scenario IV, even though the largest concentration differences between scenarios are found at those locations. Those airports are analyzed in more detail in Section 5.2.2.

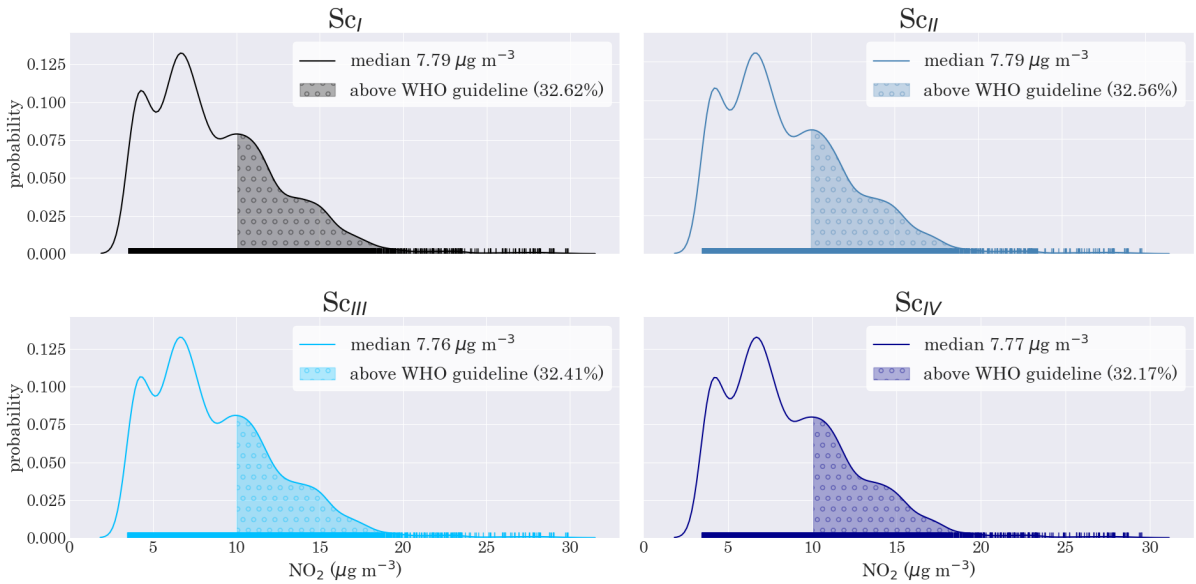

Figure 5.6. Kernel Density Estimate (KDE) showing the probability of two-week mean NO_2 concentrations for all four scenarios. The median values are reported, together with the percentage of locations that exceed the 10 μg m^{-3} WHO guideline concentration for annual mean NO_2 concentrations (hatched regions in KDE plots). Included locations are from the most inner domains (d03 and d04).

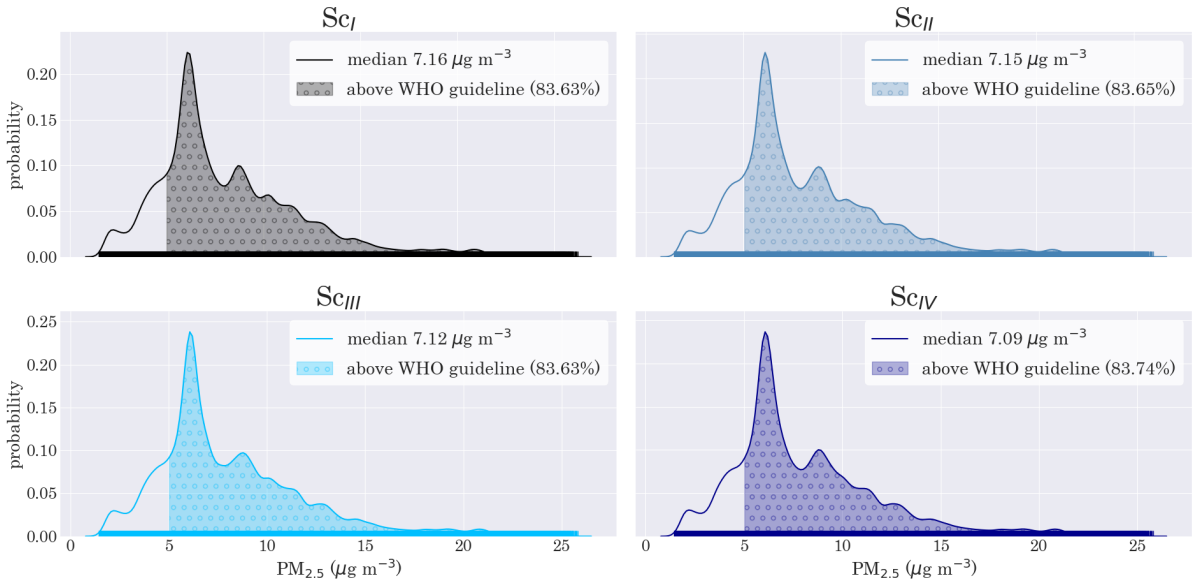

Figure 5.7. Kernel Density Estimate (KDE) showing the probability of two-week mean $PM_{2.5}$ concentrations for all four scenarios. The median values are reported, together with the percentage of locations that exceed the 5 μg m^{-3} WHO guideline for annual mean fine particulate matter concentrations (hatched regions in KDE plots). Included locations are from all domains, interpolated onto a uniform grid with the highest spatial resolution from d04.

Similar plots are shown for the two-week mean concentration of $PM_{2.5}$ with its corresponding WHO guideline concentration of 5 μg m^{-3}, shown in Figure 5.7. For $PM_{2.5}$, the lower resolution data from d01 and d02 are also included (albeit those data has been interpolated linearly along with data from d03 and d04) as the resolution of peak concentrations are less local than is the case for NO_2. Mode and median values are in this case above the WHO guideline concentration, and as Figure 5.7 reveals, the vast majority (around 84%) of locations are not complying with the newest annual WHO AQGs. Small overall differences in $PM_{2.5}$ concentrations between scenarios and the longer residence time (and transportation) of $PM_{2.5}$ compared to NO_2 make it possible that in scenario IV more locations exceed the guideline concentration than in the case of 2019 emissions. This is hence a direct consequence of the interplay of atmospheric dynamics overshadowing the gain of less fine particulate emissions by flying on hydrogen. Figure 5.7 shows that large emission reductions are needed for $PM_{2.5}$ concentrations to be reduced to below the WHO guideline concentration. Reductions in aircraft emissions can, at the most, contribute a small part of this.

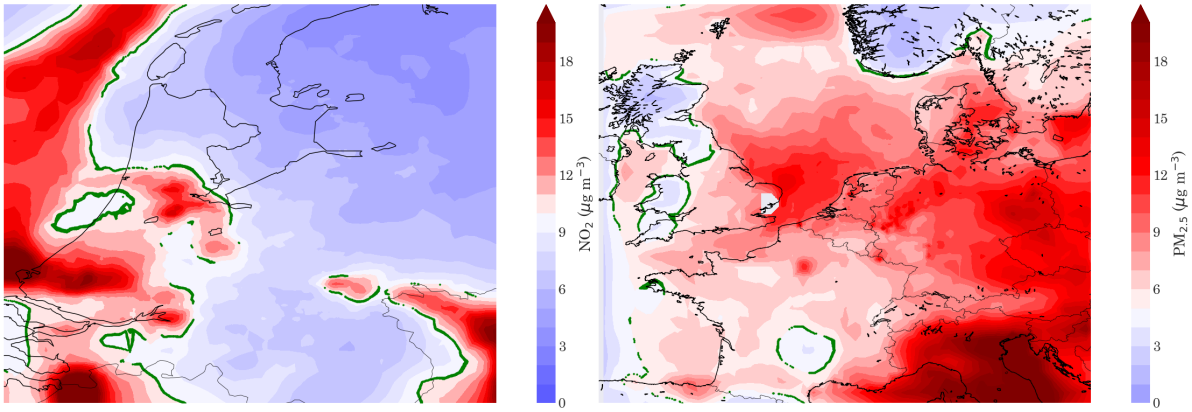

(a) d03 and d04 **(b)** all domains

Figure 5.8. Domains involved in Figures 5.6 and 5.7, showing the time mean concentrations for scenario I (**(a)** NO_2 and **(b)** $PM_{2.5}$). Locations where concentrations are above (below) the WHO guideline concentrations are red (blue), which are 10 μg m^{-3} for NO_2 and 5 μg m^{-3} for $PM_{2.5}$. The green dots are locations where the WHO guideline concentration is exceeded in scenario I but complied with in scenario IV.

5.1.3. 24-Hour Mean NO_2 and $PM_{2.5}$ Concentrations versus WHO Guidelines

Recent evidence shows that short-term (daily) exposure to high concentrations of NO_2 and $PM_{2.5}$ have a higher impact on human morbidity and mortality than previously thought [WHO, 2021]. In 2021, the WHO revised the previous 24-hour mean concentration guideline of 25 μg m^{-3} from 2005 to a guideline of 15 μg m^{-3} for $PM_{2.5}$ [WHO, 2021]. For NO_2, on the other hand, no previous 24-hour mean guideline was formulated. The current guideline concentration is set at 25 μg m^{-3}. The 99th percentile rule of exceedance applies to both NO_2 and $PM_{2.5}$, meaning that it is recommended to restrict local exceedance days to a maximum of 3-4 days per year.

Starting with NO_2, at each location within the research domain, the modeled NO_2 concentrations are compared with the newest 24-hour WHO guideline by computing the daily mean concentrations during the simulation period (June 1st till June 14th). Again the data from d03 and d04 are used. The overall results are shown in Table 5.3. The individual number of WHO guideline exceedances (combining all 24-hour means at all locations) are in the order of a couple of permilles, similar to the proportion of locations where the guideline is being exceeded at least once during the fortnight simulation period. In most of those locations, the guideline concentration is being exceeded during four or more days, with a mean of 9-10 days exceeding the guideline (out of 14). The 0.33-0.35% of locations exceeding the guideline four days or more already violates the 99th percentile guideline by the WHO in merely two weeks. At all of the other locations, information should be gained on the intra-annual variability of daily mean concentrations to draw conclusions on local short-term air quality. This is done in Section 6.3. For this study, differences between scenarios in short-term air quality regarding NO_2 are found to be minor.

Table 5.3. Exceedance of NO_2 24-hour mean guideline concentration of 25 μg m^{-3}. Table shows the local exceedances as a percentage of all 24-hour mean values at all locations, and the percentage of geographical locations N where the guideline value is exceeded ($C > AQG$) at least once or at least four times during the simulation time, respectively. Also, the mean number of exceedances for individual locations where the guideline value is exceeded at least once is shown (rounded to days).

	Individual exceedances of total [%]	Locations where $N_{C>AQG} \geq 1$ [%]	Locations where $N_{C>AQG} \geq 4$ [%]	Mean number of exceedances per location in the $N_{C>AQG} \geq 1$ group
Sc_I	0.29	0.43	0.35	9
Sc_{II}	0.29	0.43	0.34	10
Sc_{III}	0.29	0.41	0.34	10
Sc_{IV}	0.28	0.44	0.33	9

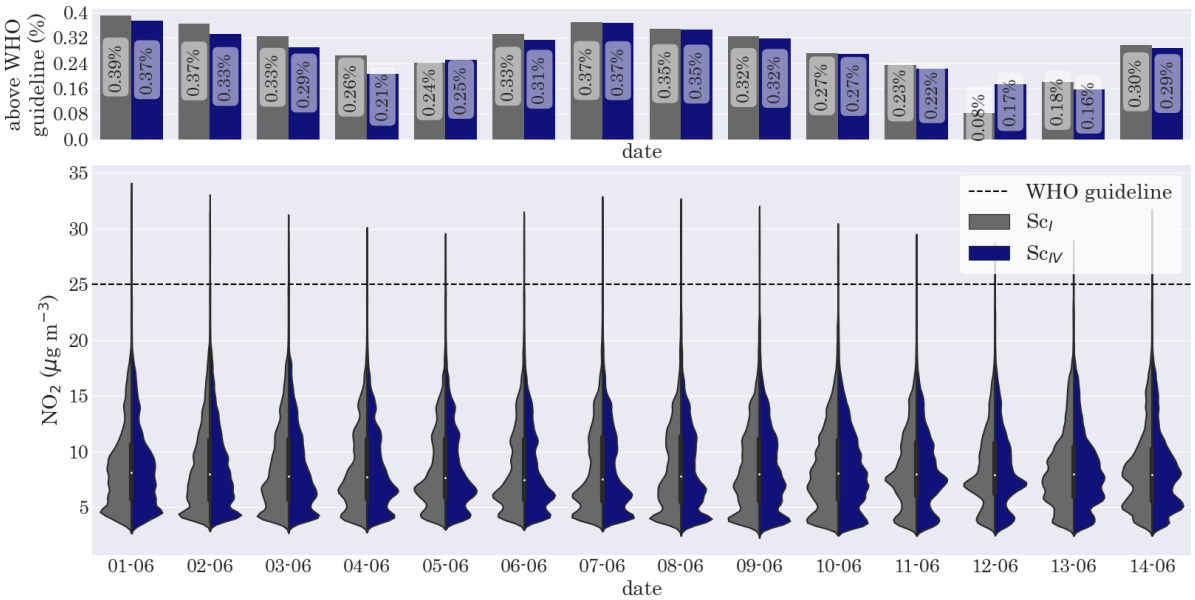

Figure 5.9. Time series showing the daily mean NO_2 distribution for the study domain on each day during the simulation, for scenarios I and IV. The spatial distribution is shown as kernel density estimate, with a simplified boxplot showing the median value (of two runs combined) as a white dot and the inter-quartile range as a black box. The WHO guideline concentration of 25 μg m^{-3} is indicated as a dashed line. Op top the percentage of locations exceeding the WHO guideline concentration is shown for that day. Plots for scenarios II and III are highly similar and are shown in Appendix D, Figure D.1.

Figure 5.9 shows, in addition to Table 5.3, the daily mean time series for NO_2 with all locations in d03 and d04 represented as a kernel density estimate, and the WHO guideline concentration indicated to show the proportion of each distribution falling below and above the guideline. On all days the vast majority (over 99%) of locations exhibit NO_2 concentrations that are well below the AQG level, with slight inter-daily fluctuations. Despite the inter-daily variations in the concentration distribution, most distributions are (close to) bi-modal, possibly due to the dichotomy in rural and urban background concentrations.

Short-term air quality related to $PM_{2.5}$ is falling short at more locations within the study domain than for NO_2 (during the simulated period of the year), as can be deduced from Table 5.4 and Figure 5.10. Even though the locations exceeding the AQG concentration of 15 μg m^{-3} are rigid over time, the differences between scenarios are clearer than for NO_2. Despite being in the order of permilles, the number of locations exceeding this short-term AQG concentration decreases with decreasing air traffic emissions of air pollutants. From the presented data it is concluded that nearly 7% of locations do not comply with the 99th percentile short-term AQG on a yearly basis by virtue of a two-week simulation in June. This percentage is likely higher when considering different periods of the year where $PM_{2.5}$ concentrations tend to be higher (e.g. during winter months). For a discussion on this, see Section 6.3.

Table 5.4. Exceedance of $PM_{2.5}$ 24-hour mean guideline concentration of 15 μg m^{-3}. Table shows the local exceedances as a percentage of all 24-hour mean values at all locations, and the percentage of geographical locations N where the guideline value is exceeded ($C > AQG$) at least once or at least four times during the simulation time, respectively. Also, the mean number of exceedances for individual locations where the guideline value is exceeded at least once is shown (rounded to days).

	Individual exceedances of total [%]	Locations where $N_{C>AQG} \geq 1$ [%]	Locations where $N_{C>AQG} \geq 4$ [%]	Mean number of exceedances per location in the $N_{C>AQG} \geq 1$ group
Sc_I	6.24	7.55	6.87	12
Sc_{II}	6.19	7.54	6.84	12
Sc_{III}	6.13	7.45	6.77	12
Sc_{IV}	6.11	7.44	6.73	12

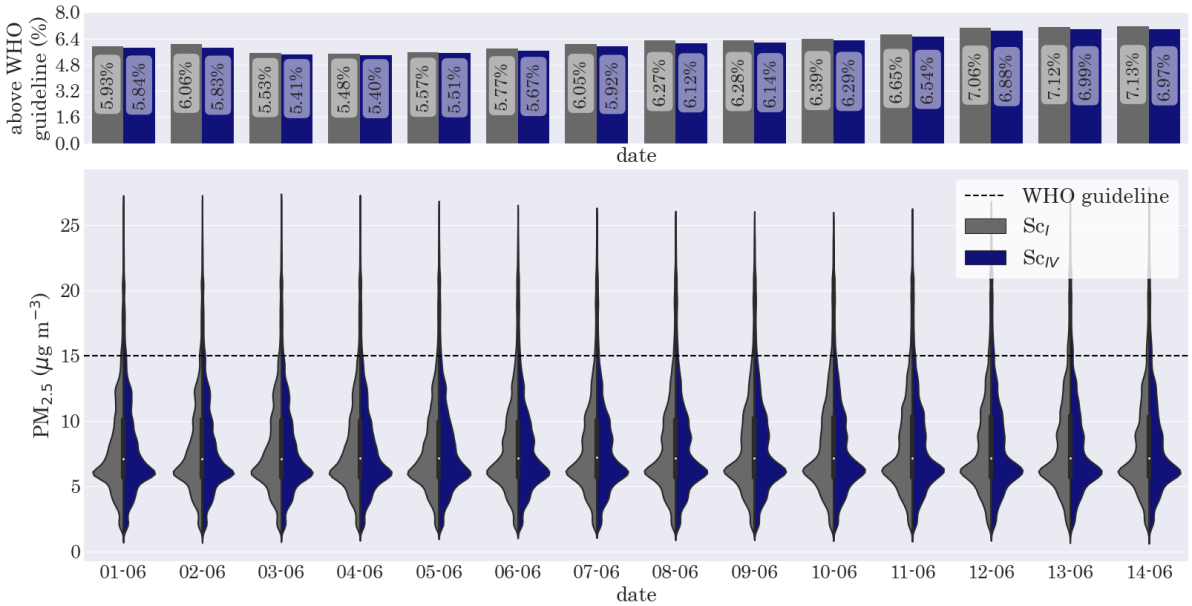

Figure 5.10. Time series showing the daily mean $PM_{2.5}$ distribution for the research domain on each day within the simulation time, for scenarios I and IV. The spatial distribution is shown as kernel density estimate, with a simplified boxplot showing the median value (of two runs combined) as a white dot and the inter-quartile range as a black box. The WHO guideline concentration of 15 μg m^{-3} is indicated as a dashed line. On top the percentage of locations exceeding the WHO guideline value is shown for that day. Plots for scenarios II and III are highly similar and are shown in Appendix D, Figure D.2.

5.1.4. 8-Hour Mean O_3 Concentrations versus WHO Guidelines

The final assessment regarding air quality by comparison with AQG levels is related to short-term O_3 concentrations. The 8-hour running mean approach explained in Section 4.6 yields daily maximum 8-hour O_3 concentrations which are summarized in Figure 5.11. Inter-daily variations in those maximum 8-hour O_3 concentrations are much higher than for the daily mean NO_2 and $PM_{2.5}$ concentrations, with two peaks occurring between June 7th and June 9th and from June 13th. On those days, a large number of locations do not comply with the AQG level of 100 μg m^{-3}, which is more than one-quarter of locations on June 14th. Those high O_3 episodes indicate the sensitivity of the study period to the evaluation presented here. The total AQG concentration exceedance in the case of O_3 again shows a dependency on aviation-induced air pollution, as the number of locations overshooting the AQG level decreases monotonically for air traffic scenarios in which less air pollutants are being emitted. This happens in spite of the observation from Figure 5.2 that O_3 concentrations increase locally at some locations where NO_2 concentrations decrease. At nearly half of the locations, the AQG level is being exceeded at least once, and at less than half of those locations the AQG level is exceeded on four days or more. Still, at approximately one out of five locations the 3-4 exceedance days per year allowance has already been reached within the two simulated weeks. What this means on a yearly timescale is again discussed in Section 6.3.

Table 5.5. Exceedance of the daily maximum 8-hour mean O_3 guideline concentration of 100 μg m^{-3}. The local exceedances as a percentage of all daily maximum 8-hour mean values at all locations are shown, and the percentage of geographical locations N where the guideline concentration is exceeded ($C > AQG$) at least once or at least four times during the simulation time. Also, the mean number of exceedances for individual locations where the guideline concentration is exceeded at least once is shown (rounded to days).

	Individual exceedances of total [%]	Locations where $N_{C>AQG} \geq 1$ [%]	Locations where $N_{C>AQG} \geq 4$ [%]	Mean number of exceedances per location in the $N_{C>AQG} \geq 1$ group
Sc_I	13.36	45.36	20.24	4
Sc_{II}	13.25	45.13	20.01	4
Sc_{III}	13.15	44.89	19.93	4
Sc_{IV}	13.09	44.59	19.77	4

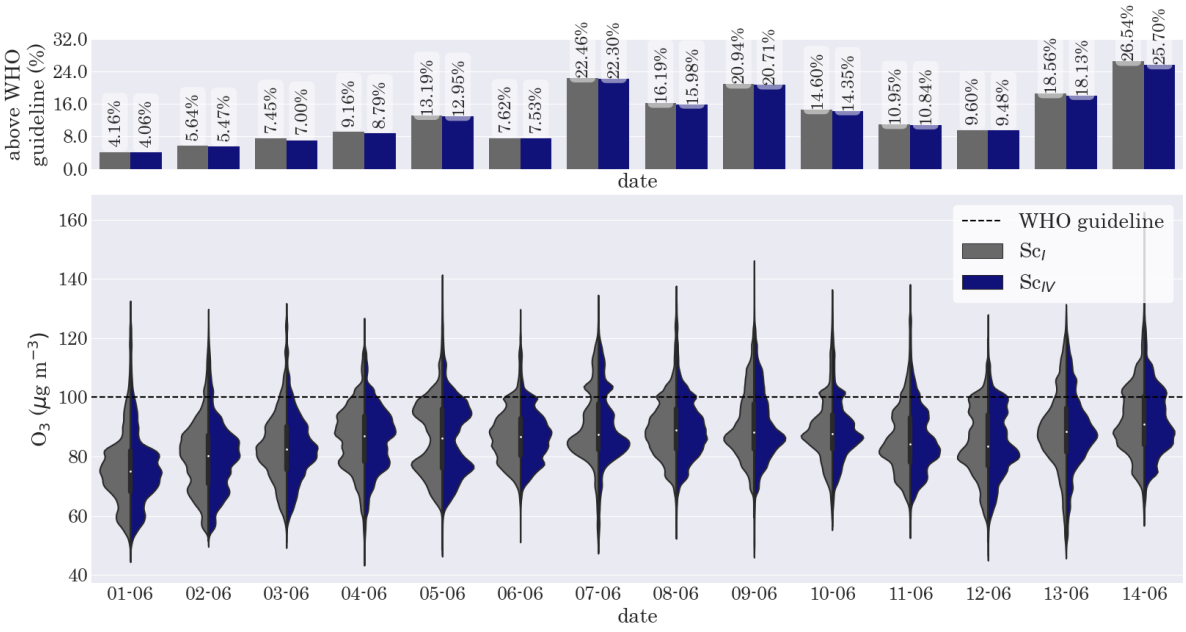

Figure 5.11. Time series showing the daily maximum 8-hour mean O_3 distribution for the study domain on each day of the simulation, for scenarios I and IV. The spatial distribution is shown as kernel density estimate, with a simplified boxplot showing the median value (of two runs combined) as a white dot and the inter-quartile range as a black box. The WHO guideline concentration of 100 μg m^{-3} is indicated as a dashed line. On top the percentage of locations exceeding the WHO guideline concentration is shown for that day. Plots for scenarios II and III are highly similar and are shown in Appendix D, Figure D.3.

5.2. Local Air Quality Changes Near Airports

Section 5.1 focused on the intercomparison of scenarios analyzing air quality domain-wide. This section presents the modeling results focusing on local air quality, there where largest changes in air quality are observed. As surface air quality is regarded, those changes take place predominantly in the vicinity of airports where most low-level air traffic movements are found.

5.2.1. Air Quality Changes at Ten Major Airports

In merely 2% of all locations within the entire study domain, air traffic takes place between ground level and approximately 60 meters. Air traffic at those locations are assumed to be directly related to landing, take-off and taxi practises at an airport within that same grid cell[1]. At all those locations, the amount of fuel burned by air traffic is being used as a proxy for airport size, i.e. when referring to the ”largest airports”, those locations are meant where aviation fuel consumption is highest.

At the ten largest airports within the study domain, all associated with a total daily fuel consumption from aviation of at least 70 metric tonnes, the changes in nitrogen dioxide, ozone, and fine particulate concentrations are analyzed between scenarios. At all locations, the NO_2 concentrations in the hydrogen scenarios are calculated to be lower than in scenario I, reductions varying from merely 0.3% at Vienna in scenario II to 25.2% at London Heathrow in scenario IV. The only exception where NO_2 concentrations are higher in a hydrogen scenario, is scenario II at Manchester where NO_2 concentrations are 0.50% higher than in scenario I. The changes in air quality for different scenarios at Manchester Airport are shown in Figure 5.12c. Similarly, $PM_{2.5}$ concentrations are observed to be lower everywhere in all hydrogen scenarios except from Manchester, where fine particulates are more abundant in all three hydrogen scenarios compared to scenario I. Later in this section the case of Manchester will be elaborated on.

Overall, largest changes in air quality are observed at Frankfurt Airport, for which the changes in air quality are shown in Figure 5.12a. Background NO_2 concentrations decrease monotonically with 7.48%, 18.19% and 25.13% compared to scenario I when going from scenario II to scenario IV. Similarly, background $PM_{2.5}$ concentrations decrease monotonically by 1.71%, 2.30% and 2.43%. For O_3, the opposite behavior is observed - O_3 concentrations increase monotonically when going from scenario II to scenario IV. On the contrary, Munich Airport, shown in Figure 5.12b, is an example of an airport where O_3 concentrations decrease monotonically, along with monotonic decreases in NO_2 and $PM_{2.5}$ concentrations. Hence, regarding the evolution of O_3 concentrations, two distinct behaviors are observed:

- The first airport grouping includes Frankfurt, London Heathrow, Dublin, Charles de Gaulle Paris, Amsterdam Schiphol, Zurich, and Manchester Airport. At those airports, reductions in NO_2 concentrations for each scenario are associated with local increases in O_3 concentrations (and vice versa, in the case of Manchester in scenario II). Examples of this behavior are shown for Frankfurt and Manchester Airport in Figures 5.12a and 5.12c, respectively.
- The second grouping includes Milan Malpensa, Munich, and Vienna Airport. At those airports, reductions in NO_2 concentrations are associated with reductions in O_3 concentrations. An example of this behavior is shown in Figure 5.12b for Munich Airport.

The airports that are not shown in Figure 5.12 are shown in Appendix E. The results at Vienna and Amsterdam Schiphol Airport are inconsistent with the rest as O_3 concentrations do not monotonically increase or decrease going from scenario II to IV. Still, all locations show that air quality improves in terms of $PM_{2.5}$ and NO_2 when flying on hydrogen. Comparing scenarios II, III, and IV, major local air quality improvements are made at each step moving away from the 2019 emission case. However, the relative impact on air quality of each step is different for each airport.

Looking at individual cases, Manchester Airport deviates the most from other locations as 1) NO_2 concentrations are higher during scenario II than during scenario I and 2) the $PM_{2.5}$ concentration is lower in scenario I than in the hydrogen scenarios as pointed out before. A possible underlying mechanism is that, when differences in emissions (from aviation) compared to the background concentrations are relatively small, possible effects on air quality are more likely to be masked out by meteorological effects. First of all, Manchester Airport is amongst the smallest airports of the ten analyzed airports.

[1] Section 4.6 explains how is dealt with cases in which this assumption might not be true.

Furthermore, focusing on scenario II, Manchester Airport has the smallest proportion of short-haul departing or arriving flights out of the ten discussed airports[2]. Those factors could explain why changes in aviation emissions moving away from the baseline scenario would be less pronounced and possibly overshadowed by meteorological effects at Manchester.

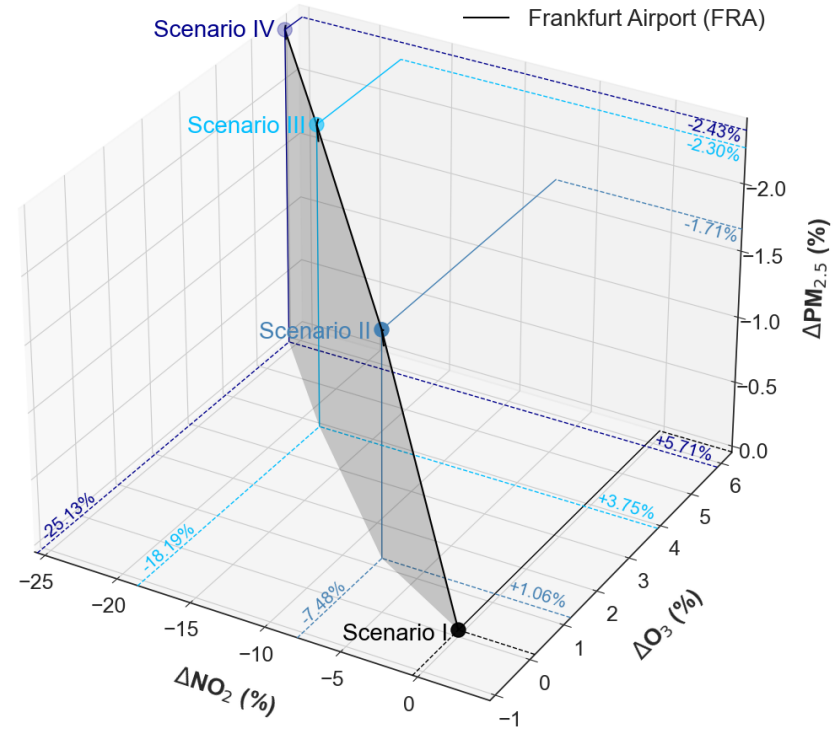

(a)

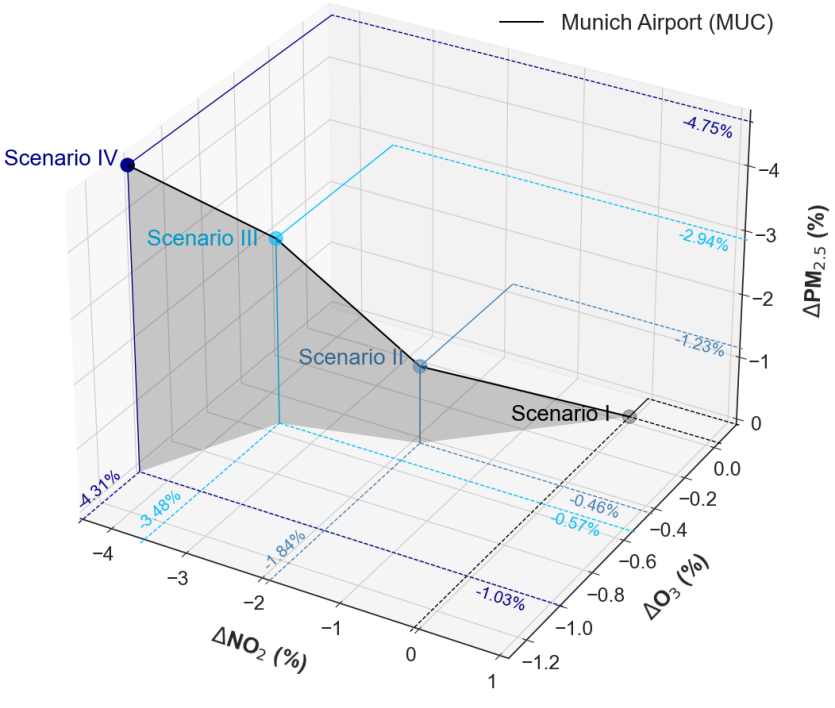

(b)

Figure 5.12. cont'd on next page

[2]37% of all departing/arriving flights At Manchester Airport are classified as short-haul, while the average for all ten airports is at 58%.

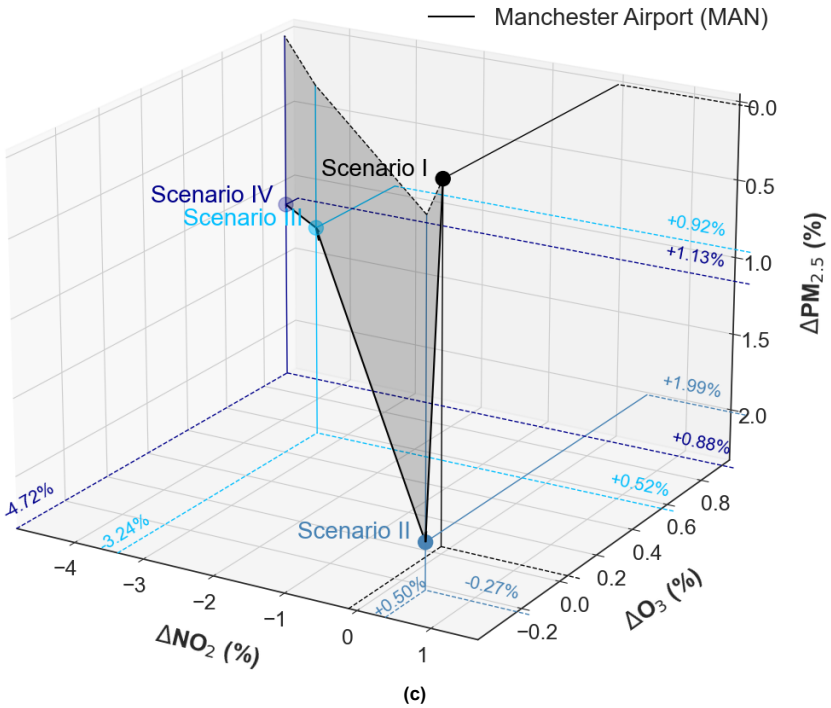

(c)

Figure 5.12. Changes in air quality shown for the hydrogen scenarios (scenarios II, III, and IV) at three of the ten largest airports within the study domain - **(a)** Frankfurt Airport, **(b)** Munich Airport, and **(c)** Manchester Airport. Relative differences in background concentrations for each compound compared to the baseline scenario are shown. Note that the z-axis (showing $PM_{2.5}$) has been reverted in all plots for visualization purposes. The remaining airports are shown in Appendix E.

Figure 5.13 shows a breakdown of $PM_{2.5}$ into its different compounds (see Section 5.1.1) for the three airports with highest associated fuel consumption - Charles de Gaulle, Frankfurt, and London Heathrow Airport - and for Manchester Airport. The graph once again shows that total $PM_{2.5}$ concentrations are lowest in scenario I at Manchester. This is however not linked to one particular compound. Both primary and secondary fine aerosols are most abundant in scenario II, followed by scenarios IV and III. Thereby the possibility of ascribing the contrasting pattern in $PM_{2.5}$ concentrations found at this location solely to local chemistry (forming secondary aerosols) is excluded, as the observed increase in primary aerosols relative to scenario I must be related to transport or other meteorological effects.

Figure 5.14 shows for each scenario the modeled wind direction at Manchester Airport, based on hourly horizontal wind components, along with the mean wind speed from each direction. Local changes in the wind field are minor between scenarios. The dominant wind direction is from the south-west, with westerlies being strongest on average. Intercomparing regional[3] NO_2 and $PM_{2.5}$ concentrations between scenarios leads to the conclusion that the elevated concentrations of pollutants in the H_2 scenarios are highly wind-driven for the Manchester case. Winds regionally converge above the Irish Sea in the H_2 scenarios compared to scenario I followed by accumulation of NO_2 and $PM_{2.5}$, which is blown towards Great-Britain by the westerlies causing higher pollutant levels. Another plausible explanation is the observation that the average wind speed in scenario I at Manchester Airport is slightly higher (0.02-0.03 m/s) than for the other scenarios, causing different levels in transport of air pollutants.

[3]Within a radius of 100 km from the airport.

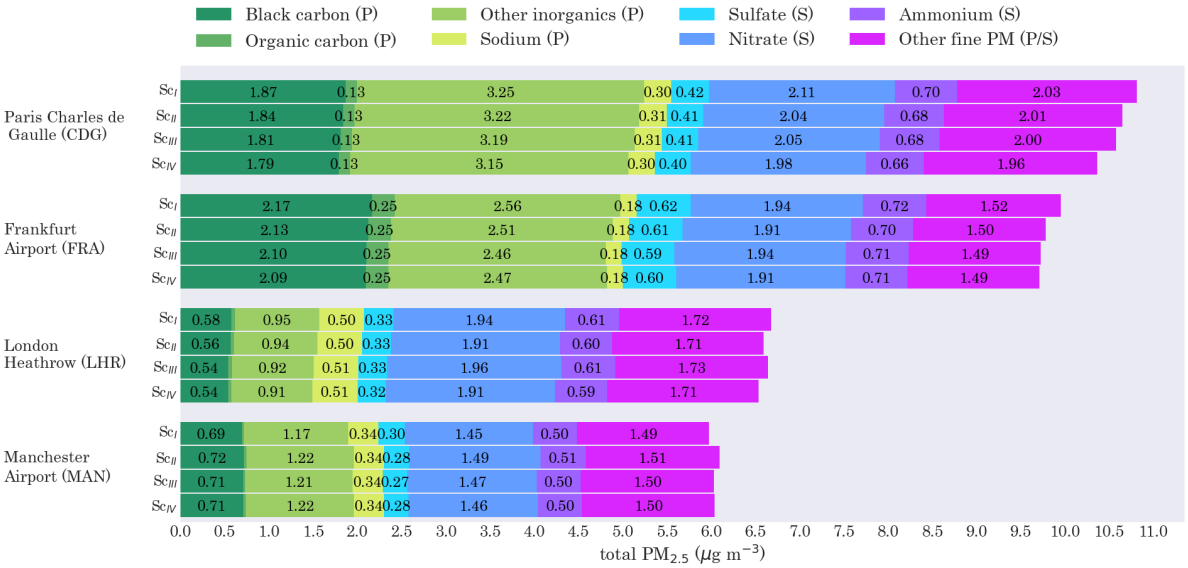

Figure 5.13. Breakdown of fine particulate matter into different compounds at four major airports: Charles de Gaulle Paris (CDG), Frankfurt Airport (FRA), London Heathrow (LHR), and Manchester Airport (MAN). The most-left bars with a green color tone are particulate matter compounds primarily of primary nature (indicated by P), while the bars with a blue color tone are primarily of secondary nature (indicated by S).

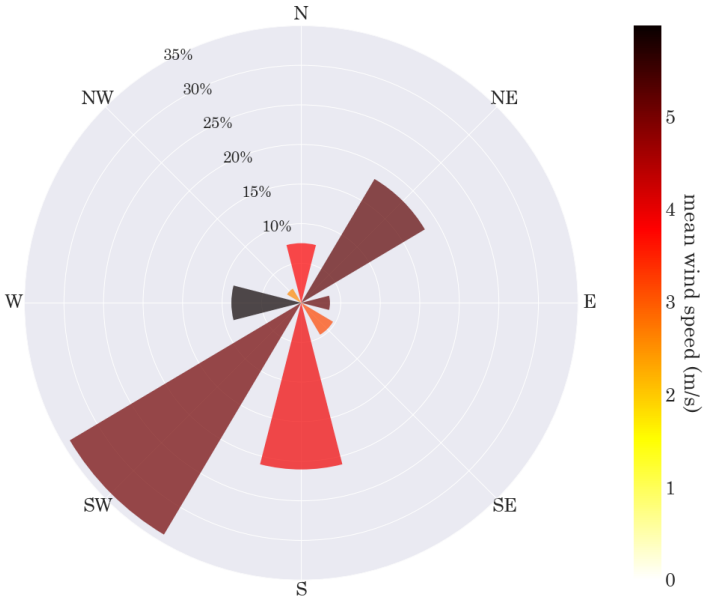

Figure 5.14. Wind rose (indicating from where the wind is originating) for scenario I at Manchester Airport. The frequency of the wind direction (as a proportion) is shown on the radial axis. Colors show the average wind speed in each direction. Wind roses for the other scenarios are highly similar and are therefore not shown.

Revisiting the general observations drawn from Figure 5.12, with two airport groupings based on changes in O_3 levels associated with changes in NO_2 levels, leads to Figure 5.15 which shows the ratio of background volatile organic compound (VOC) concentration to the background NO_x ($NO + NO_2$) concentration. The list of VOCs that are included here has been discussed in Section 4.6. The locations of the ten airports from Figure 5.12 (their associated grid cell center) are shown as well. Around Amsterdam Schiphol Airport the relative VOC abundance is smallest with a VOC/NO_x ratio around 1.1, while Milan Malpensa resides at the other side of the spectrum with a VOC/NO_x ratio around 3. The link between the VOC/NO_x ratio and the results from Figure 5.12 becomes clearer in Figure 5.16, which shows the VOC/NO_x ratio at individual airports versus the difference in O_3 concentrations between different scenarios, i.e. three data points for each airport. Figure 5.16 shows that for the relatively high

Sc_I: baseline (2019 emissions), Sc_{II}: H_2 fuel cells & jet fuel combustion, Sc_{III}: H_2 fuel cells & H_2 combustion, Sc_{IV}: H_2 fuel cells

(low) VOC/NO_x ratios above (below) ~ 2, O_3 decreases (increases) with a decrease in NO_2 concentrations. The single red data point in Figure 5.16 corresponds to Manchester Airport, scenario II versus scenario I, where O_3 decreases upon an increase in NO_2 concentration as Manchester lies within the so-called VOC-limited regime. The obtained results are highly consistent with theory. For the included VOCs, the boundary between the VOC-limited and NO_x-limited regime lies somewhere in the hatched portion of the graph, between a VOC/NO_x ratio of 2 and 2.15. The interplay between background VOC and NO_x concentrations explains the distinctive translation of individual airports towards higher/lower O_3 concentrations in Figure 5.12.

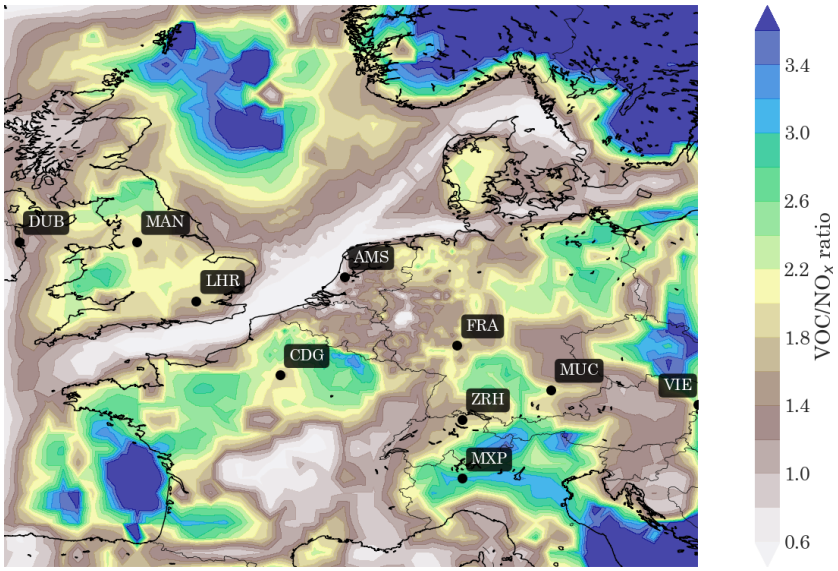

Figure 5.15. Ratio between a list of volatile organic compounds (VOCs) and nitrogen oxides (NO_x) background concentrations, regridded onto a uniform grid with the highest spatial resolution from d04. Values shown are two-weekly mean values for scenario I. The maps for scenarios II, III, and IV are highly similar.

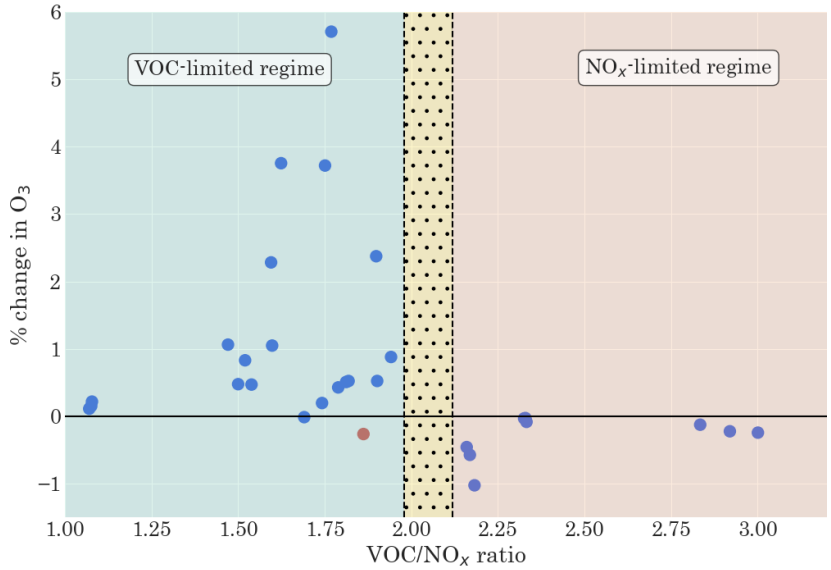

Figure 5.16. Ratio between a list of volatile organic compounds (VOCs) and nitrogen oxides (NO_x) background concentrations versus the change in O_3 concentrations between scenarios. Individual points represent the ten major airport locations in combination with a scenario paired with the baseline (scenario I), i.e. $10 \times 3 = 30$ data points. The change in background nitrogen dioxide is given to the color aesthetic, where red (blue) indicates an increase (decrease) in NO_2. The VOC-limited regime is indicated by a mediumaquamarine background, the NO_x-limited regime by a sandybrown background. The hatched area in between indicates the uncertainty range in the boundary between the two regimes.

5.2.2. Radius of Airport Pollution

Local air quality changes in the vicinity of three largest Dutch airports - Eindhoven, Rotterdam-The Hague, and Amsterdam Schiphol Airport - are shown in Figures 5.17 and F.1. At all three airports, air quality improvements regarding NO_2 clearly peak right at the airport, declining when moving further away from the airport until the curves level off, theoretically to a mean background difference. At all three airports, O_3 levels are shown to be elevated, likely caused by local reductions in NO_2 concentrations in an area residing in the VOC-limited regime. The O_3 difference compared to the baseline rapidly becomes negative when moving away from the airports, which can be seen most clearly for Eindhoven en Rotterdam-The Hague Airport in Figures 5.17d, 5.17e, and 5.17f. In the case of Eindhoven this transition happens between 0.8 and 2.9 km from the airport - depending on the scenario - and between 5.9 and 14 km in the case of Rotterdam-The Hague. In the case of Amsterdam Schiphol the airport signature is much less clear and background concentrations are less apparent from the data presented. This could be partly due to the airport size with runways spread over a wider area, whereby associated emissions are spread out over a larger area. Additionally, some potential modeling errors[4] point to the case of Amsterdam Schiphol. Henceforth, only the cases of Eindhoven and Rotterdam-The Hague Airport will be addressed. The plots for Amsterdam Schiphol are included in Appendix F.

NO_2 gives the clearest signal as it is relatively short-lived, meaning elevated concentrations remain closer to the original emission source. Based on Figure 5.17, the radius of airport pollution (RAP) at Eindhoven Airport is visually estimated around 8 km, with the $PM_{2.5}$ signal being less clear but also plausibly complying with a similar RAP. For Rotterdam-The Hague Airport, the visual estimate of the RAP is 13 km. The larger aviation fuel consumption associated with Eindhoven Airport (+92% compared to Rotterdam-The Hague Airport) is reflected in the absolute NO_2 differences at the airport being larger at Eindhoven Airport, but as differences in NO_2 concentrations decline much faster around Eindhoven than around Rotterdam-The Hague Airport, the RAP is generally lower for Eindhoven Airport. Predominant wind directions are similar, yet mean wind speed is found larger at Rotterdam-The Hague Airport than at Eindhoven Airport during the simulation time (3.40 m/s versus 3.25 m/s with negligible differences in variability), possibly explaining the larger RAP found at Rotterdam-The Hague. It is also observed that the NO_2 reductions (and O_3 increases) in scenario III are smaller than in scenario II, despite lower air pollution from aviation in scenario III. It is found that within a 15 km radius from Rotterdam-The Hague Airport, the mean short-wave radiation flux - used as proxy for the photolysis rate converting NO_2 back to NO - is significantly lower in scenario III than in the other scenarios (roughly -1.4% compared to the baseline scenario). Hence NO_2 is depleted at a slower rate in scenario III and this effect may be larger than the aviation emission cut in scenario III compared to scenario II.

The Quantile-Quantile plots for all data contained within the original boundaries defining d04 are shown in Appendix G for the normalized differences in time mean NO_2, O_3, and $PM_{2.5}$ concentrations. The Shapiro-Wilk test and the D'Agostino's K^2 test, with the null hypothesis of the distributions being normal, show that in all cases except O_3 changes between scenarios II and I ($p = 0.052$) the null hypothesis should be rejected using a 0.05 significance level. Yet, based on Figure G.1 all data distributions are said to be close to Gaussian. The mean concentration difference at locations at a fixed distance from each airport (line graphs in Figures 5.17 and F.1) are converted to a Z-score and subsequently to p-values assuming a Gaussian distribution, as explained in Section 4.6.6. The results are shown in Table 5.6. Even though the RAP values reported in Table 5.6 are clearly lower than the ones reported previously based on visual inspection, this method shows once again that the RAP is lower for Eindhoven than for Rotterdam-The Hague Airport. Nonetheless the visual inspection method is preferred as the latter approach involves parametric assumptions and an arbitrary definition of the significance level, as well as a domain-wide approximation of background levels which may not correspond with local background levels.

[4] Modeled changes in air quality around Amsterdam Schiphol resulted much lower than at other large airports within the study domain. This is possibly due to a mismatch between the number of emission input files grid lines (in west-east direction) and the number of grid lines defined in the namelist settings (see Appendix A). Due to server problems this could not be further verified.

Table 5.6. Radius of airport pollution (km) per airport, per compound and per scenario, based on significant deviations from the mean difference.

Airport	Compound	Sc_{II} - Sc_I	Sc_{III} - Sc_I	Sc_{IV} - Sc_I
Eindhoven	NO_2	3.6	7.3	6.2
	O_3	0.0	2.1	2.6
	$PM_{2.5}$	0.0	0.0	0.0
Rotterdam-The Hague	NO_2	6.2	5.4	7.6
	O_3	7.8	5.8	6.6
	$PM_{2.5}$	7.2	0.0	0.0

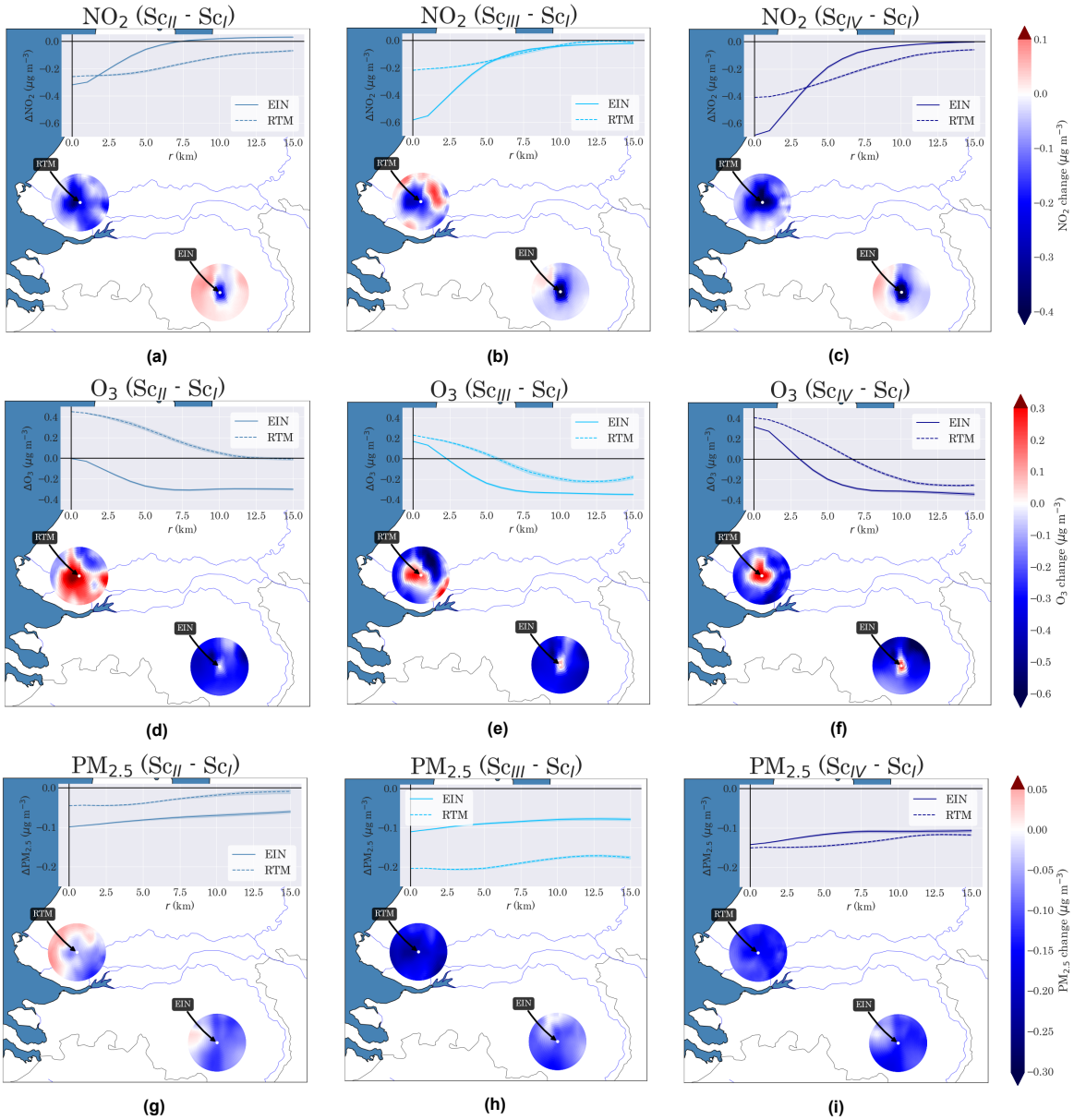

Figure 5.17. Time mean changes in air quality around Eindhoven Airport (EIN) and Rotterdam-The Hague Airport (RTM), the Netherlands, between the H_2 scenarios and the baseline scenario. Differences in concentration are plotted starting at the airport, moving 15 km away from the airport. Contour plots show absolute differences in concentration, the line plots show the absolute differences as a function of distance from the airport (the mean at each distance) with a 95% confidence interval band of the mean. Plots **(a)**, **(b)**, and **(c)** show changes in NO_2 concentrations, plots **(d)**, **(e)**, and **(f)** show changes in O_3 concentrations and plots **(g)**, **(h)**, and **(i)** show changes in $PM_{2.5}$ concentrations.

6

Modeling Evaluation

This chapter reviews the research modeling process and validates the two main models used - the AEM (Section 6.1) and the WRF-Chem model (Section 6.2) - along with an assessment of how the simulation period affects some of the obtained results from Chapter 5 (Section 6.3).

6.1. Validation AEM Output

To validate the aviation emissions output from the Advanced Emission Model described in Section 4.2, the burned fuel and specific compound emissions are compared with provided output of the FLights and Emission Model (FLEM) aircraft emission model, maintained by the Dutch Civil Aviation Department [Pulles et al., 1995]. The FLEM output data contain flight emissions (in kilograms) for three different aircraft: the Boeing 747-400, the Boeing 767-300, and the Airbus 310-200. The emissions on three different flight distances, each carrying the same payload, are reported, which are 3,000, 6,000, and 9,000 km for the B747, 3,000, 5,000, and 7,000 km for the B767 and 2,000, 3,000, and 4,000 km for the A310. The effect of payload is disregarded in AEM. The reported fuel consumed over the entire flight and the emitted NO_x mass are shown in Figures 6.1a and 6.1b, respectively.

A total of 223, 294, and 27 flights operated with the B747-400, the B767-300, and the A310, respectively, are encountered in the air traffic data sets used in this study, and the burned fuel and NO_x emissions as estimated by AEM have been plotted in Figures 6.1a and 6.1b as a function of flown distance. Trend lines shown are based on the method of least-squares regression. As the exact flight path varies for each flight, there is some variability seen with respect to the trend lines, but overall the emitted fuel (and NO_x) scales linearly with distance flown. The data points obtained from FLEM are within the observed range for all three aircraft types, and show a high degree of conformity between both models, especially relating to the total amount of burned fuel. NO_x emissions also show large correspondence between models for the A310, but AEM estimates roughly 35% higher NO_x emissions for the Boeing aircraft types. Carbon monoxide estimates - shown in Figure H.2a of Appendix H - are a factor 2-3 lower in AEM than in FLEM. Differences in CO and NO_x estimates can arise under different parametrization schemes, as the emission of both compounds rely on complex thermodynamics. E.g. for CO_2 and H_2O, which are not incorporated in this study, the correspondence between both models is as good as for the total fuel emitted (see Figure H.1) as those quantities are related by a fixed emission factor - 1.237 kg/kg fuel for H_2O and 3.155 kg/kg fuel for CO_2. For sulfuric oxides however, it is observed that AEM estimates a factor 4 higher emissions than FLEM, see Figure H.2b. This is most probably related to underlying modeling assumptions about the sulfuric content of the fuel used by the three aircraft types.

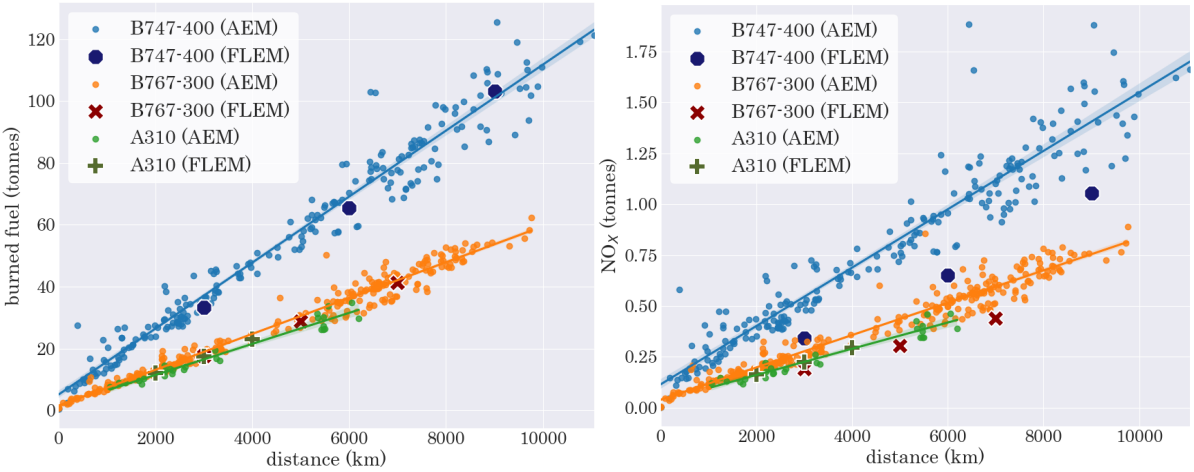

Figure 6.1. Modeled fuel burned **(a)** and NO_x emitted **(b)** as a function of distance flown for three aircraft types - B747-400, B767-300, and A310(-200) - shown as small dots. The AEM output is compared with FLEM output (large dots). Least squares regression lines with a 95% confidence interval of the mean are shown for each aircraft type.

Segmenting flights based on the flight phases shown in Figure 4.5 gives a better idea of where the model discrepancies arise. Figure 6.2 shows this for the landing and take-off (LTO) phase, which includes the taxi, take-off, climb out, landing, and approach phases from Figure 4.5. Differences in the traversed distance within the LTO phase between individual flights are small enough to disregard. In Figure 6.2, the AEM output is compared with the same reference flights from FLEM. Additionally, the AEM output can be compared with measurements on fuel consumption or emissions per LTO cycle and per aircraft type from EEA [2019], as measuring emissions during the LTO cycle is a mandatory part of each engine certification process. Whereas total in-flight emitted NO_x mass estimates from AEM are higher than for FLEM, the mean NO_x mass emitted during the LTO phase obtained from AEM is even less than for the reference points (-5% and -1% for the B747-400, -21% and -25% for the B767-300, and -36% and -49% for the A310, compared to EMEP/EEA and FLEM, respectively). Higher estimates from AEM primarily arise during the climb and cruise phase. As the model estimates from AEM are not consistently higher during all flight phases and the orders of magnitude correspond, it is assumed that observed model discrepancies arise due to 1) the limited amount of data to compare the AEM output with, 2) different model parametrizations.

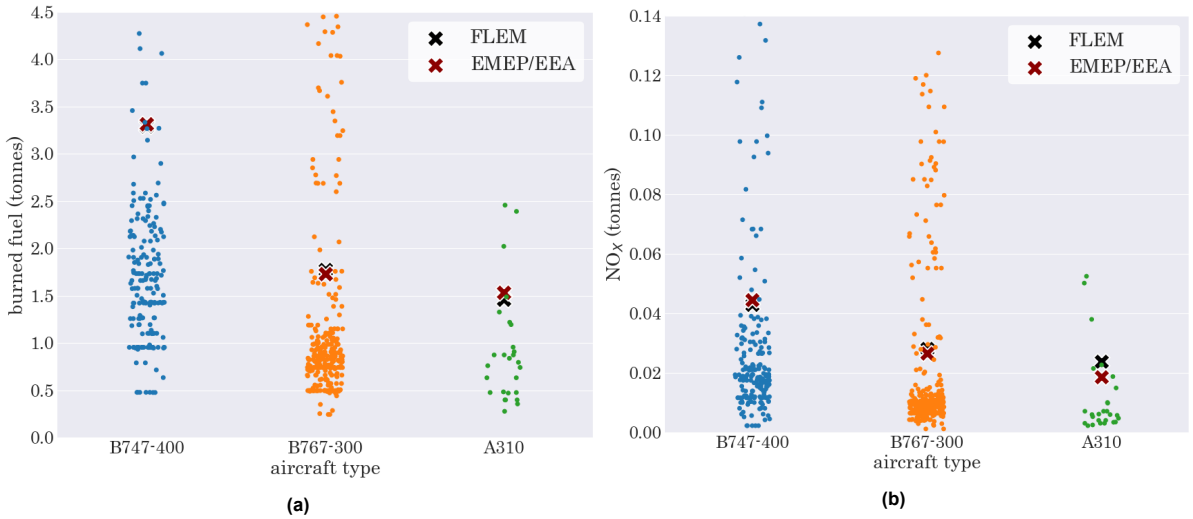

Figure 6.2. Modeled fuel burned **(a)** and emitted NO_x **(b)** for the same three aircraft types during the landing and take-off (LTO) phase. The AEM output (small dots) is compared with FLEM and EMEP/EEA data (large dots). Each individual flight from the AEM output is again represented by a blue, orange or green dot.

For carbon monoxide, AEM outputs lower emissions than FLEM and EMEP/EEA report during all three flight phases where low thrust settings cause a large relative contribution to total CO emissions - taxi-in/out, cruise, and descent. For the B747-400 and the B767-300, Figure H.3a shows that differences between FLEM and EMEP in LTO cycle CO emissions are also large. This illustrates the difficulty in estimating CO emissions, a product depending on incomplete fuel combustion. Due to the large share of CO emissions during taxiing, unreliable taxi time estimates go hand in hand with unreliable total CO emission estimates.

SO_x emissions are estimated higher with AEM during all flight phases (except during the LTO phase for the B747-400 and the B767-300, see Figure H.3b). Much depends on the underlying modeling assumptions regarding the fuel composition - in this case the sulfuric content of the fuel. The legally enforced limit on fuel sulfuric content is set at 3000 parts per million volume (0.3% by weight), but highly varies in practise depending on national legislation [Kapadia et al., 2016]. For AEM, the fuel sulfuric content is assumed to be 0.085% by weight [EUROCONTROL, 2021a]. Related model estimates may produce high biases of a couple of orders magnitude. From Figure 4.10 it was seen that fuel consumption, outputted by AEM, scales linearly with SO_x emissions. The model parameters, including the engine types that are coupled to the discussed aircraft types, should be assessed more accurately for all sources to pinpoint the cause(s) of observed discrepancies.

6.2. Validation WRF-Chem Model Output

The modeled concentrations have been compared with observations to assess their uncertainty, which is relevant in light of the modeling results presented in Chapter 5. Therefore this section compares the model output of the baseline scenario (scenario I) - being the 2019 emission case - to measurement data. The compounds by which air quality is assessed - NO_2, O_3, and $PM_{2.5}$ - are in this way validated. In addition, the wind velocity and direction as derived from the horizontal wind components outputted by WRF-Chem are validated, as Chapter 5 showed that spatial variations in air quality are to a large extent influenced by those variables through transport.

In Section 4.7 the statistical validation tools were presented. Section 6.2.1 presents the model performance assessed by validated hourly measurements from the RIVM and the Dienst Centraal Milieubeheer Rijnmond (DCMR) on NO_2, O_3, $PM_{2.5}$, wind speed, and wind direction at 23 rural background sites within the Netherlands [RIVM, DCMR and others, 2021]. Only rural background sites are used for the model validation because local sources of pollution, e.g. near factories or highways, are not well-resolved on the modeled (or interpolated) resolution of $\sim 1.3 \times 2.1$ km. Therefore, concentrations measured at those sites could be higher than the modeled concentrations by virtue of the measurement location. Section 6.2.2 compares the model output with data from the AirBase database on the rest of the study domain[1] [EEA, 2021a]. The used data product does not include meteorological variables and no fine particulate matter, so the evaluation is limited to NO_2 and O_3 in this case.

6.2.1. Model Performance Inner Domains

A major part of this study focused on the inner domains, d03 and d04. Local air quality around airports (Section 5.2.2) and the comparison of local NO_2 levels with WHO guideline levels are completely based on those domains as the spatial resolution on those domains allowed for this. RIVM, DCMR and others [2021] provide hourly measurements, both for the air quality indicators discussed in this study as for meteorological variables, at the 23 rural background stations shown in Figure 6.3. All stations are listed in Table I.1, which shows the variables that are measured at the station. NO_2 concentrations, wind speed, and wind direction are measured at all sites. O_3 and $PM_{2.5}$ concentrations are measured at 16 and 9 locations, respectively. The time series, both from the WRF-Chem simulations and from measurements, at those sites are shown in Appendix I.

[1] Data within the Netherlands is excluded as this is already analyzed in Section 6.2.1.

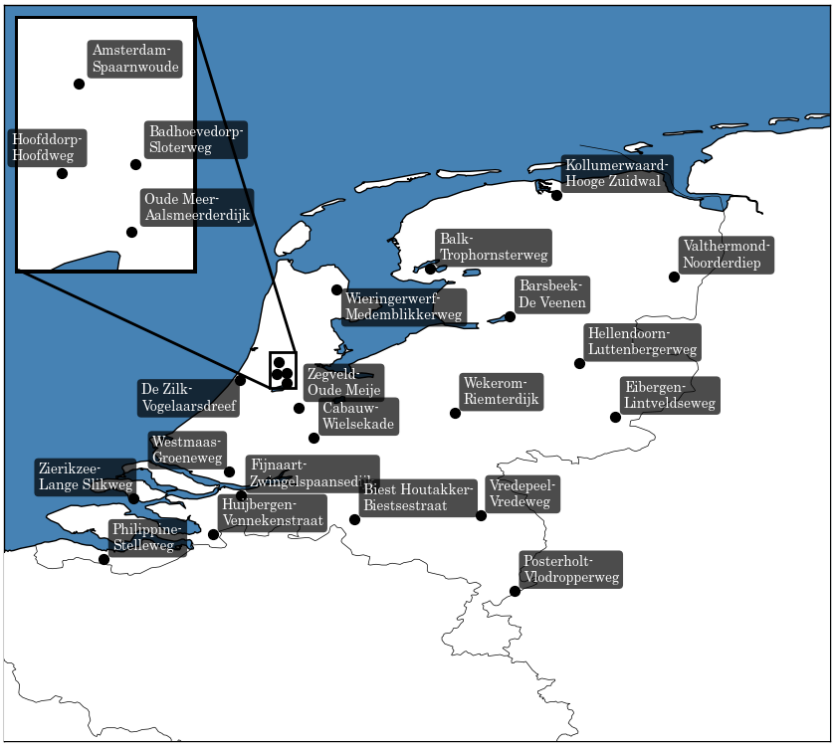

Figure 6.3. Rural background measurement sites from the RIVM/DCMR database [RIVM, DCMR and others, 2021].

Table 6.1 shows the outcome of the validation procedure for NO_2, O_3, $PM_{2.5}$, wind direction, and wind speed. R and IOA are shown side-by-side to indicate that both metrics indicate a similar ranking of variables based on model performance, except O_3 which has a higher correlation coefficient than the wind direction but a lower IOA. As mentioned before, the disadvantage of R is that a systematic (e.g. additive) bias between model-simulated values and observations is not captured, while IOA incorporates this by taking the absolute differences into account. Clear from Table 6.1 is that the wind speed is modeled adequately while the modeling of $PM_{2.5}$ concentrations fall short compared to other variables. The good correspondence of the wind speed it not surprising as the wind is nudged (outside the PBL) during the WRF-Chem simulations. Looking at individual locations however, the lowest correlation and agreement are found for NO_2 at Oude Meer and Huijbergen, as can be seen in the bar plots in Figure 6.4. The low model correspondence with measurements at Oude Meer is conspicuous, as this site is located near Schiphol Airport where the suspicion was raised that WRF-Chem is underestimating air pollutant concentrations. This systematic underestimation can be seen in the time series in Figure I.1, and in Figure 6.5b which shows the normalized mean bias error (NMBE) on the horizontal axis. Similar underestimation of NO_2 concentrations are found at Badhoevedorp - another site in the direct vicinity of Schiphol Airport - see Figures I.1 and 6.5b. Unfortunately the sites at Oude Meer and Badhoevedorp do not measure ozone (see Table I.1). $PM_{2.5}$ is measured at Badhoevedorp and has the lowest correlation and agreement of all sites measuring $PM_{2.5}$ ($R = 0.22$, IOA = 0.44), which can be attributed to large differences in variability (RMSE = 9.1 μg m^{-3}, MBE = -0.5 μg m^{-3}). Together with Spaarnwoude, Badhoevedorp is the only site where the MBE is negative (i.e. the model systematically underestimates $PM_{2.5}$ concentrations at those sites). Spaarnwoude and Badhoevedorp are the only sites near Amsterdam where $PM_{2.5}$ is measured.

Table 6.1. The validation of five modeled variables, measured at a total of 23 Dutch stations. The observed mean quantity at those locations, Pearson's correlation coefficient (R), Willmott's Index of Agreement (IOA), mean bias error (MBE), centered root mean squared error (CRMSE) and root mean squared error (RMSE) are shown along with the minimum and maximum values between square brackets.

Variable	Mean obs.[2]	R [-]	IOA [-]	MBE[2]	CRMSE[2]	RMSE[2]
NO_2 [μg m^{-3}]	11.4 [6.5-21.0]	0.47 [0.15-0.63]	0.63 [0.39-0.78]	-2.9 [-11.6-0.9]	7.5 [3.4-12.9]	8.3 [4.48-16.5]
O_3 [μg m^{-3}]	60.8 [55.8-67.7]	0.58 [0.44-0.69]	0.73 [0.63-0.83]	7.7 [0.1-15.8]	20.4 [16.2-27.2]	22.0 [16.2-29.7]
$PM_{2.5}$ [μg m^{-3}]	7.2 [4.9-9.9]	0.39 [0.22-0.56]	0.57 [0.44-0.71]	2.0 [-1.2-4.8]	6.5 [5.3-9.1]	7.0 [6.1-9.1]
Wind dir [°]	190 [172-203]	0.54 [0.19-0.73]	0.76 [0.57-0.86]	-1.3 [-10.5-9.4]	81.1 [64.9-107.1]	81.2 [64.9-107.0]
Wind speed [m/s]	4.3 [2.9-6.2]	0.84 [0.74-0.90]	0.88 [0.78-0.93]	-0.2 [-1.5-1.1]	1.4 [1.2-1.8]	1.5 [1.2-2.4]

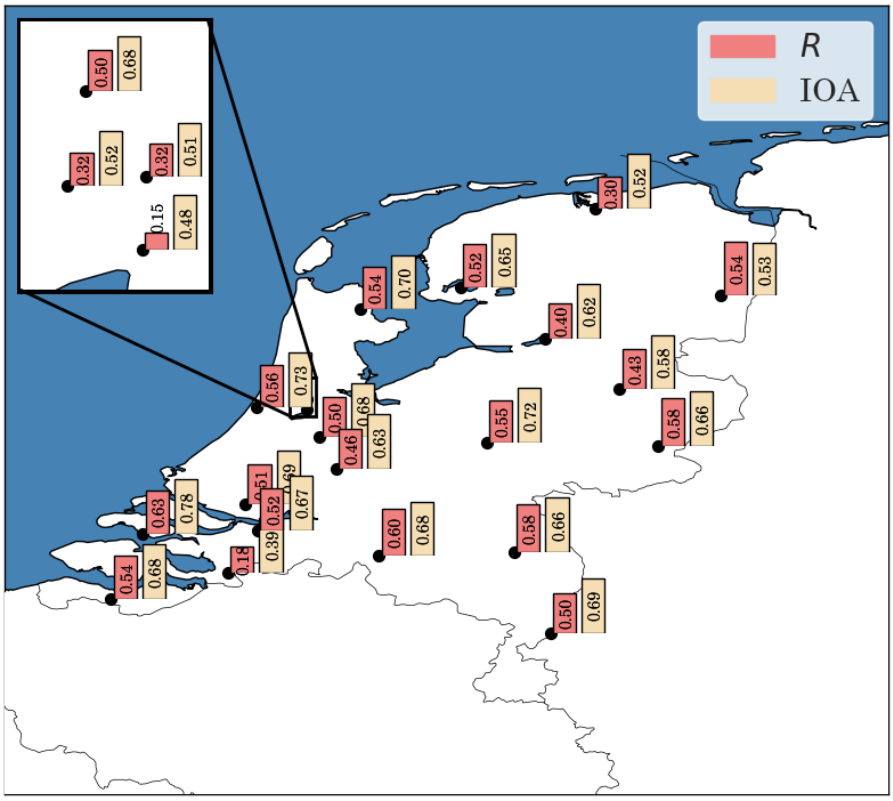

Figure 6.4. Pearson's correlation coefficient (R) and Willmott's Index of Agreement (IOA) between model-simulated and measured NO_2 concentrations at each measuring site.

From a comparison of the MBE and CRMSE columns in Table 6.1 it can be said that a major part of the modeling error is due to temporal variability in the measured data that is not well resolved in WRF-Chem. Figure I.1 shows for example that WRF-Chem underestimates the magnitude of local peaks in NO_2 concentrations in most occasions. Measures as the RMSE penalize those occurrences even more as those metrics rely on squaring the differences between the modeled and the observed data. However, in terms of model bias the model performs reasonably well, which can be deduced more clearly from Figure 6.5b. The NMBE shown in Figure 6.5b puts the reported MBE values in perspective of the overall magnitudes by dividing the MBE by the mean of the observed values (see Equation 4.11). The mean NMBE for each variable is indicated by the diamond-shaped icons in Figure 6.5b. There is hardly any model bias present in the wind speed and direction (mean NMBE = -0.7% and -1.7%, respectively). The mean NMBE for the NO_2, O_3, and $PM_{2.5}$ are -24.8%, 12.9%, and 35.2%, respectively. The NMBE values regarding wind direction at each site are clustered around zero, while there is more spread in the NMBE values regarding wind speed. At 19 out of 23 sites, the NO_2 bias is negative, meaning WRF-Chem systematically underestimates NO_2 concentrations at most locations. $PM_{2.5}$ concentrations are generally overestimated by WRF-Chem, except near Amsterdam (Badhoevedorp

[2]Shown in units of variable.

and Spaarnwoude). Finally, mean O_3 concentrations are overestimated by WRF-Chem at all 16 sites where O_3 is being measured - possible relating to the negative NO_2 bias and the found anti-correlation between NO_2 and O_3 concentrations in NO_x-limited areas. NO_2 and $PM_{2.5}$ concentrations at Huijbergen and Badhoevedorp respectively stand out due to their negligible bias yet high NRMSE. This is caused by a high CRMSE (NCRMSE) at both locations, attributable to overestimations of the temporal variability by WRF-Chem as can be seen from Figures I.1 and I.3, and an unresolved, strong $PM_{2.5}$ elevation in the measurement data on the 9th of June at Badhoevedorp.

Figure 6.5a shows the modified Taylor diagram where all sites and compounds are included. Together with Figure 6.5b it shows the model performance spatially (i.e. at all measurement sites), with most apparent sites labeled in the two figures. The ratio of standard deviations (σ-ratio) indicates whether the temporal variance of the considered quantity is overestimated by the model ($\sigma_M/\sigma_O > 1$) or underestimated ($\sigma_M/\sigma_O < 1$). The mean ratio is near 1 for NO_2 and the wind direction, even though the (spatial) spread is much larger for NO_2 than for the wind direction. Therefore it is concluded that temporal variations in wind direction are modeled best, which Figure I.4 confirms. The low correlation and high σ-ratio at Huijbergen is clearly visible in Figure I.1, where WRF-Chem predicts large NO_2 elevations (in most extreme cases exceeding 50 μg m^{-3} while this is not seen back in measurements). Temporal variations in $PM_{2.5}$ concentrations are overestimated[3] and generally underestimated for O_3 concentrations. The wind speed stands out as being modeled most accurately, with R above 0.73 at each site and a consistently low NCRMSE.

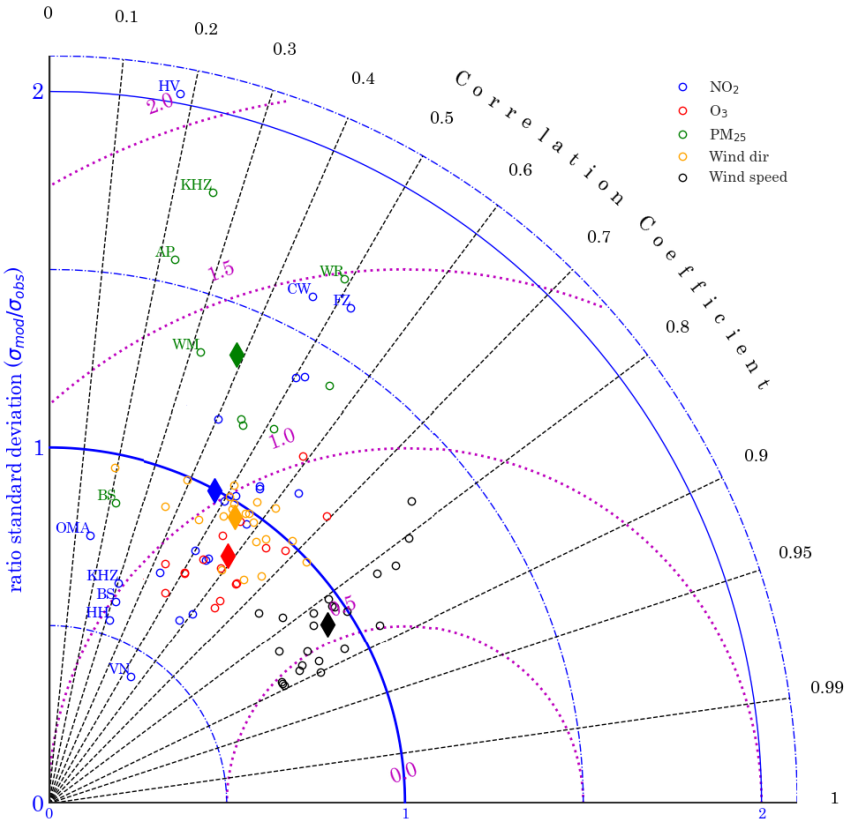

(a) The σ-ratio (σ_M/σ_O), R and normalized centered root mean squared error (NCRMSE) are shown, with (1, $\frac{\pi}{2}$) as an imaginary reference point (see also Figure 4.14).

Figure 6.5. cont'd on next page

[3]Except at Badhoevedorp, which might be the result of the aforementioned strong $PM_{2.5}$ elevation in the measurement data on the 9th of June, see Figure I.3.

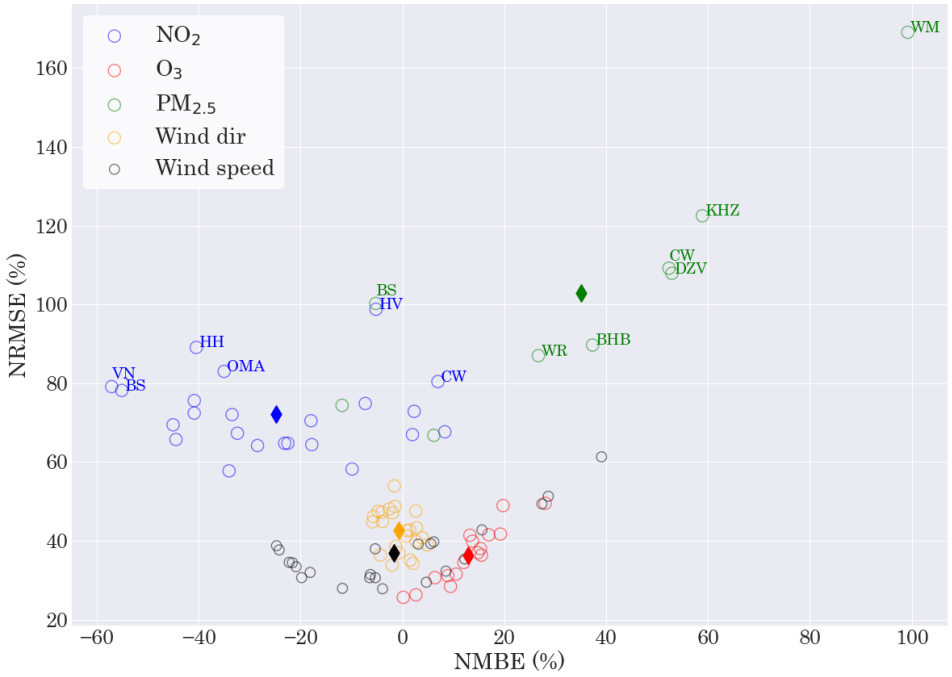

(b) Normalized mean bias error (NMBE) plotted versus normalized root mean squared error (NRMSE).

Figure 6.5. WRF-Chem model performance near 23 measurement sites in The Netherlands, shown graphically with **(a)** a modified Taylor diagram for five different variables at 23 sites and **(b)** a complementary scatter plot showing the model bias. The mean of all points belonging to one particular variable are shown in both subplots as diamond-shaped points. Individual abbreviated sites are Huijbergen (HV), Kollumerwaard (KHZ), Wekerom (WR), Cabauw (CW), Fijnaart (FZ), Wieringerwerf (WM), Badhoevedorp (BS), Oude Meer (OMA), Hoofddorp (HH), Valthermond (VN), Biest Houtakker (BHB), and De Zilk (DZV).

6.2.2. Model Performance Outer Domains

The AirBase data set provides validated measurement data of NO_2 and O_3 - amongst other compounds - on a European scale [EEA, 2021a]. All rural background measurement stations where only NO_2, only O_3 or both NO_2 and O_3 are measured are shown in Figure 6.6 - excluding the Netherlands.

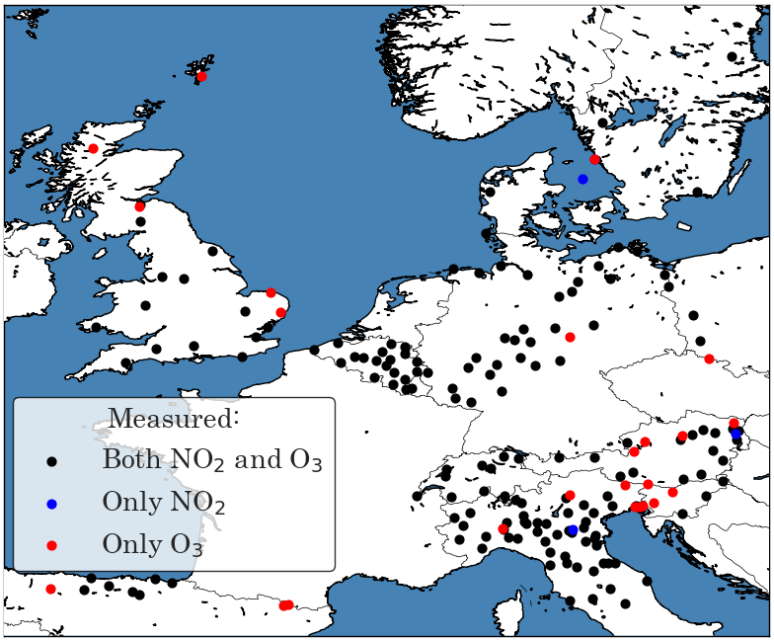

Figure 6.6. Measurement sites where out of NO_2 and O_3 only NO_2 is measured (blue), only O_3 is measured (red) or both are measured (black). The Dutch stations are not included as RIVM/DCMR data has been used to validate the model output for this region, see Section 6.2.1.

Similar to Section 6.2.1, the R, IOA, MBE, CRMSE, and RMSE metric scores are presented, see Table 6.2. Because of the high degree of skewness in the distribution of those metrics the median, first, and third quartile are reported instead of the mean, minimum, and maximum. The individual scores at each location are shown in the modified Taylor diagram in Figure 6.7a and show the high degree of spread, especially for NO_2 for which Pearson's correlation coefficient is even negative at 18 measurement sites. Those occurrences are considered acceptable looking at their relative quantity, given the number of measurement sites at which the model output is assessed. Looking at Table 6.2, conclusions are similar compared to Section 6.2.1. The model output for O_3 concentrations show a higher degree of correlation and agreement with observations compared to NO_2 concentrations, whereas the model is slightly biased towards lower NO_2 concentrations and higher O_3 concentrations.

Table 6.2. The validation of NO_2 and O_3 over the rest of the domain (outside the Netherlands). The median of the observed quantity at the measurement sites, Pearson's correlation coefficient (R), Willmott's Index of Agreement (IOA), mean bias error (MBE), centered root mean squared error (CRMSE), and root mean squared error (RMSE) are shown along with the inter-quartile range (IQR).

Variable	Mean obs.[4]	R [-]	IOA [-]	MBE[4]	CRMSE[4]	RMSE[4]
NO_2 [μg m^{-3}]	5.3 [3.4-7.8]	0.36 [0.18-0.52]	0.53 [0.37-0.65]	-0.2 [-2.0-1.8]	4.3 [3.5-5.4]	5.2 [3.9-6.2]
O_3 [μg m^{-3}]	78.0 [67.3-85.3]	0.56 [0.41-0.67]	0.66 [0.56-0.72]	0.4 [-9.5-6.7]	20.6 [17.0-24.6]	23.4 [19.7-28.2]

The MBE (and NMBE) for O_3 is however much lower in magnitude than in the inner study domains, with a mean NMBE of 0.7% (median is 0.6%). For NO_2 the mean NMBE is 26.7%, but as the median NMBE of -3.9% reflects, the mean NMBE is largely influenced by outliers caused by low observed mean NO_2 concentrations, mostly below 3 μg m^{-3} (lowest quartile, see the sites indicated in the subplot of Figure 6.7b). Similar to Section 6.2.1, the RMSE values found are largely attributable to the CRMSE.

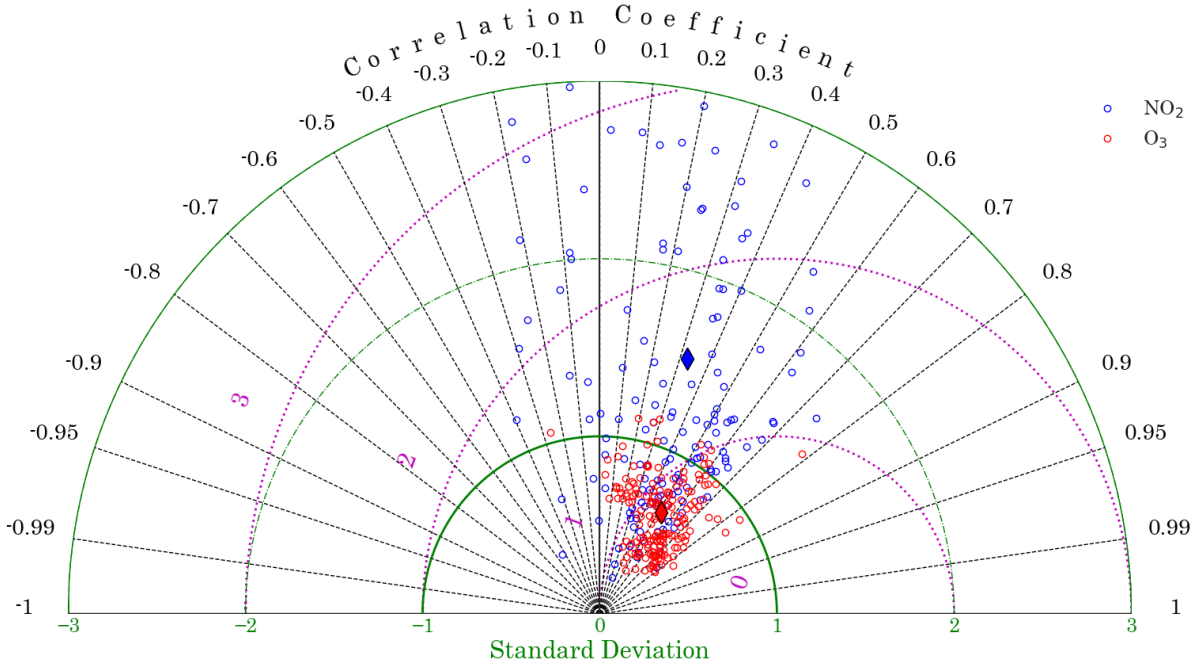

(a) The σ-ratio (σ_M/σ_O), R, and normalized centered root mean squared error (NCRMSE) are shown, with (1, $\frac{\pi}{2}$) as an imaginary reference point. For visualization purposes the σ-ratio axis is truncated at a value of 3, thereby excluding 11 data points (all NO_2) where the σ-ratio exceeds 3.

Figure 6.7. cont'd on next page

[4]Shown in units of variable.

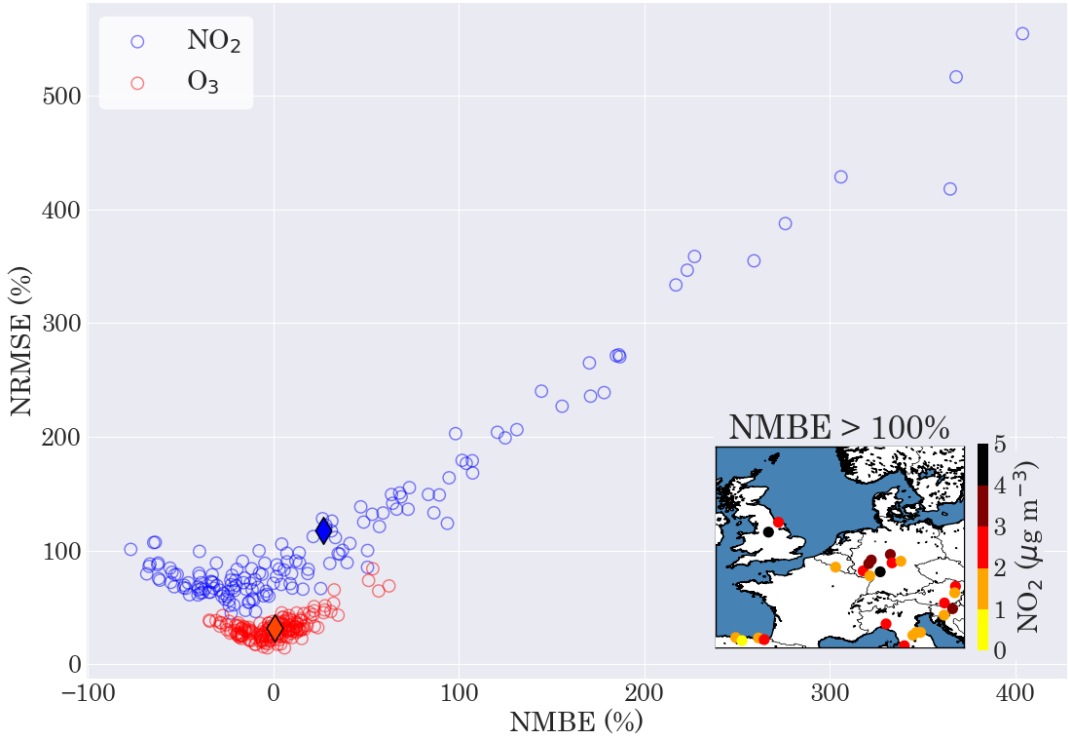

(b) Normalized mean bias error (NMBE) plotted versus normalized root mean squared error (NRMSE). The sites where the MBE is larger than the mean of the observations are shown in the inset.

Figure 6.7. WRF-Chem model performance in terms of NO_2 and O_3 concentrations near 205 measurement sites in the study domain (excluding the Netherlands), shown graphically with **(a)** a modified Taylor diagram and **(b)** a complementary scatter plot showing the model bias. The mean of all points belonging to one particular compound are shown in both subplots as diamond-shaped points.

6.3. Simulation Time-Related Error

This section puts the comparison of modeled air quality with WHO guideline levels into a broader perspective by analyzing the intra-annual variability of air quality over the study domain. As the annual WHO air quality guideline concentrations were considered, and the maximum number of allowances of surpassing the daily mean guideline (for NO_2 and $PM_{2.5}$) or maximum daily 8-hour mean guideline (for O_3) are based on a yearly time scale, the simulated time period is crucial.

The monthly mean NO_2 and O_3 concentrations are calculated at all rural background sites from the AirBase measurement data sets within the study domain (~200 locations), for which the spatial distribution is shown in Figure 6.6 (only now, Dutch stations have been included). The results of this analysis are shown in Figures 6.8 and 6.9. As the rural background sites are sampled, with a non-uniform spatial distribution over the study domain, the mean concentrations presented are merely indicative, and the emphasis is put on the observed intra-annual variability which should be representative for the entire study domain. Clearly, NO_2 concentrations during the simulated period are relatively low compared to winter months which is partly due to higher anthropogenic emissions during winter and higher photochemical conversion rates during summer [Cichowicz et al., 2017]. O_3 levels are higher during summer than during winter, primarily caused by longer days with high insolation during summer and related chemical interconversions with NO_2 by which O_3 is produced [Cichowicz et al., 2017; Roberts–Semple et al., 2012]. The simulated month of June is an extreme case in the sense that, for NO_2, the frequency of WHO guideline concentration exceedances (daily mean of 25 μg m^{-3}) was one of the lowest, while the frequency of the daily maximum 8-hour mean O_3 guideline exceedance (100 μg m^{-3}) was highest in June.

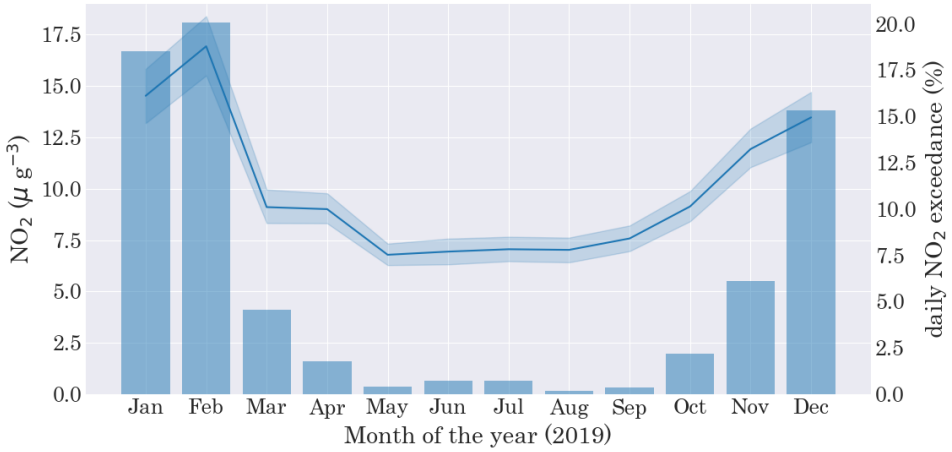

Figure 6.8. Monthly mean NO_2 concentrations based on ~200 measurement within the study domain. The band shows the 95% confidence interval of the mean. The bars show the percentage of locations and days the 25 μg m^{-3} daily mean NO_2 concentration is exceeded, considering the measurement sites located within the Netherlands (roughly d03 and d04).

Exceedance of the daily mean WHO guideline concentration for NO_2 is only considered within the Netherlands, as the original modeling resolution over the rest of the study domain is too low to make a fair comparison with measurement data. During the simulation time, the daily mean WHO guideline concentration for NO_2 is exceeded at three out of 23 rural background sites within the Netherlands. Those locations are Badhoevedorp (four exceedances), Hoofddorp (one exceedance) and Oude Meer (one exceedance), all in the vicinity of Amsterdam Schiphol Airport. The modeled daily mean NO_2 concentrations at those measurement sites do nowhere exceed 25 μg m^{-3}, again pointing to a negative model bias in the vicinity of Amsterdam (Schiphol).

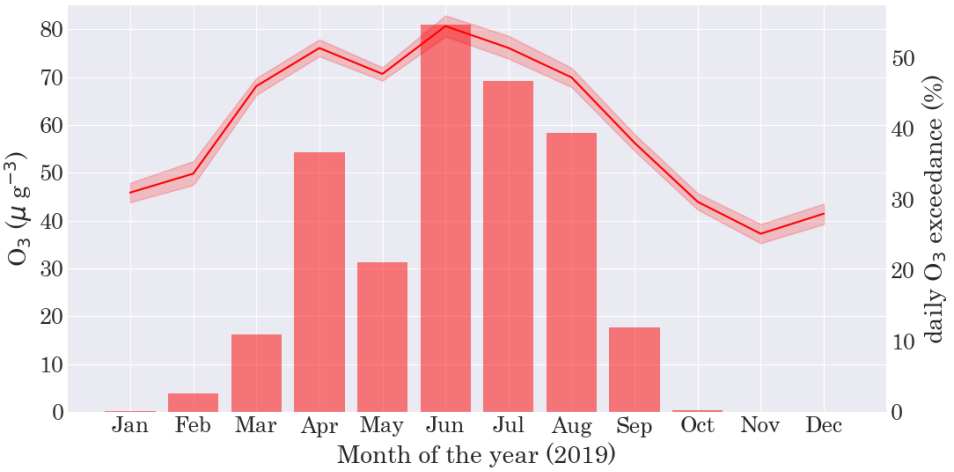

Figure 6.9. Monthly mean O_3 concentrations based on ~200 measurement sites within the study domain. The band shows the 95% confidence interval of the mean. The bars show the percentage of locations and days the 100 μg m^{-3} maximum 8-hour mean O_3 concentration is exceeded, considering all O_3 measurement sites.

At 200 out of 205 measurement sites (98%) where O_3 is measured, the daily maximum 8-hour mean WHO guideline concentration of 100 μg m^{-3} is exceeded at least four times in 2019, surpassing the threshold of 3-4 allowed exceedances on a yearly basis. In April, 191 (93%) of the sites have already reached this threshold. Within the simulated time window, i.e. during the first two weeks of June, O_3 is measured at 201 measurement sites. Out of those, the guideline concentration is exceeded four times or more at 128 sites (64%). Analyzing modeled O_3 concentrations at the same sites, it is found that O_3 concentrations are above the WHO guideline concentration at 75 (37%) of the measurement sites for at least four days between June 1st and June 14th. In other words, WRF-Chem appears to underestimate the number of sites exceeding the daily maximum 8-hour WHO guideline concentration for O_3. This might be reflected in the underestimation of temporal O_3 variability by WRF-Chem found

in this chapter, seen by a σ-ratio below 1 (Figures 6.5a and 6.7a).

Regarding $PM_{2.5}$, the region of the Netherlands is used as $PM_{2.5}$ measurements are not available from the use European AirBase data product. To compensate for the reduced size of the data set, all sites from the RIVM/DCMR database where $PM_{2.5}$ is measured are included, i.e. not only rural background sites. This totals to 47 locations. The monthly mean concentration at those sites is shown in Figure 6.10, with the frequency per month of daily mean WHO guideline exceedance (15 μg m^{-3}) shown as a bar chart. Concentrations are highest during winter months, reaching a minimum at the start of autumn.

Over the year, at all 47 measurement sites the 15 μg m^{-3} WHO guideline concentration for daily mean $PM_{2.5}$ concentrations is exceeded at least four times (the minimum is 45 days within 2019). Measurements at all those 47 locations are available during the simulation time from June 1st up to June 14th. At Badhoevedorp the WHO guideline concentration is exceeded once (which can clearly be seen in Figure I.3) and twice at another site, but at no site the guideline is exceeded four times or more during those two weeks. This is related to the time of the year as is deduced from Figure 6.10, with June having the lowest guideline exceedance frequency after September and October. According to the WRF-Chem output at those 47 sites, the WHO guideline concentration is exceeded once at 11 (different) sites, but in concordance with observations no location exceeds the WHO guideline four times or more. Still, the simulation period does not seem to be a representative time sample on a yearly basis as intra-annual $PM_{2.5}$ fluctuations are high, and concentrations are much higher during winter than during summer.

To summarize, the yearly estimate of the number of locations exceeding the daily 8-hour mean O_3 guideline seem to be most representative simulating the first two weeks of June (despite any model biases), as the simulation period falls within the O_3 peak season. Both NO_2 and $PM_{2.5}$ concentrations were low during the simulation period compared to other periods of the year. Thereby, the number of locations exceeding daily mean guidelines on a yearly basis are vastly underestimated, as well as the number of locations exceeding the annual mean guideline concentrations. This does not undermine the purpose of this study to quantify relative air quality changes between aviation scenarios. It however shows that when simulating a different period of the year, those changes may lead to stronger (weaker) conclusions as more (less) locations reside on the edge of what is being accepted regarding air quality.

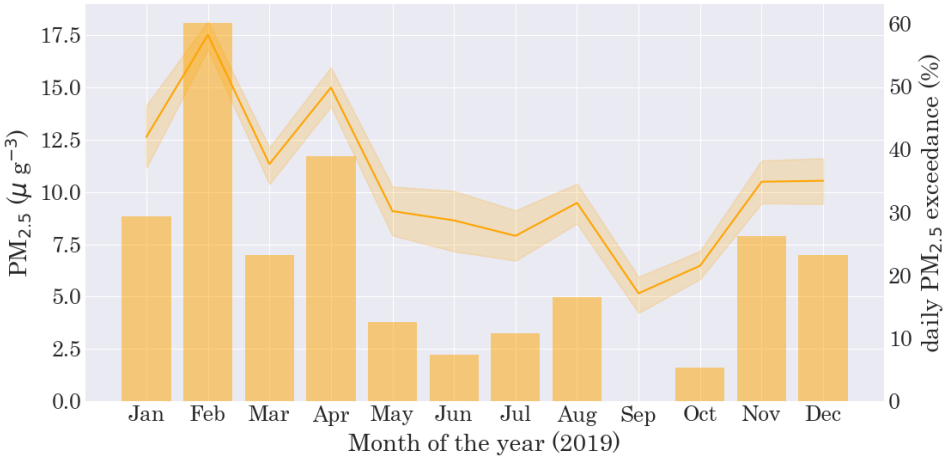

Figure 6.10. Monthly mean $PM_{2.5}$ concentrations based on 47 measurement sites within the Netherlands. The band shows the 95% confidence interval of the mean. The bars show the percentage of locations and days the 15 μg m^{-3} daily mean $PM_{2.5}$ concentration is exceeded.

7

Conclusion & Recommendations

This study aimed to quantify changes in air quality within northwestern Europe - both on a local and regional scale - by looking at different air traffic emission scenarios involving hydrogen propulsion. Domain average differences in air quality compared to the baseline scenario are small. For the first hydrogen scenario with only short-haul flights on H_2 fuel cells (scenario II), NO_2, O_3, and $PM_{2.5}$ concentrations decrease by 2.3‰, 0.6‰, and 1.9‰, respectively. For the most promising yet technically feasible hydrogen scenario (scenario III), NO_2, O_3, and $PM_{2.5}$ concentrations decrease by 3.3‰, 1.5‰, and 5.8‰, respectively. For scenario IV, which quantifies the theoretically achievable change in air quality by aviation, decreases of 5.7‰, 1.6‰, and 8.1‰ are found for NO_2, O_3, and $PM_{2.5}$, respectively. Hence, total contributions of current aviation to background NO_2, O_3, and $PM_{2.5}$ concentrations are reduced by 57%, 91%, and 72%, respectively, when short-haul flights are equipped with H_2 fuel cells and medium and long-haul flights with the H_2 combustion system (scenario III). The reductions are 40%, 34%, and 24% in the case where only short-haul flights fly on H_2 fuel cells (scenario II). A breakdown of $PM_{2.5}$ shows that mainly sulfate, nitrate, ammonium, black carbon, and other inorganics contribute to the effects of aviation on atmospheric $PM_{2.5}$ concentrations. Locally, small increases in $PM_{2.5}$ are found over the study domain, which is shown to coincide significantly with changes in wind field.

Furthermore, this study finds that aviation generally amplifies spatial differences in air quality, especially in terms of NO_2 and $PM_{2.5}$. This can be explained by the local nature of air traffic emissions - near airports - and the location of (major) airports in the vicinity of (large) cities where air pollution levels are generally higher than at rural sites. It is thereby likely that air traffic pollution contributes to degradation of air quality at locations where air quality is often already poor. For O_3, no clear effect on spatial differences in air quality is seen, as this study shows that O_3 increases in some locations and decreases in others.

In the vicinities of the ten largest airport within the study domain, NO_2 concentrations decrease when moving from scenario I (2019 aviation emissions) to scenario IV (no aviation emissions). One exception is Manchester Airport, where $PM_{2.5}$ concentrations are also higher in the hydrogen scenarios compared to the baseline scenario. This cannot be related to local chemistry but rather to small changes in the wind field (increase in wind speed and local wind convergence). In addition, Manchester Airport is one of the smallest out of the ten analyzed airports, with the smallest share of short-haul flights. Therefore the absolute change in air traffic emissions - especially for scenario II in which only short-haul flight emissions are reduced - is smallest for this airport. Hence, any effect of reduced local emissions could be more easily overshadowed by meteorological effects (like transport). This is affirmed by looking at primary and secondary aerosol concentrations, which are both lower in scenario I than in the hydrogen scenarios. The largest changes in air quality are seen around Frankfurt Airport, with a respective 18.2% and 2.3% decrease in NO_2 and $PM_{2.5}$ concentrations, and a 3.8% increase in O_3 concentrations in scenario III compared to scenario I. Relative changes in air quality around the largest airports are about two orders of magnitude larger than the changes in domain averages. O_3 concentrations decrease with lower air traffic emissions at merely three out of ten airport, whereas it increases at seven other

airports. This dichotomy is shown to consistently relate to the background ratio of VOC and NO_x concentrations (VOC/NO_x ratio). A VOC/NO_x threshold between 2 and 2.15 is found for the included VOC species above which a location is said to be in a NO_x-limited regime. In this regime, decreases in NO_2 concentrations are associated with decreases in O_3 concentrations (and vice versa). These results show that mitigation of air pollution regarding O_3 is less straightforward than for NO_2 and $PM_{2.5}$, and that it requires a site-by-site assessment of local background concentrations.

Lower air traffic emissions are associated with local decreases (increases) in NO_2 and $PM_{2.5}$ (O_3) concentrations at Eindhoven and Rotterdam-The Hague Airport, in the order of a couple of tens of micrograms per cubic meter of air. Decreases in absolute NO_2 concentrations are greater at Eindhoven than at Rotterdam-The Hague, possibly because there is more air traffic associated with Eindhoven Airport. However, differences in NO_2 concentrations at Eindhoven decline faster when moving away from the airport. Higher wind speeds are found around Rotterdam-The Hague Airport which allows for transport of air pollutants over longer distances from the airport, possibly explaining this difference. It becomes clear that the presence of those airports have an impact on air quality in the direct vicinity of those airports within a ~10 km radius. For Amsterdam Schiphol Airport - one of Europe's largest airports - the signatures are much less clear. Overall changes in air quality are low when considering the size of Schiphol. This, combined with large model discrepancies compared to observations, indicate that modeling errors occurred for this region[1].

Furthermore, this study shows that at roughly 32% of locations, the two-week mean NO_2 concentrations are above the annual WHO guideline concentration of 10 μg m^{-3}. Yet, NO_2 background concentrations are found to be lower in summer than during fall or winter within the study domain. It is therefore plausible that the annual WHO guideline concentration is exceeded at many more locations when considered for a whole year. Similar reasoning applies to the exceedance of 24-hour guideline concentrations, for which it was found that 41-44 out of 10,000 locations exceeded the WHO guideline concentration at least once during the first two weeks of June 2019. 33-35 out of 10,000 locations even surpassed the yearly 99th percentile allowance (four times per year); an underestimation of the number of locations when considered for a whole year. Differences between scenarios are small and occur at locations where the background concentrations are close to the guideline concentrations.

For fine particulates, 84% of locations exceed the annual WHO guideline concentration of 5% μg m^{-3}, despite relatively low $PM_{2.5}$ concentrations found during the study period compared to other periods of the year. Also, 673-687 out of 10,000 locations exceed the 24-hour guideline at least four times during the first two weeks of June. No air traffic emissions (scenario IV) seem to prevent 14 out of 10,000 locations from surpassing this threshold during this period. It is seen that the number of locations classified as having poor air quality decrease monotonically when moving from scenario I to scenario IV. This makes it convincing that those decreases are attributable to a cleaner aviation sector, despite absolute changes being low.

It is shown that inter-daily fluctuations in O_3 concentrations are higher than for NO_2 and $PM_{2.5}$ during the fortnight simulation period, and that the found locations exceeding the 8-hour mean WHO guideline value of 100 μg m^{-3} may be even more sensitive to the simulated period than NO_2 and $PM_{2.5}$. In contrast to NO_2 and $PM_{2.5}$, O_3 background concentrations peak in June, and thereby the calculated number of locations exceeding the WHO guideline concentration at least four times would correspond closest to the number found when the entire year would have been simulated. As for $PM_{2.5}$, a monotonic decrease in locations exceeding guideline concentrations (at least four times) is found when moving to cleaner aviation emission scenarios, from 2,024 per 10,000 locations in scenario I to 1,977 per 10,000 locations in scenario IV.

The relatively small proportion of locations where the WHO guideline concentrations are exceeded in June - particularly for NO_2 - does not necessarily indicate that a small proportion of individuals are exposed to hazardous concentrations. Most locations above guideline concentrations are expected to be highly populated, or in the vicinity of transportation routes where large number of individuals reside, as these are the locations where most pollutants are emitted. Regardless, the European Union strives for compliance with air quality guidelines at *all* locations as clean air is regarded as a human right, enshrined in EU legislation [EU, 2008].

[1] This could not be verified due to server problems during the execution of this study.

Overall, it is shown using observational data that high intra-annual variability in domain-wide background concentrations dominate the variability in concentrations between scenarios. Therefore, it is recommended to perform simulations over different seasons of the year, as shifts between scenarios in local compliance with air quality guidelines are highly dependent on the time of the year. Increasing the simulation time to several years would extend the framework of this study by inclusion of carbon dioxide emissions and their related effects, changes in methane concentrations due to changes in the hydroxyl radical concentrations, and other involved species with a long atmospheric lifetime. Due to the coupling between chemistry and atmospheric dynamics, all those factors should be incorporated for a complete assessment of changes in air quality due to aviation. Longer simulation times would also allow for a more realistic, step-wise implementation of H_2 propulsion in aviation, involving the time dimension in the study. As large-scale H_2 propulsion in commercial aviation still has a way to go, the use of future projections for anthropogenic ground emissions, up-scaling of air traffic movements according to the projected sector growth, and future climate projections would add to the realism and quantitative accuracy of this study.

A major drawback of the performed simulations with WRF-Chem was the restriction to input water vapor as an anthropogenic emission. In the context of this study, water vapor is particularly interesting, as the elimination of carbon (and sulfuric) emissions with H_2 fuel goes at the cost of higher water vapor emissions. Although short-lived, water vapor is known as a potent greenhouse gas, and through its influence on cloud and aerosol formation, it could impact air quality in various manners.

Bibliography

Airbus. Global Market Forecast 2019-2038. https://www.airbus.com/aircraft/market/global-market-forecast.html, 2019. Last accessed: Sep 20 2021.

Airbus. ZEROe: Towards the world's first zero-emission commercial aircraft. https://www.airbus.com/en/innovation/zero-emission/hydrogen/zeroe, 2020a. Last accessed: Dec 03 2021.

Airbus. Hydrogen fuel cells, explained. https://www.airbus.com/newsroom/news/en/2020/10/hydrogen-fuel-cell-cross-industry-collaboration-potential-for-aviation.html, 2020b. Last accessed: Oct 14 2021.

J. Altenstedt and K. Pleijel. An Alternative Approach to Photochemical Ozone Creation Potentials Applied under European Conditions. *Journal of the Air Waste Management Association*, 50:1023–1036, 2000. DOI: 10.1080/10473289.2000.10464145.

A. Arakawa and V. Lamb. Computational design of the basic dynamical processes of the UCLA general circulation model. *Methods in Computational Physics*, 17:174–267, 1977. DOI: 10.1016/B978-0-12-460817-7.50009-4.

ATSDR. Toxicological Profile For Jet Fuels JP-4 and JP-7, 1995. Agency for Toxic Substances and Disease Registry. Last accessed: Dec 15 2021.

A. Balzarini, G. Pirovano, L. Honzak, R. Zabkar, G. Curci, R. Forkel, M. Hirtl, R. San José, P. Tuccella, and G. Grell. WRF-Chem model sensitivity to chemical mechanisms choice in reconstructing aerosol optical properties. *Atmospheric Environment*, 115:604–619, 2015. DOI: 10.1016/j.atmosenv.2014.12.033.

F. Bernardini, L. Attademo, R. Trezzi, C. Gobbicchi, P. Balducci, V. Del Bello, G. Menculini, L. Pauselli, M. Piselli, T. Sciarma, P. Moretti, A. Tamantini, R. Quartesan, M. Compton, and A. Tortorella. Air pollutants and daily number of admissions to psychiatric emergency services: evidence for detrimental mental health effects of ozone. *Epidemiology and psychiatric sciences*, 29, 2020. DOI: 10.1017/S2045796019000623.

C. J. Bucaram and F. M. Bowman. WRF-Chem Modeling of Summertime Air Pollution in the Northern Great Plains: Chemistry and Aerosol Mechanism Intercomparison. *Atmosphere*, 12:505–521, 2021. DOI: 10.3390/atmos12091121.

R. R. Buchholz, L. K. Emmons, S. Tilmes, and T. C. D. Team. CESM2.1/CAM-chem Instantaneous Output for Boundary Conditions. UCAR/NCAR. *Atmospheric Chemistry Observations and Modeling Laboratory*, 2019. DOI: 10.5065/NMP7-EP60. Subset used: Lat: 42 to 63, Lon: 352.5 to 17.5, May 30 2019 - Jun 15 2019. Last accessed: Sep 30 2021.

U. Burkhardt, L. Bock, and A. Bier. Mitigating the contrail cirrus climate impact by reducing aircraft soot number emissions. *Climate and Atmospheric Science*, 1, 2018. DOI: 10.1038/s41612-018-0046-4.

R. Chen, P. Yin, X. Meng, L. Wang, C. Liu, Y. Niu, Z. Lin, Y. Liu, J. Liu, J. Qi, J. You, H. Kan, and M. Zhou. Associations between ambient nitrogen dioxide and daily cause-specific mortality: evidence from 272 Chinese cities. *Epidemiology*, 29:482–489, 2018. DOI: 10.1097/EDE.0000000000000829.

R. Cichowicz, G. Wielgosinski, and W. Fetter. Dispersion of atmospheric air pollution in summer and winter season. *Environmental Monitoring and Assessment*, 189:605, 2017. DOI: 10.1007/s10661-017-6319-2.

CLO. Verzuring en grootschalige luchtverontreiniging: emissies, 1990 - 2019. https://www.clo.nl/indicatoren/nl018325-verzuring-en-grootschalige-luchtverontreiniging-emissies, 2021. Centraal Bureau voor de Statistiek (CBS), Planbureau voor de Leefomgeving (PBL), Rijksinstituut voor Volksgezondheid en Milieu (RIVM) and Wageningen University Research (WUR). Last accessed: Aug 29 2021.

W. D. Collins, P. J. Rasch, B. A. Boville, J. J. Hack, J. R. McCaa, D. L. Williamson, J. T. Kiehl, and B. Briegleb. Description of the NCAR Community Atmosphere Model (CAM 3.0). https://www.cesm.ucar.edu/models/atm-cam/docs/description/description.pdf, 2004. Last accessed: Oct 02 2021.

D. DuBois and G. C. Paynter. "Fuel Flow Method2" for Estimating Aircraft Emissions. *Journal of Aerospace*, 115:1–14, 2006. DOI: 10.4271/2006-01-1987.

G. Duveiller, D. Fasbender, and M. Meroni. Revisiting the concept of a symmetric index of agreement for continuous datasets. *Scientific Reports*, 6:19401, 2016. DOI: 10.1038/srep19401.

EASA, EEA and EUROCONTROL. European Aviation Environmental Report. https://ec.europa.eu/transport/sites/default/files/2019-aviation-environmental-report.pdf, 2019. European Aviation Safety Agency (EASA), European Environment Agency (EEA), EUROCONTROL. Last accessed: Oct 11 2021.

EC. Final energy consumption in transport by type of fuel, 2019. European Commission: Eurostat. Last accessed: Dec 15 2021.

EC. Updated analysis of the non-CO_2 climate impacts of aviation and potential policy measures pursuant to EU Emissions Trading System Directive Article 30(4). https://eur-lex.europa.eu/legal-content/EN/TXT/?uri=SWD:2020:277:FIN, 2020. European Commission. Last accessed: Dec 02 2021.

EC. European Green Deal: Commission aims for zero pollution in air, water and soil. https://ec.europa.eu/environment/strategy/zero-pollution-action-plan, 2021. European Commission. Last accessed: Dec 03 2021.

ECMWF. MACC-III: Monitoring Atmospheric Composition and Climate 3. https://atmosphere.copernicus.eu/sites/default/files/repository/MACCIII_FinalReport.pdf, 2016. Last accessed: Sep 02 2021.

EEA. EMEP/EEA air pollutant emission inventory guidebook 2019. https://www.eea.europa.eu/publications/emep-eea-guidebook-2019, 2019. European Environment Agency. Last accessed: Nov 22 2021.

EEA. AirBase: Air Quality e-Reporting. https://www.eea.europa.eu/data-and-maps/data/aqereporting-9, 2021a. European Environment Agency. Last accessed: Nov 17 2021.

EEA. Air quality in Europe 2021. *European Environment Agency*, 15, 2021b. DOI: 10.2800/549289.

EEA. Air quality standards. https://www.eea.europa.eu/themes/air/air-quality-concentrations/air-quality-standards, 2021c. European Environment Agency. Last accessed: Dec 03 2021.

S. Elvidge, M. Angling, and B. Nava. On the use of modified Taylor diagrams to compare ionospheric assimilation models. *Radio Science*, 49:737–745, 2014. DOI: 10.1002/2014RS005435.

L. K. Emmons, R. H. Schwantes, J. J. Orlando, G. Tyndall, D. Kinnison, J.-F. Lamarque, D. Marsh, M. J. Mills, S. Tilmes, C. Bardeen, R. R. Buchholz, A. Conley, A. Gettelman, R. Garcia, I. Simpson, D. R. Blake, S. Meinardi, and G. Pétron. The Chemistry Mechanism in the Community Earth System Model Version 2 (CESM2). *Journal of Advances in Modeling Earth Systems*, 12, 2020. DOI: 10.1029/2019MS001882.

EU. *On ambient air quality and cleaner air for Europe*. European Parliament and the Council of the European Union, 2008.

EUROCONTROL. Standard Inputs for EUROCONTROL Cost-Benefit Analyses. https://www.eurocontrol.int/sites/default/files/2021-03/eurocontrol-standard-inputs-economic-analysis-ed-7.pdf, 2015. Last accessed: Oct 08 2021.

EUROCONTROL. European Aviation in 2040: Challenges of Growth. https://www.eurocontrol.int/sites/default/files/2019-07/challenges-of-growth-2018-annex1_0.pdf, 2019. Annex 1: Flight Forecast to 2040. Last accessed: Dec 03 2021.

EUROCONTROL. R&D Data Archive. https://www.eurocontrol.int/dashboard/rnd-data-archive, 2020. Last accessed: May 28 2021.

EUROCONTROL. Advanced Emission Model v2.5.5. https://www.eurocontrol.int/model/advanced-emission-model, 2021a. Last accessed: Sep 19 2021.

EUROCONTROL. *AEM Kernel User Guide*. EUROCONTROL, 2021b.

FAA. Aviation & Emissions: A Primer. https://www.faa.gov/regulations_policies/policy_guidance/envir_policy/media/aeprimer.pdf, 2005. Federal Aviation Administration: Office of Environment and Energy. Last accessed: Sep 27 2021.

FBI. Aircraft market research report. https://www.fortunebusinessinsights.com/industry-reports/aircraft-engine-market-101766, 2020. Fortune Business Insights. Report ID: FBI101766.

FCH JU. Hydrogen-powered aviation: A fact-based study of hydrogen technology, economics, and climate impact by 2050. https://www.fch.europa.eu/sites/default/files/FCH%20Docs/20200720_Hydrogen%20Powered%20Aviation%20report_FINAL%20web.pdf, 2020. Fuel Cells and Hydrogen Joint Undertaking. Last accessed: Oct 09 2021.

G. G. Fleming and I. De Lépinay. Environmental Trends in Aviation to 2050. https://www.icao.int/environmental-protection/Documents/EnvironmentalReports/2019/ENVReport2019_pg17-23.pdf, 2019. Last accessed: Sep 14 2021.

FNL. NCEP FNL Operational Model Global Tropospheric Analyses, continuing from July 1999., 2000. National Centers for Environmental Prediction/National Weather Service/NOAA/U.S. Department of Commerce. Last accessed: Sep 30 2021.

FOCA. Aircraft Piston Engine Database. https://www.bazl.admin.ch/bazl/en/home/specialists/regulations-and-guidelines/environment/pollutant-emissions/aircraft-engine-emissions/report--appendices--database-and-data-sheets.html, 2021. Federal Office of Civil Aviation. Last accessed: Sep 19 2021.

FOI. Database for Turboprop Engine Emissions. https://www.foi.se/en/foi/research/aeronautics-and-space-issues/environmental-impact-of-aircraft.html, 2021. Swedish Defence Research Agency. Last accessed: Sep 19 2021.

M. Gauss, I. Isaksen, S. Wong, and W.-C. Wang. Impact of H_2O emissions from cryoplanes and kerosene aircraft on the atmosphere. *Climate and Dynamics*, 108, 2003. DOI: 10.1029/2002JD002623.

P. Ginoux, M. Chin, I. Tegen, J. M. Prospero, B. Holben, O. Dubovik, and S.-J. Lin. Sources and distributions of dust aerosols simulated with the GOCART model. *Journal of Geophysical Research*, 106:20255–20273, 2001. DOI: 10.1029/2000JD000053.

G. A. Grell. Prognostic Evaluation of Assumptions Used by Cumulus Parameterizations. *Monthly Weather Review*, 121:764–787, 1993. DOI: 10.1175/1520-0493(1993)121<0764:PEOAUB>2.0.CO;2.

G. A. Grell and D. Dévényi. A generalized approach to parameterizing convection combining ensemble and data assimilation techniques. *Geophysical Research Letters*, 29:381–384, 2002. DOI: 10.1029/2002GL015311.

S. C. Herndon, J. H. Shorter, M. S. Zahniser, D. D. Nelson, J. Jayne, R. C. Brown, R. C. Miake-Lye, I. Waitz, P. Silva, T. Lanni, K. Demerjian, and C. E. Kolb. NO and NO_2 Emission Ratios Measured from In-Use Commercial Aircraft during Taxi and Takeoff. *Environmental Science & Technology*, 38, 2004. DOI: 10.1021/es049701c.

O. Hodnebrog, T. Berntsen, O. Dessens, M. Gauss, V. Grewe, I. Isaksen, B. Koffi, G. Myhre, D. Olivié, M. Prather, F. Stordal, S. Szopa, Q. Tang, P. Van Velthoven, and J. Williams. Future impact of traffic emissions on atmospheric ozone and OH based on two scenarios. *Atmospheric Chemistry and Physics*, 12:12211–12225, 2012. DOI: 10.5194/acp-12-12211-2012.

S.-Y. Hong, Y. Noh, and J. Dudhia. A New Vertical Diffusion Package with an Explicit Treatment of Entrainment Processes. *Monthly Weather Review*, 121:2318–2341, 2006. DOI: 10.1175/MWR3199.1.

P. Hoor, J. Borken-Kleefeld, D. Caro, O. Dessens, O. Endresen, M. Gauss, V. Grewe, D. Hauglustaine, I. S. A. Isaksen, P. Jöckel, J. Lelieveld, G. Myhre, E. Meijer, D. Olivie, M. Prather, C. Schnadt Poberaj, K. P. Shine, J. Staehelin, Q. Tang, J. van Aardenne, P. van Velthoven, and R. Sausen. The impact of traffic emissions on atmospheric ozone and OH: results from QUANTIFY. *Atmospheric Chemistry and Physics*, 9:3113–3136, 2009. DOI: 10.5194/acp-9-3113-2009.

ICAO. The World of Air Transport in 2019. https://www.icao.int/annual-report-2019/Pages/the-world-of-air-transport-in-2019.aspx, 2019. International Civil Aviation Organization. Last accessed: Sep 21 2021.

ICAO. Aircraft Engine Emissions Databank. https://www.easa.europa.eu/domains/environment/icao-aircraft-engine-emissions-databank#group-easa-downloads, 2021. International Civil Aviation Organization. Last accessed: Sep 19 2021.

IPCC. Aviation and the Global Atmosphere. *Cambridge University Press*, 1999. Intergovernmental Panel on Climate Change.

P. A. Jiménez, J. Dudhia, J. F. González-Rouco, J. Navarro, J. P. Montávez, and E. García-Bustamante. A Revised Scheme for the WRF Surface Layer Formulation. *Monthly Weather Review*, 140:898–918, 2012. DOI: 10.1175/MWR-D-11-00056.1.

C.-R. Jung, Y.-T. Lin, and B.-F. Hwang. Ozone, particulate matter, and newly diagnosed Alzheimer's disease: a population-based cohort study in Taiwan. *Journal of Alzheimer's Disease*, 44:573–584, 2015. DOI: 10.3233/JAD-140855.

Z. Z. Kapadia, A.-S. R. Spracklen, Dominick V. and, D. J. Borman, G. W. Mann, K. J. Pringle, S. A. Monks, C. L. Reddington, F. Benduhn, A. Rap, C. E. Scott, E. W. Butt, , and M. Yoshioka. Impacts of aviation fuel sulfur content on climate and human health. *Atmospheric Chemistry and Physics*, 16:10521–10541, 2016. DOI: 10.5194/acp-16-10521-2016.

KNMI. Impact of emissions from shipping, aviation and road traffic on atmospheric composition and climate. https://www.knmi.nl/kennis-en-datacentrum/achtergrond/impact-of-emissions-from-shipping-aviation-and-road-traffic-on-atmospheric-composition-and-climate, 2007. Koninklijk Nederlands Meteorologisch Instituut. Last accessed: Sep 28 2021.

J. S. Kurniawan and S. Khardi. Comparison of methodologies estimating emissions of aircraft pollutants, environmental impact assessment around airports. *Environmental Impact Assessment Review*, 31:240–252, 2011. DOI: 10.1016/j.eiar.2010.09.001.

T. Kärnä and A. Baptista. Evaluation of a long-term hindcast simulation for the Columbia River estuary. *Ocean Modelling*, 99:1–14, 2016. DOI: 10.1016/j.ocemod.2015.12.007.

D. Lee, D. Fahey, A. Skowron, M. Allen, U. Burkhardt, Q. Chen, S. Doherty, S. Freeman, P. Forsterg, J. Fuglestvedt, A. Gettelman, R. De León, L. Lima, M. Lund, R. Millar, B. Owen, J. Penner, G. Pitari, and L. Wilcox. The contribution of global aviation to anthropogenic climate forcing for 2000 to 2018. *Atmospheric Environment*, 244, 2021. DOI: 10.1016/j.atmosenv.2020.117834.

D. S. Lee, D. W. Fahey, P. M. Forster, P. J. Newton, R. C. Wite, L. L. Lim, B. Owen, and R. Sausen. Aviation and global climate change in the 21st century. *Atmospheric Environment*, 43, 2009. DOI: 10.1016/j.atmosenv.2009.04.024.

M. Masiol and R. M. Harrison. Aircraft engine exhaust emissions and other airport-related contributions to ambient air pollution: A review. *Atmospheric Environment*, 95, 2014. DOI: 10.1016/j.atmosenv.2014.05.070.

B. Matthews and R. Wankmueller. Methodologies applied to the CEIP GNFR gap-filling 2021 Part I: Main Pollutants (NO_x, NMVOCs, SO_x, NH_3, CO), Particulate Matter ($PM_{2.5}$, PM_{10}, PM_{coarse}), and Black Carbon (BC) for the years 2000 to 2019, 2021. Last accessed: Oct 03 2021.

H. Morrison, G. Thompson, and V. Tatarskii. Impact of Cloud Microphysics on the Development of Trailing Stratiform Precipitation in a Simulated Squall Line: Comparison of One- and Two-Moment Schemes. *Monthly Weather Review*, 137:991–1007, 2009. DOI: 10.1175/2008MWR2556.1.

A. Nuic, D. Poles, and V. Mouillet. BADA: An advanced aircraft performance model for present and future ATM systems. *International Journal of Adaptive Control and Signal Processing*, 2010. DOI: 10.1002/acs.1176.

M. Ponater, S. Pechtl, R. Sausen, U. Schumann, and G. Hüttig. Potential of the cryoplane technology to reduce aircraft climate impact: A state-of-the-art assessment. *Atmospheric Environment*, 40:6928–6944, 2006. DOI: 10.1016/j.atmosenv.2006.06.036.

J. Pulles, S. Lowe, R. Van Drimmelen, G. Baarse, and P. McMahon. The AERO-project. Model description and status. *Dutch Civil Aviation Department*, 3:247–257, 1995. DOI: 10.5094/APR.2012.027.

A. G. Rao, F. Yin, and H. G. Werij. Energy Transition in Aviation: The Role of Cryogenic Fuels. *Aerospace*, 7:181, 2020. DOI: 10.3390/aerospace7120181.

Rijksoverheid. Het Schone Lucht Akkoord. https://www.schoneluchtakkoord.nl/schone-lucht-akkoord/, 2020. Dutch Ministry of Infrastructure and Water Management, Rijksinstituut voor Volksgezondheid en Milieu (RIVM), Rijkswaterstaat, provinces and municipalities. Last accessed: Oct 16 2021.

K. Riley, R. Cook, E. Carr, and B. Manning. A systematic review of the impact of commercial aircraft activity on air quality near airports. *City and Environment Interactions*, 5:100066, 2021. DOI: 10.1016/j.cacint.2021.100066.

RIVM, DCMR and others. Luchtmeetnet. https://www.luchtmeetnet.nl/, 2021. Involved parties are Rijksinstituut voor Volksgezondheid en Milieu (RIVM), Ministerie van Infrastructuur en Waterstaat (IenW), GGD Amsterdam, DCMR Milieudienst Rijnmond, Regionale Uitvoeringsdienst Zuid-Limburg (RUDZL), Omgevingsdienst Midden- en West-Brabant (OMWB) and Omgevingsdienst regio Arnhem (ODRA). Used data in this study is from RIVM and DCMR. Last accessed: Nov 14 2021.

P. Roberts, L. White, L. Post, L. Tarrason, S. Tsyro, R. Stern, A. Kerschbaumer, L. Rouil, B. Bessagnet, R. Bergström, M. Schaap, G. Boersen, P. Boersen, P. Thunis, and C. Cuvelier. Evaluation of a Sectoral Approach to Integrated Assessment Modelling Including the Mediterranean Sea. https://publications.jrc.ec.europa.eu/repository/handle/JRC41801, 2008. EUR 23444 EN. Luxembourg (Luxembourg): OPOCE.

D. Roberts–Semple, F. Song, and Y. Gao. Seasonal characteristics of ambient nitrogen oxides and ground–level ozone in metropolitan northeastern New Jersey. *Atmospheric Pollution Research*, 3: 247–257, 2012. DOI: 10.5094/APR.2012.027.

Roland Berger. Hydrogen: A future fuel for aviation?, 2020. Last accessed: Dec 05 2021.

M. Schaefer and S. Bartosch. Overview on fuel flow correlation methods for the calculation of NO_x, CO and HC emissions and their implementation into aircraft performance software. *Deutsches Zentrum für Luft- und Raumfahrt (DLR)*, IB-325-11-13, 2013.

U. Schumann. Aircraft Emissions. *Causes and consequences of global environmental change*, 3: 178–186, 2002.

J. H. Seinfeld and S. N. Pandis. *Atmospheric Chemistry and Physics: From Air Pollution to Climate Change*. Wiley, 3 edition, 2016.

P. Sicard, P. Crippa, A. De Marco, S. Castruccio, P. Giani, J. Cuesta, E. Paoletti, Z. Feng, and A. Anav. High spatial resolution WRF-Chem model over Asia: Physics and chemistry evaluation. *Atmospheric Environment*, 244:118004, 2021. DOI: 10.1016/j.atmosenv.2020.118004.

D. Simpson, A. Benedictow, H. Berge, R. Bergstrom, L. Emberson, H. Fagerli, C. Flechard, G. Hayman, M. Gauss, J. Jonson, M. Jenkin, A. Nyíri, C. Richter, V. Semeena, S. Tsyro, J.-P. Tuovinen, A. Valdebenito, and P. Wind. The EMEP MSC-W chemical transport model – technical description. https://acp.copernicus.org/articles/12/7825/2012/acp-12-7825-2012-supplement.pdf, 2012a. Last accessed: Oct 04 2021.

D. Simpson, A. Benedictow, H. Berge, R. Bergström, L. Emberson, H. Fagerli, C. Flechard, G. Hayman, M. Gauss, J. Jonson, M. Jenkin, A. Nyíri, C. Richter, V. Semeena, S. Tsyro, □. Tuovinen, J.-P. Valdebenito, and P. Wind. The EMEP MSC-W chemical transport model – technical description. *Atmospheric Chemistry and Physics*, 12:7825–7865, 2012b. DOI: 10.5194/acp-12-7825-2012.

W. C. Skamarock, J. B. Klemp, J. Dudhia, D. O. Gill, D. M. Barker, X.-Y. Duda, M. G Huang, W. Wang, and J. G. Powers. A Description of the Advanced Research WRF Version 3. *NCAR Tech. Note NCAR/TN-475+STR*, 121:113 pp., 2008. DOI: 10.5065/D68S4MVH.

T. L. Spero, C. G. Nolte, M. S. Mallard, and J. H. Bowden. A Maieutic Exploration of Nudging Strategies for Regional Climate Applications Using the WRF Model. *Journal of Applied Meteorology and Climatology*, 57:1883–1906, 2018. DOI: 10.1175/JAMC-D-17-0360.1.

D. R. Stauffer and N. L. Seaman. Multiscale Four-Dimensional Data Assimilation. *Journal of Applied Meteorology and Climatology*, 33:416–434, 1994. DOI: 10.1175/1520-0450(1994)033<0416:MFDDA>2.0.CO;2.

T. Stocker, D. Qin, G.-K. Plattner, M. Tignor, S. Allen, J. Boschung, A. Nauels, Y. Xia, V. Bex, and P. Midgley. Climate Change 2013: The Physical Science Basis. Contribution of Working Group I to the Fifth Assessment Report of the Intergovernmental Panel on Climate Change. AR5, 2013.

K. Taylor. Summarizing multiple aspects of model performance in a single diagram. *Journal of Geophysical Research*, 106:7183– 7192, 2001. DOI: 10.1029/2000JD900719.

S. Tilmes, A. Hodzic, L. K. Emmons, M. J. Mills, A. Gettelman, D. E. Kinnison, M. Park, J.-F. Lamarque, F. Vitt, M. Shrivastava, P. Campuzano-Jost, J. L. Jimenez, and X. Liu. Climate Forcing and Trends of Organic Aerosols in the Community Earth System Model (CESM2). *Journal of Advances in Modeling Earth Systems*, 11:4323–4351, 2019. DOI: 10.1029/2019MS001827.

H. D. van der Gon, A. Visschedijk, and J. Kuenen. TNO Monitoring Atmospheric Composition and Climate 3 (TNO-MACC-III) Data Product, 2014. Last accessed: Oct 03 2021.

R. Vecchi, G. Marcazzan, G. Valli, M. Cerini, and C. Antoniazzi. The role of atmospheric dispersion in the seasonal variation of PM_1 and $PM_{2.5}$ concentration and composition in the urban area of Milan (Italy). *Atmopheric Environment*, 38:4437–4446, 2004. DOI: 10.1016/j.atmosenv.2004.05.029.

R. Von Glasow and P. Crutzen. *Treatise on Geochemistry: The Atmosphere*. 2 edition, 2014.

H. Wang, J. Lin, Q. Wu, H. Chen, X. Tang, Z. Wang, X. Chen, H. Cheng, and L. Wang. MP CBM-Z V1.0: design for a new Carbon Bond Mechanism Z (CBM-Z) gas-phase chemical mechanism architecture for next-generation processors. *Geoscientific Model Development*, 12:749–764, 2019. DOI: 10.5194/gmd-12-749-2019.

E. Weijers, G. Kos, M. Blom, R. Otjes, M. M. Schaap, and E. Van der Swaluw. Measurements of secondary inorganic aerosols in The Netherlands. https://www.rivm.nl/sites/default/files/2018-11/Measurements%20of%20secondary%20inorganic%20aerosols%20in%20The%20Netherlands.pdf, 2012. Last accessed: Oct 11 2021.

WHO. WHO global air quality guidelines: particulate matter ($PM_{2.5}$ and PM_{10}), ozone, nitrogen dioxide, sulfur dioxide and carbon monoxide. https://apps.who.int/iris/handle/10665/345329, 2021. World Health Organization. License: CC BY-NC-SA 3.0 IGO. Last accessed: Oct 17 2021.

O. Wild, X. Zhu, and M. J. Prather. Fast-J: Accurate Simulation of In- and Below-Cloud Photolysis in Tropospheric Chemical Models. *Journal of Atmospheric Chemistry*, 37:245–282, 2000. DOI: 10.1023/A:1006415919030.

J. Willemsen. Juni 2019: de warmste junimaand sinds 1901. https://www.weeronline.nl/nieuws/weeroverzichten-2019-juni, 2020. Last accessed: Sep 30 2021.

C. J. Willmott. On the Validation of Models. *Physical Geography*, 2:184–194, 1981.

J. Wormhoudt, S. Herndon, P. Yelvington, and C. Lye-Miake, R.C.and Wey. Nitrogen Oxide (NO/NO_2/HONO) Emissions Measurements in Aircraft Exhausts. *Journal of Propulsion and Power*, 23, 2007. DOI: 10.2514/1.23461.

J. Yang, S. Kang, and Z. Ji. Sensitivity Analysis of Chemical Mechanisms in the WRF-Chem Model in Reconstructing Aerosol Concentrations and Optical Properties in the Tibetan Plateau. *Aerosol and Air Quality Research*, 18:505–521, 2018. DOI: 10.4209/aaqr.2017.05.0156.

A. Yerramilly, V. S. C. Challa, V. B. R. Dodla, L. Myles, W. R. Pendergrass, C. A. Vogel, F. Tuluri, J. M. Baham, R. Hughes, C. Patrick, J. Young, and S. Swanier. Simulation of surface ozone pollution in the Central Gulf Coast region during summer synoptic condition using WRF/Chem air quality model. *Atmospheric Pollution Research*, 3:55–71, 2012. DOI: 10.5094/APR.2012.005.

S. Yim, G. Lee, I. Lee, F. Allroggen, A. Ashok, F. Caiazzo, S. Eastham, R. Malina, and S. Barrett. Global, regional and local health impacts of civil aviation emissions. *Environmental Research Letters*, 10: 034001, 2015a. DOI: 10.1088/1748-9326/10/3/034001.

S. H. Yim, G. L. Lee, I. H. Lee, F. Allroggen, A. Ashok, F. Caiazzo, S. D. Eastham, R. Malina, and S. R. Barrett. Global, regional and local health impacts of civil aviation emissions. *Environmental Research Letters*, 10:034001, 2015b. DOI: 10.1088/1748-9326/10/3/034001/meta.

R. A. Zaveri and L. K. Peters. A new lumped structure photochemical mechanism for large-scale applications. *Journal of Geophysical Research*, 104:30387–30415, 2008. DOI: 10.1029/1999JD900876.

R. A. Zaveri, R. C. Easter, J. D. Fast, and L. K. Peters. Model for Simulating Aerosol Interactions and Chemistry (MOSAIC). *Journal of Geophysical Research*, 113, 2008. DOI: 10.1029/2007JD008782.

ZeroAvia. First commercial hydrogen-electric flight between London and Rotterdam The Hague Airport expected in 2024. https://www.zeroavia.com/rotterdam, 2021. Last accessed: Dec 08 2021.

L. Zhuo, Q. Dai, D. Han, N. Chen, and B. Zhao. Assessment of Simulated Soil Moisture from WRF Noah, Noah-MP, and CLM Land Surface Schemes for Landslide Hazard Application. *Hydrology and Earth System Sciences*, 23:4199–4218, 2019. DOI: 10.5194/hess-2019-95.

A

Namelists WRF-Chem

A.1. WPS Namelist

Go back to page 17.

```
&share
wrf_core             =   'ARW',
max_dom              =   4,
start_date           =   '2019-05-30_00:00:00',  '2019-05-30_00:00:00',
                         '2019-05-30_00:00:00',  '2019-05-30_00:00:00',
end_date             =   '2019-06-15_00:00:00',  '2019-06-15_00:00:00',
                         '2019-06-15_00:00:00',  '2019-06-15_00:00:00',
interval_seconds     =   21600,
io_form_geogrid      =   2,
debug_level          =   0,
/

&geogrid
parent_id            =   1,      1,      2,      3,
parent_grid_ratio    =   1,      3,      3,      3,
i_parent_start       =   1,      18,     17,     9,
j_parent_start       =   1,      14,     16,     8,
e_we                 =   49,     49,     49,     100,
e_sn                 =   40,     40,     40,     79,
geog_data_res        =   'modis_30s',    'modis_30s',
                         'modis_30s',    'modis_30s',
dx                   =   0.5,
dy                   =   0.5,
map_proj             =   'lat-lon',
stand_lon            =   1.0,
ref_lat              =   52,
ref_lon              =   5,
/

&ungrib
out_format           =   'WPS',
prefix               =   'FILE',
/

&metgrid
fg_name              =   'FILE',
```

```
io_form_metgrid     =   2,
/

&mod_levs
press_pa            =   200100, 100000, 97500,  95000,  92500,  90000,
                        85000,  80000,  75000,  70000,  65000,  60000,
                        55000,  50000,  45000,  40000,  35000,  30000,
                        25000,  20000,  15000,  10000,  7000,   5000,
                        3000,   3000,   2000,   1000
/
```

A.2. WRF Namelist

Go back to page 14.

```
&time_control
run_days                    =   0,
run_hours                   =   0,
run_minutes                 =   0,
run_seconds                 =   0,
start_year                  =   2019,   2019,   2019,   2019,
start_month                 =   05,     05,     05,     05,
start_day                   =   30,     30,     30,     30,
start_hour                  =   0,      0,      0,      0,
start_minute                =   0,      0,      0,      0,
start_second                =   0,      0,      0,      0,
end_year                    =   2019,   2019,   2019,   2019,
end_month                   =   06,     06,     06,     06,
end_day                     =   15,     15,     15,     15,
end_hour                    =   0,      0,      0,      0,
end_minute                  =   0,      0,      0,      0,
end_second                  =   0,      0,      0,      0,
interval_seconds            =   21600
input_from_file             =   .true., .true., .true., .true.,
history_interval            =   60,     60,     60,     60,
frames_per_outfile          =   24,     24,     24,     24,
restart                     =   .false.,
restart_interval            =   10080,
auxinput5_interval          =   60,     60,     60,     60,
io_form_history             =   2,
io_form_restart             =   2,
io_form_input               =   2,
io_form_boundary            =   2,
io_form_auxinput5           =   2,
frames_per_auxinput5        =   12,
auxinput5_inname            =   ”wrfchemi_<hour>z_d<domain>”,
debug_level                 =   0,
iofields_filename           =   ”my_out_fields.txt”, ”my_out_fields.txt”,
                                 ”my_out_fields.txt”, ”my_out_fields.txt”,
io_form_auxhist3            =   2,
auxhist3_interval           =   60,     60,     60,     60,
frames_per_auxhist3         =   24,     24,     24,     24,
/

&domains
time_step                    =   120,
max_dom                      =   4,
```

```
e_we                                =   49,     49,     49,     100,
e_sn                                =   40,     40,     40,     79,
e_vert                              =   22,     22,     22,     22,
dx                                  =   55588.7366760194,   18529.578892006462,
                                        6176.526297335488,  2058.842099111829,
dy                                  =   55588.7366760194,   18529.578892006462,
                                        6176.526297335488,  2058.842099111829,
num_metgrid_levels                  =   27,
grid_id                             =   1,      2,      3,      4,
parent_id                           =   1,      1,      2,      3,
i_parent_start                      =   1,      18,     17,     9,
j_parent_start                      =   1,      14,     16,     8,
parent_grid_ratio                   =   1,      3,      3,      3,
parent_time_step_ratio              =   1,      3,      3,      3,
feedback                            =   1,
eta_levels                          =   1.000,  0.993,  0.988,  0.976,  0.958,
                                        0.933,  0.901,  0.862,  0.816,  0.763,
                                        0.703,  0.636,  0.562,  0.481,  0.392,
                                        0.302,  0.225,  0.165,  0.120,  0.080,
                                        0.040,  0.000,
p_top_requested                     =   10000,
sfcp_to_sfcp                        =   .true.
/

&physics
mp_physics                          =   10,     10,     10,     10,
ra_lw_physics                       =   3,      3,      3,      3,
ra_sw_physics                       =   3,      3,      3,      3,
radt                                =   30,     30,     30,     30,
sf_sfclay_physics                   =   1,      1,      1,      1,
sf_surface_physics                  =   2,      2,      2,      2,
bl_pbl_physics                      =   1,      1,      1,      1,
bldt                                =   0,      0,      0,      0,
cu_physics                          =   5,      5,      5,      0,
shcu_physics                        =   0,      0,      0,      1,
cudt                                =   0,      0,      0,      0,
num_land_cat                        =   20,
progn                               =   1,      1,      1,      1,
cu_rad_feedback                     =   .true.
/

&fdda
grid_fdda                           =   2,      2,      2,      2,
gfdda_inname                        =   ”wrffdda_d<domain>”,
gfdda_interval_m                    =   360,    360,    360,    360,
gfdda_end_h                         =   8760,   8760,   8760,   8760,
io_form_gfdda                       =   2,
fgdt                                =   0,      0,      0,      0,
if_no_pbl_nudging_uv                =   1,      1,      1,      1,
if_no_pbl_nudging_t                 =   1,      1,      1,      1,
if_no_pbl_nudging_q                 =   1,      1,      1,      1,
if_no_pbl_nudging_ph                =   1,      1,      1,      1,
guv                                 =   0.0003, 0.0003, 0.0003, 0.0003,
gt                                  =   0.0003, 0.0003, 0.0003, 0.0003,
gq                                  =   0.000015,       0.000015,
                                        0.000015,       0.000015,
```

```
gph                                 =   0.0,     0.0,     0.0,     0.0,
xwavenum                            =   3,       3,       3,       3,
ywavenum                            =   3,       3,       3,       3,
if_ramping                          =   0,
/

&dynamics
w_damping                           =   0,
diff_opt                            =   1,
km_opt                              =   4,
diff_6th_opt                        =   0,       0,       0,       0,
diff_6th_factor                     =   0.12,    0.12,    0.12,    0.12,
base_temp                           =   290.,
damp_opt                            =   3,
zdamp                               =   5000.0, 5000.0, 5000.0, 5000.0,
dampcoef                            =   0.2,     0.2,     0.2,     0.2,
khdif                               =   0,       0,       0,       0,
kvdif                               =   0,       0,       0,       0,
non_hydrostatic                     =   .true., .true., .true., .true.,
moist_adv_opt                       =   2,       2,       2,       2,
scalar_adv_opt                      =   2,       2,       2,       2,
chem_adv_opt                        =   2,       2,       2,       2,
/

&bdy_control
spec_bdy_width                      =   5,
spec_zone                           =   1,
relax_zone                          =   4,
specified                           =   .true., .false.,.false.,.false.,
nested                              =   .false.,.true., .true., .true.,
/

&grib2
/

&chem
kemit                               =   21,
chem_opt                            =   32,      32,      32,      32,
bioemdt                             =   30,      30,      30,      30,
photdt                              =   1,       1,       1,       1,
phot_opt                            =   2,       2,       2,       2,
chemdt                              =   1.0,     1.0,     1.0,     1.0,
io_style_emissions                  =   1,
emiss_inpt_opt                      =   102,     102,     102,     102,
emiss_opt                           =   4,       4,       4,       4,
chem_in_opt                         =   1,       1,       1,       1,
gas_drydep_opt                      =   1,       1,       1,       1,
aer_drydep_opt                      =   1,       1,       1,       1,
bio_emiss_opt                       =   1,       1,       1,       1,
dust_opt                            =   1,
dmsemis_opt                         =   1,
seas_opt                            =   2,
gas_bc_opt                          =   0,       0,       0,       0,
gas_ic_opt                          =   0,       0,       0,       0,
aer_bc_opt                          =   0,       0,       0,       0,
aer_ic_opt                          =   0,       0,       0,       0,
```

```
gaschem_onoff               =   1,      1,      1,      1,
aerchem_onoff               =   1,      1,      1,      1,
wetscav_onoff               =   1,      1,      1,      1,
cldchem_onoff               =   1,      1,      1,      1,
vertmix_onoff               =   1,      1,      1,      1,
chem_conv_tr                =   1,      1,      1,      0,
conv_tr_wetscav             =   1,      1,      1,      1,
conv_tr_aqchem              =   1,      1,      1,      1,
biomass_burn_opt            =   0,      0,      0,      0,
plumerisefire_frq           =   30,     30,     30,     30,
aer_ra_feedback             =   1,      1,      1,      1,
have_bcs_chem               =   .true., .true., .true., .true.,
have_bcs_tracer             =   .true., .true., .true., .true.,
chemdiag                    =   1,
n2o5_hetchem                =   1,
/

&namelist_quilt
nio_tasks_per_group         =   0,
nio_groups                  =   1,
/
```

B

Vertical Levels Model

Go back to page 16 or go back to page 27.

Table B.1. Model eta levels and the corresponding pressure levels.

η	p **(hPa)**	η	p **(hPa)**
1	1013.25	0.636	680.83
0.993	1006.86	0.562	613.25
0.988	1002.29	0.481	539.27
0.976	991.33	0.392	457.99
0.958	974.89	0.302	375.80
0.933	952.06	0.225	305.48
0.901	922.84	0.165	250.6
0.862	887.22	0.120	209.59
0.816	845.21	0.080	173.06
0.763	796.81	0.040	136.53
0.703	742.01	0.000	100.00

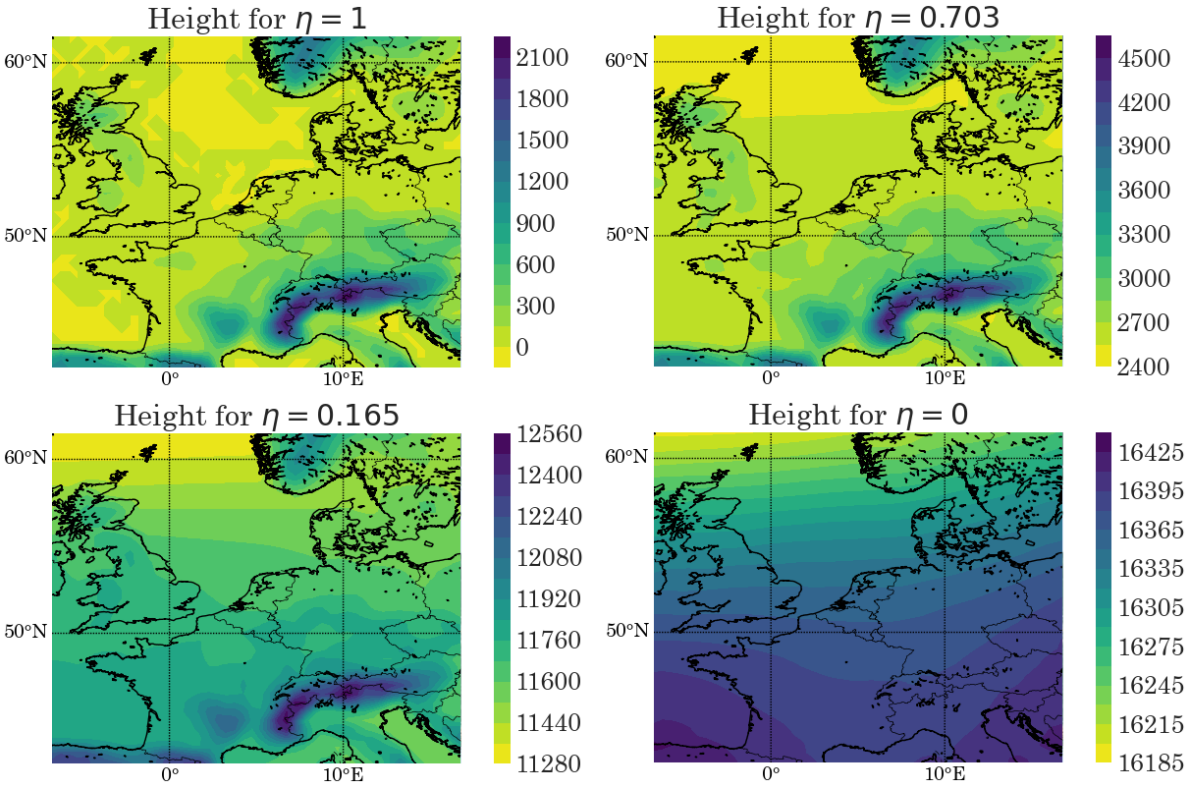

Figure B.1. Height in meters displayed on four different eta levels (ground level, intermediate level, aircraft cruise level and top of model). Values shown are averaged over time for a run on May 30th 2019, on domain 4.

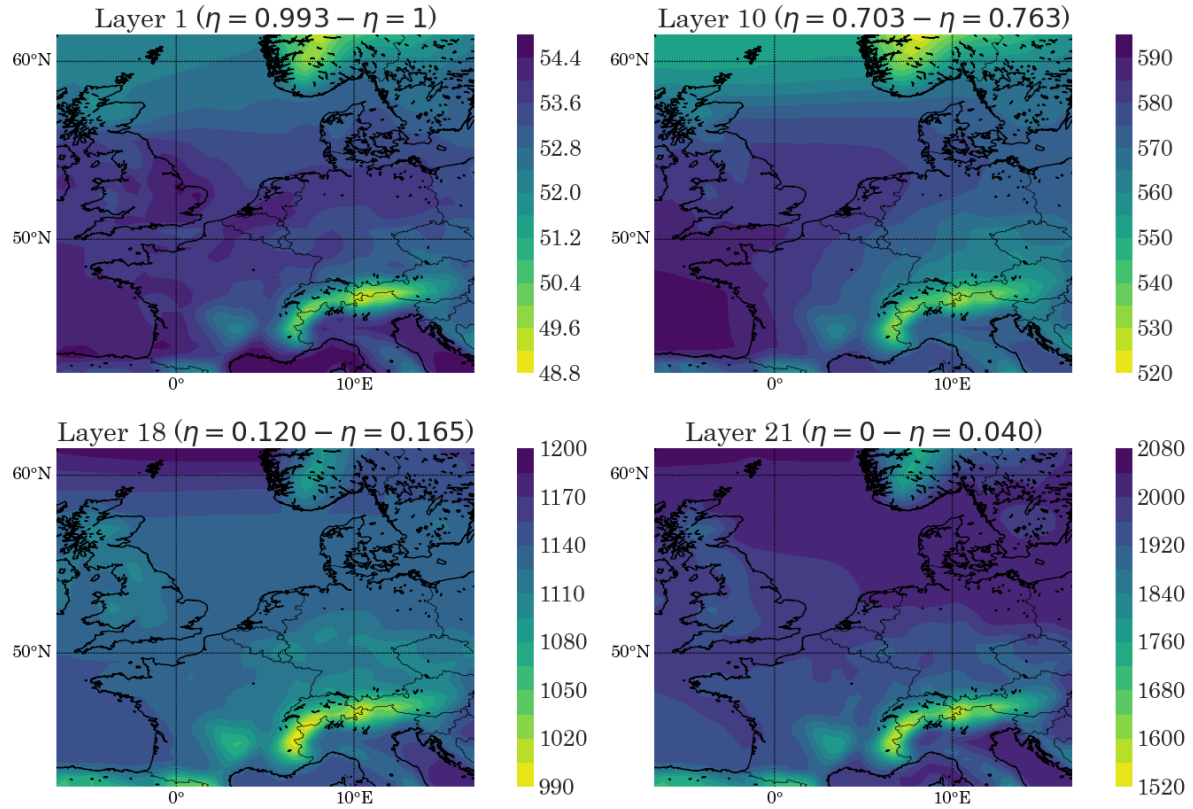

Figure B.2. Layer thickness in meters displayed on four different levels (ground level, intermediate level, aircraft cruise level and top of model). Values shown are averaged over time for a run on May 30th 2019, on domain 4.

C

AEM to CBM-Z Speciation

Go back to page 30.

Table C.1. Mapping of AEM species (on the horizontal) to CBM-Z species (on the vertical). Only the AEM species that have been mapped are included in the table. For all species, see EUROCONTROL [2021b]. The table shows weight factors by which AEM species masses are mapped to the respective CBM-Z species, for each emission case (case A_1/case A_2/case B). Mapping factors are based on the emiss_v03.F file within the WRF-Chem module.

AEM / CBM-Z	Acetal-dehyde	Propianol-dehyde	Acrolein	NO_x	CO	PM_{10}	HC	Formal-dehyde	1,3-Butadiene	Styrene	$PM_{2.5}$	SO_x	Benzene	Toluene	Xylene
E_ALD	0/0/1	0/0/1	0/0/0.5	x	x	x	x	x	x	x	x	x	x	x	x
E_C2H5OH	x	x	x	x	x	x	x	x	x	x	x	x	x	x	x
E_CH3OH	x	x	x	x	x	x	x	x	x	x	x	x	x	x	x
E_CO	x	x	x	x	0/0/1	x	x	x	x	x	x	x	x	x	x
E_ECJ	x	x	x	x	x	0/0/1	x	x	x	x	x	x	x	x	x
E_ETH	x	x	x	x	x	x	x	x	x	x	x	x	x	x	x
E_HC3	x	x	x	x	x	x	0/0/1	x	x	x	x	x	x	x	x
E_HC5	x	x	x	x	x	x	0/0/0	x	x	x	x	x	x	x	x
E_HC8	x	x	x	x	x	x	0/0/0	x	x	x	x	x	x	x	x
E_HCHO	x	x	x	x	x	x	x	0/0/1	x	x	x	x	x	x	x
E_ISO	x	x	x	x	x	x	x	x	x	x	x	x	x	x	x
E_KET	x	x	x	x	x	x	x	x	x	x	x	x	x	x	x
E_NH3	x	x	x	x	x	x	x	x	x	x	x	x	x	x	x
E_NO	x	x	x	0/0.315/0.9	x	x	x	x	x	x	x	x	x	x	x
E_NO2	x	x	x	0/0.035/0.1	x	x	x	x	x	x	x	x	x	x	x
E_OL2	x	x	x	x	x	x	x	x	x	x	x	x	x	x	x
E_OLI	x	x	x	x	x	x	x	x	0/0/0.5	x	x	x	x	x	x
E_OLT	x	x	0/0/0.5	x	x	x	x	x	0/0/0.5	0/0/1	x	x	x	x	x
E_ORA2	x	x	x	x	x	x	x	x	x	x	x	x	x	x	x
E_PM25I	x	x	x	x	x	x	x	x	x	x	0/0/0.2	x	x	x	x
E_PM25J	x	x	x	x	x	x	x	x	x	x	0/0/0.8	x	x	x	x
E_SO2	x	x	x	x	x	x	x	x	x	x	x	0/0/1	x	x	x
E_TOL	x	x	x	x	x	x	x	x	x	x	x	x	0/0/1	0/0/1	x
E_XYL	x	x	x	x	x	x	x	x	x	x	x	x	x	x	0/0/1

D

Short-term Air Quality versus WHO Guidelines - Scenarios II and III

Go back to page 48.

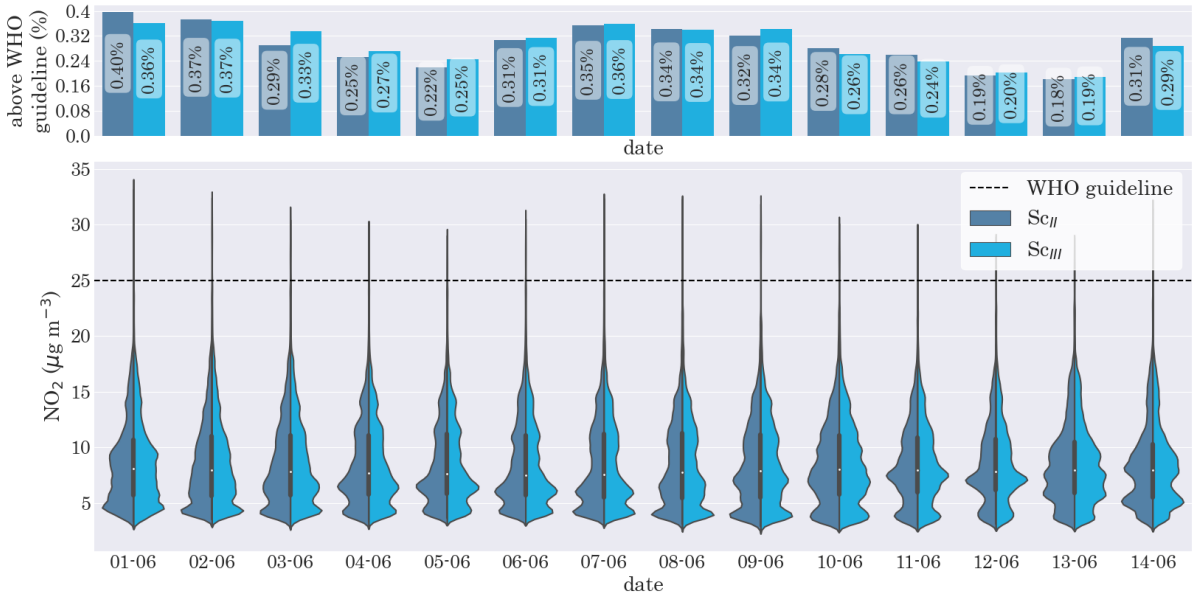

Figure D.1. Time series showing the daily mean NO_2 concentration distribution for the study domain on each day of the simulation, for scenarios II and III. The spatial distribution is shown as kernel density estimate, with a simplified boxplot showing the median value (of two runs combined) as a white dot and the inter-quartile range as a black box. The WHO guideline concentration of 25 μg m^{-3} is indicated as a dashed line. On top the percentage of locations exceeding the WHO guideline concentration is shown for that day.

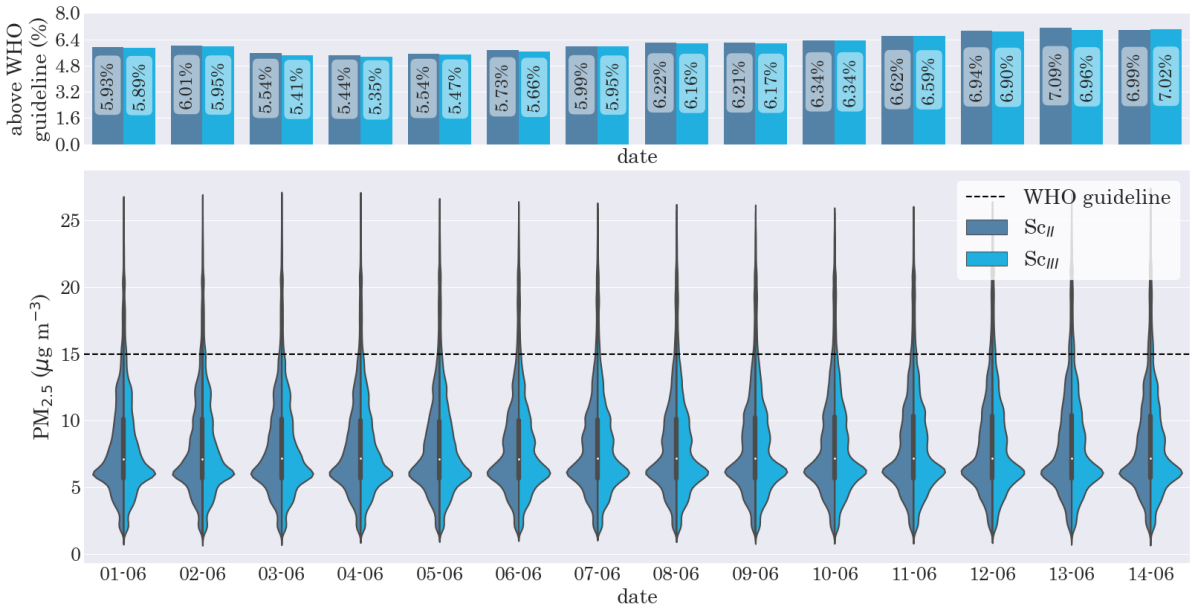

Figure D.2. Time series showing the daily mean $PM_{2.5}$ concentration distribution for the study domain on each day of the simulation, for scenarios II and III. The spatial distribution is shown as kernel density estimate, with a simplified boxplot showing the median value (of two runs combined) as a white dot and the inter-quartile range as a black box. The 24-hour mean WHO guideline concentration of 15 μg m^{-3} is indicated as dashed line.

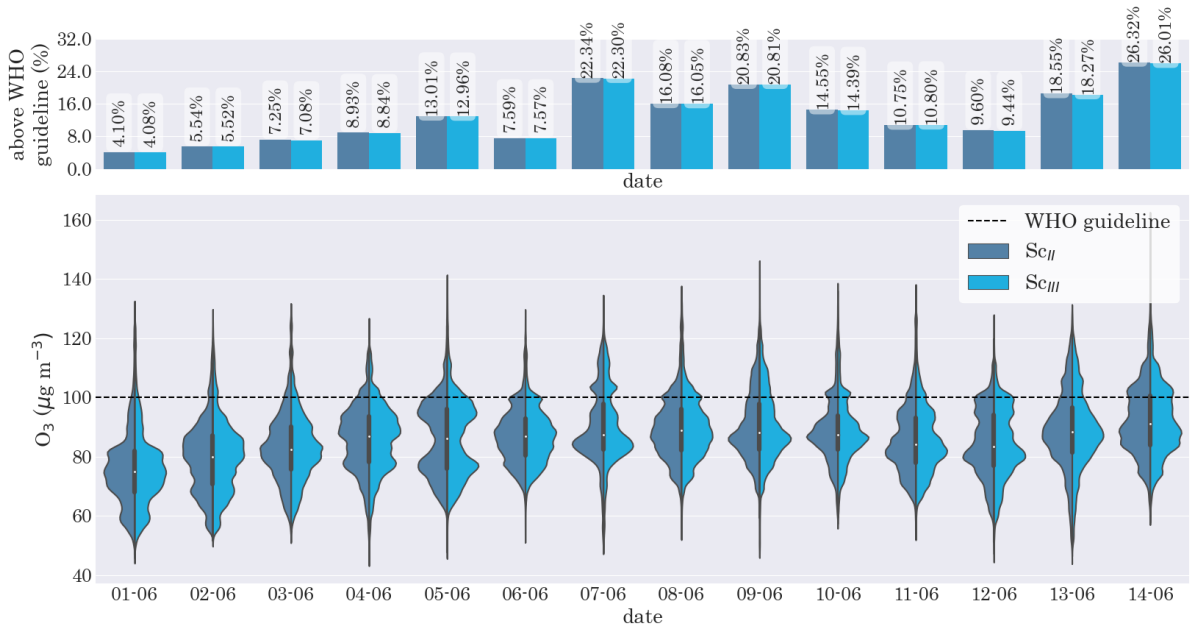

Figure D.3. Time series showing the daily maximum 8-hour mean O_3 concentration distribution for the study domain on each day of the simulation, for scenarios II and III. The spatial distribution is shown as kernel density estimate, with a simplified boxplot showing the median value (of two runs combined) as a white dot and the inter-quartile range as a black box. The WHO guideline concentration of 100 μg m^{-3} is indicated as a dashed line. On top the percentage of locations exceeding the WHO guideline concentration is shown for that day.

E

Changes in Air Quality at Large Airports

Go back to page 51.

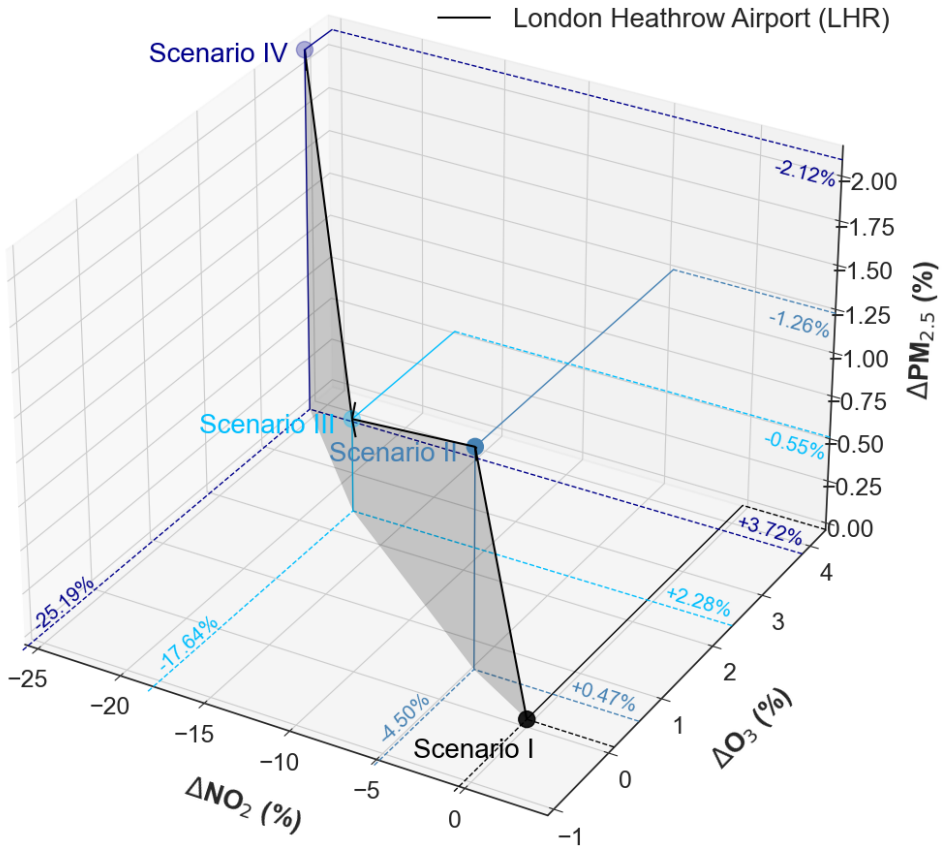

(a)

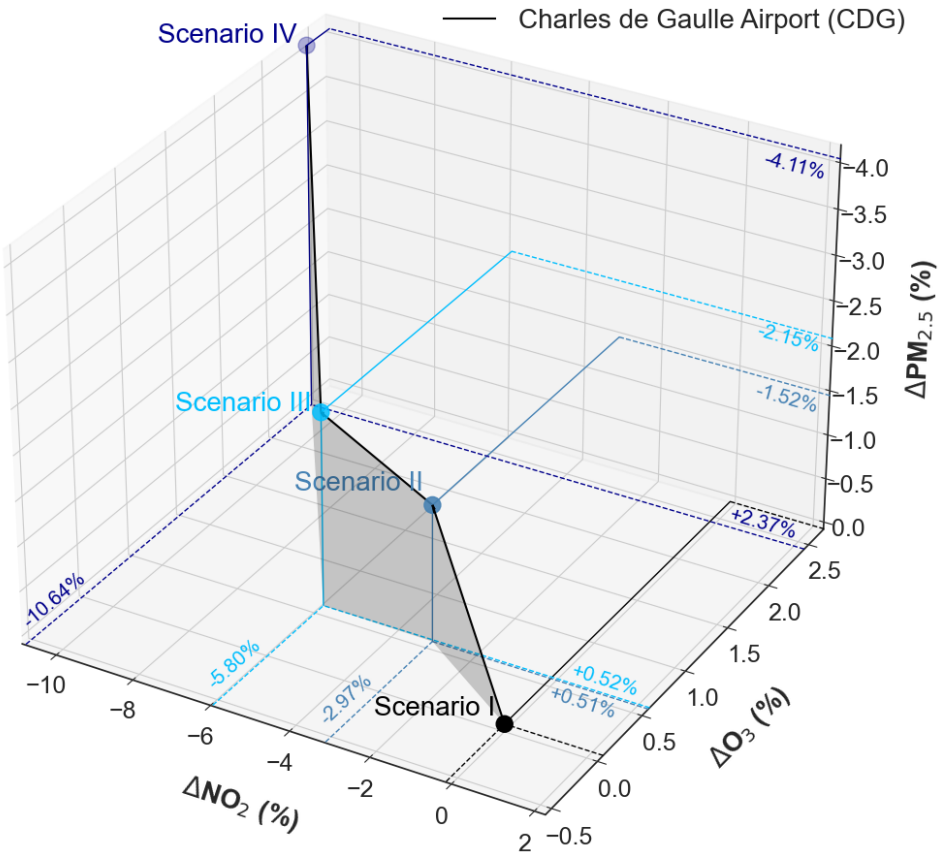

(b)

Figure E.1. cont'd on next page

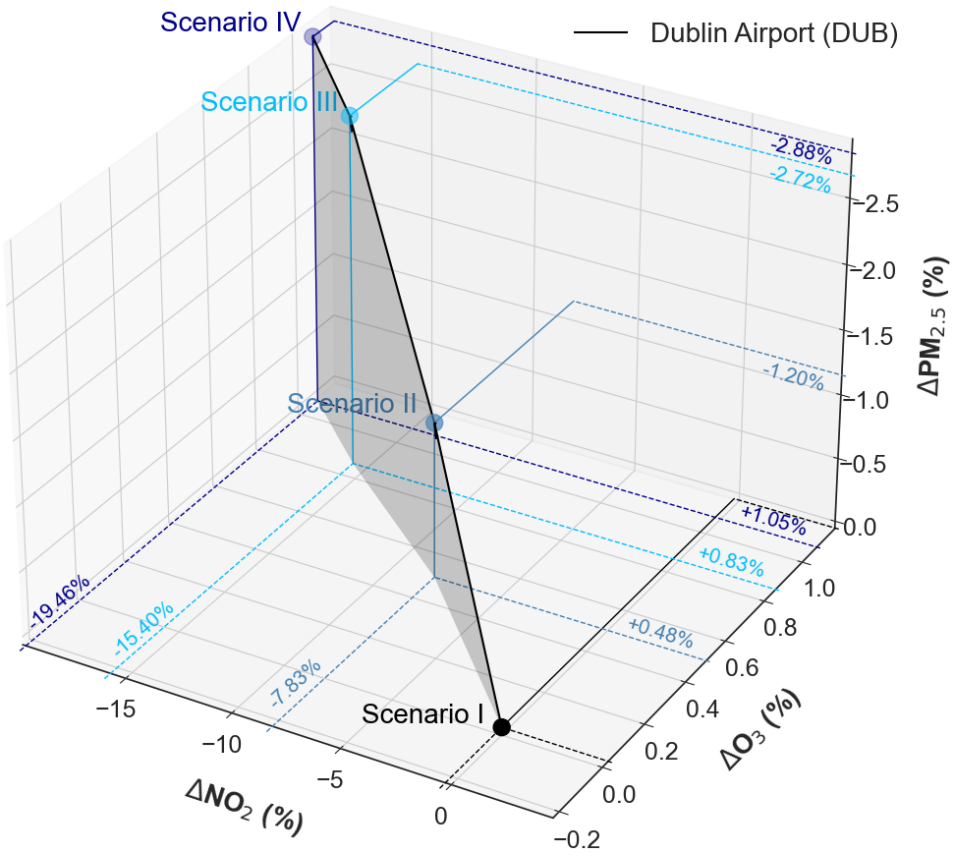

(c)

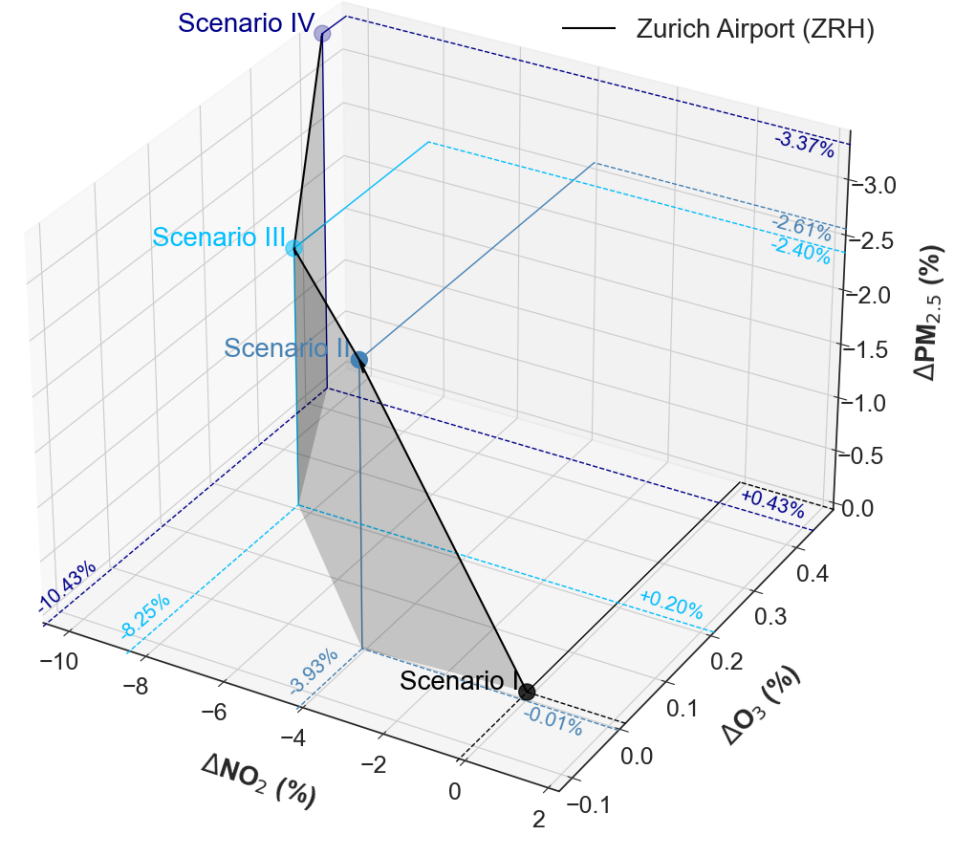

(d)

Figure E.1. cont'd on next page

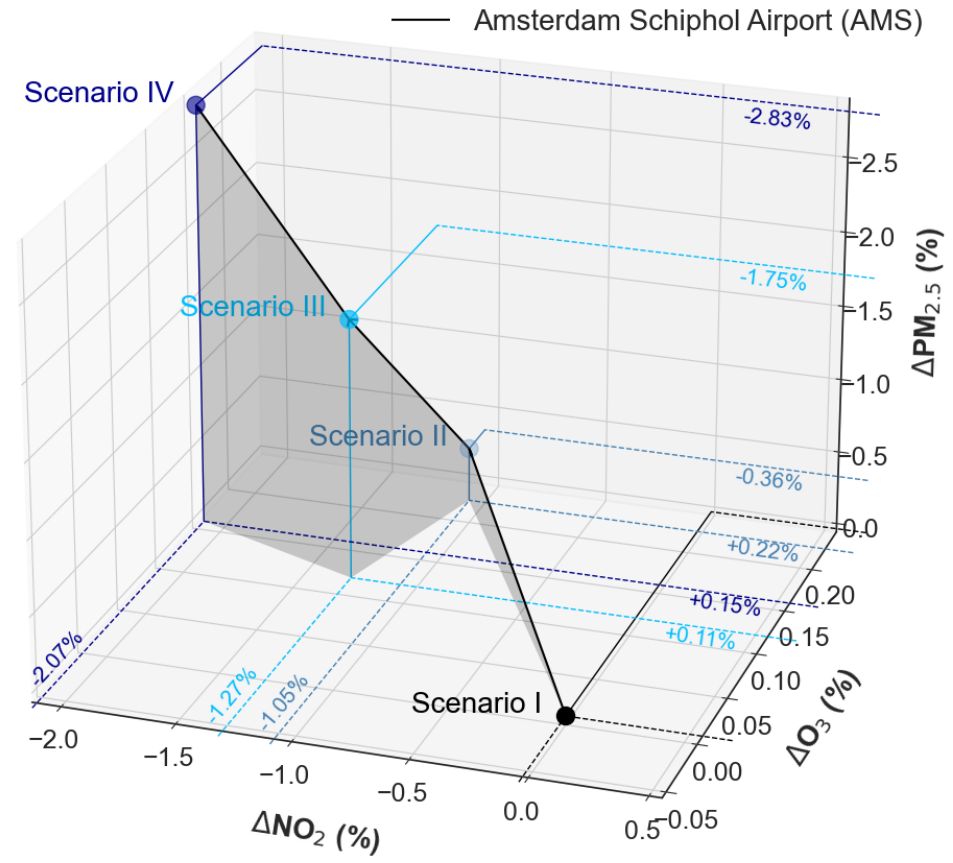

(e)

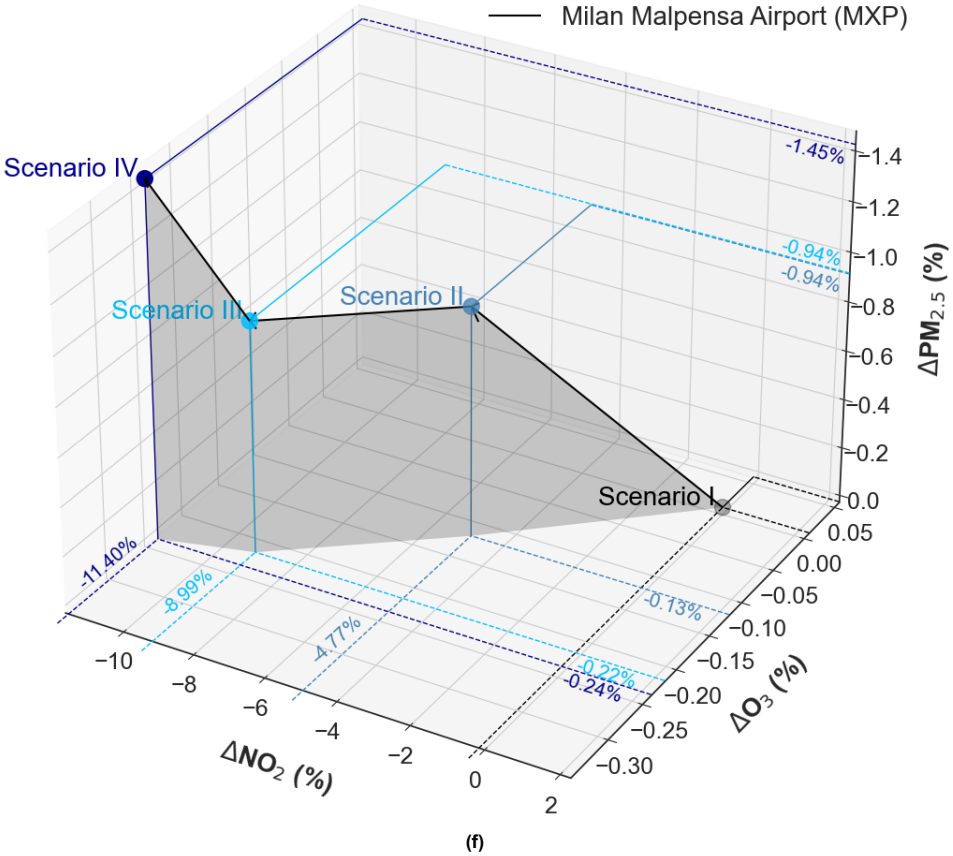

(f)

Figure E.1. cont'd on next page

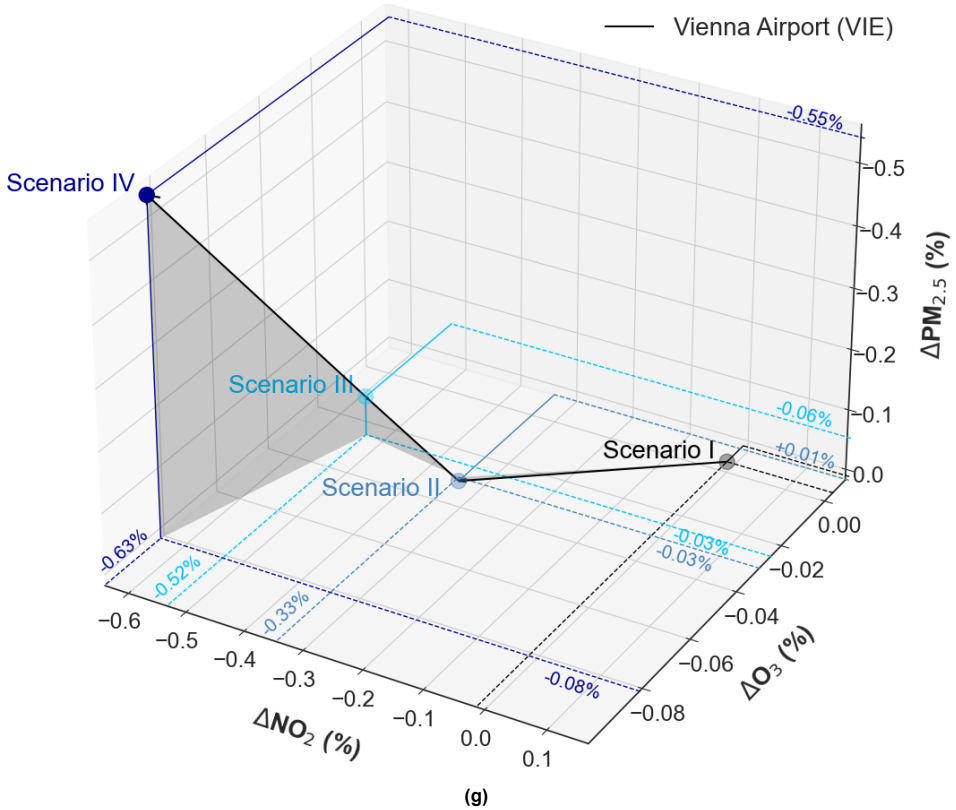

(g)

Figure E.1. Changes in air quality shown for the hydrogen scenarios (scenarios II, III, and IV) at seven of the ten largest airports within the study domain - **(a)** London Heathrow, **(b)** Charles de Gaulle, **(c)** Dublin, **(d)** Zurich, **(e)** Amsterdam Schiphol, **(f)** Milan Malpensa, and **(g)** Vienna Airport.

F

Radius of Airport Pollution Amsterdam Schiphol Airport

Go back to page 56.

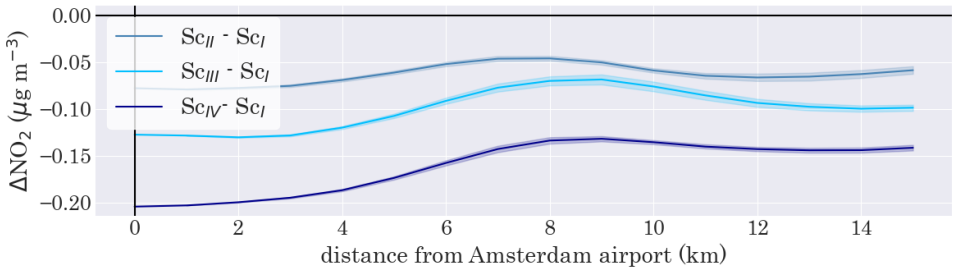

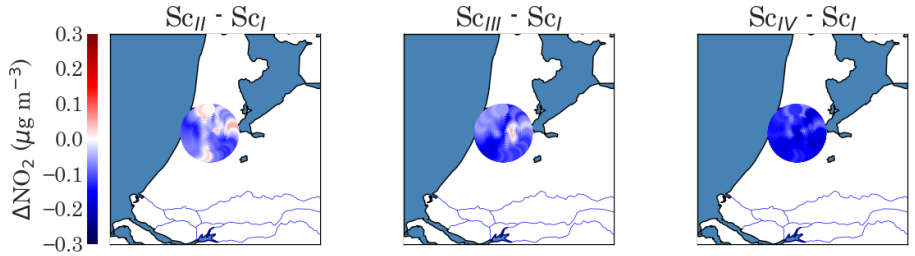

(a) Differences in nitrogen dioxide concentrations.

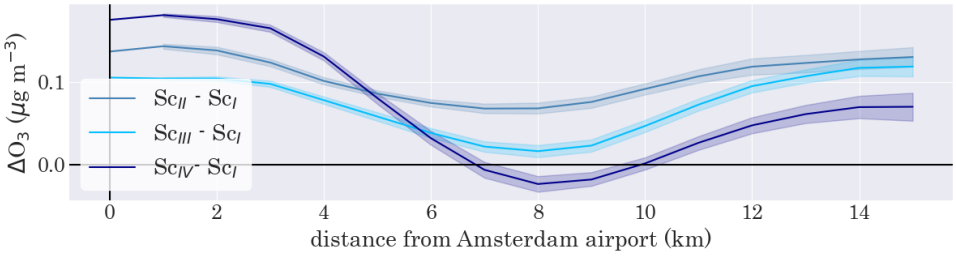

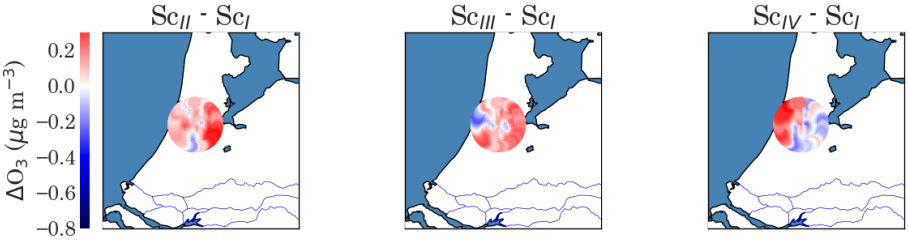

(b) Differences in ozone concentrations.

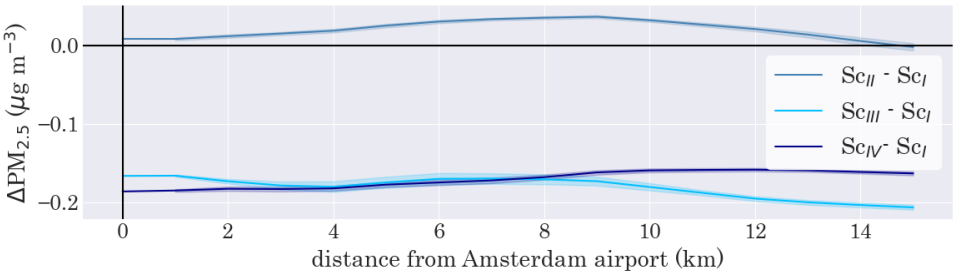

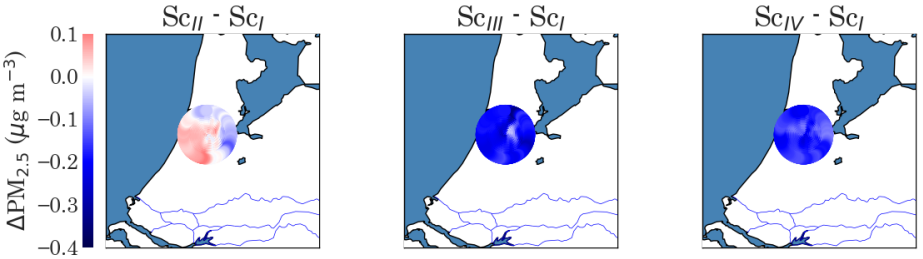

(c) Differences in fine particulate matter concentrations.

Figure F.1. Time-mean changes in air quality around Schiphol Amsterdam Airport, the Netherlands, between different scenarios, taking scenario I as a baseline. Differences in concentration are plotted starting at the airport, moving 15 km away from the airport. Contour plots show absolute differences in concentration, the line plots above show relative differences.

G

Normality Tests Air Quality Change Distribution

Go back to page 56.

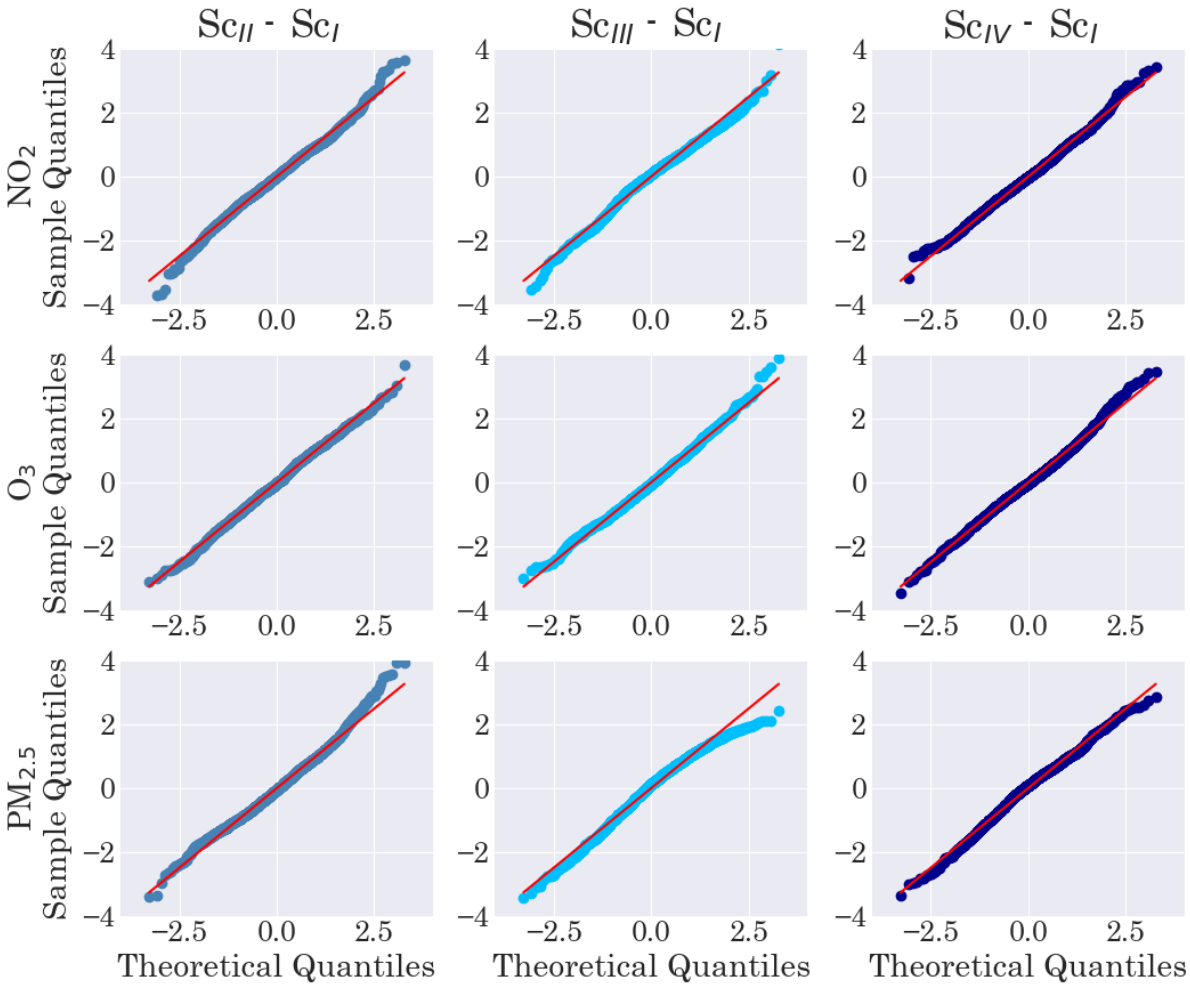

Figure G.1. Quantile-Quantile plots with the theoretical quantiles on the horizontal axis and the data quantiles on the vertical axis. The red $y = x$ lines show a perfect Gaussian distribution. Any deviations from this line indicate non-normality of the real data distribution.

H

AEM Validation

Go back to page 58.

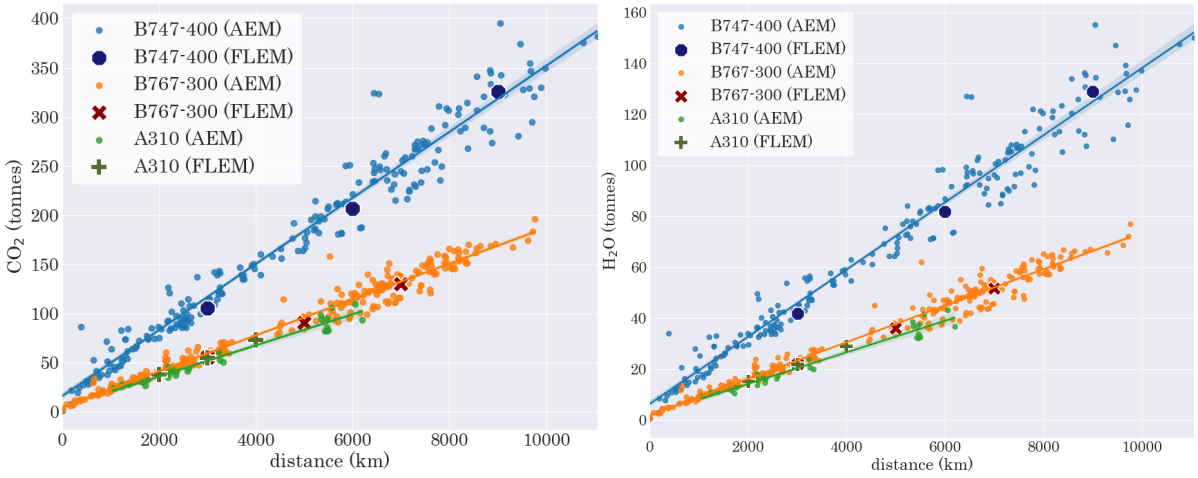

(a) (b)

Figure H.1. Modeled carbon dioxide emissions **(a)** and water vapor emissions **(b)** as a function of distance flown for three aircraft types - B747-400, B767-300, and A310(-200) - shown as small dots. The AEM output is compared with FLEM output (large dots).

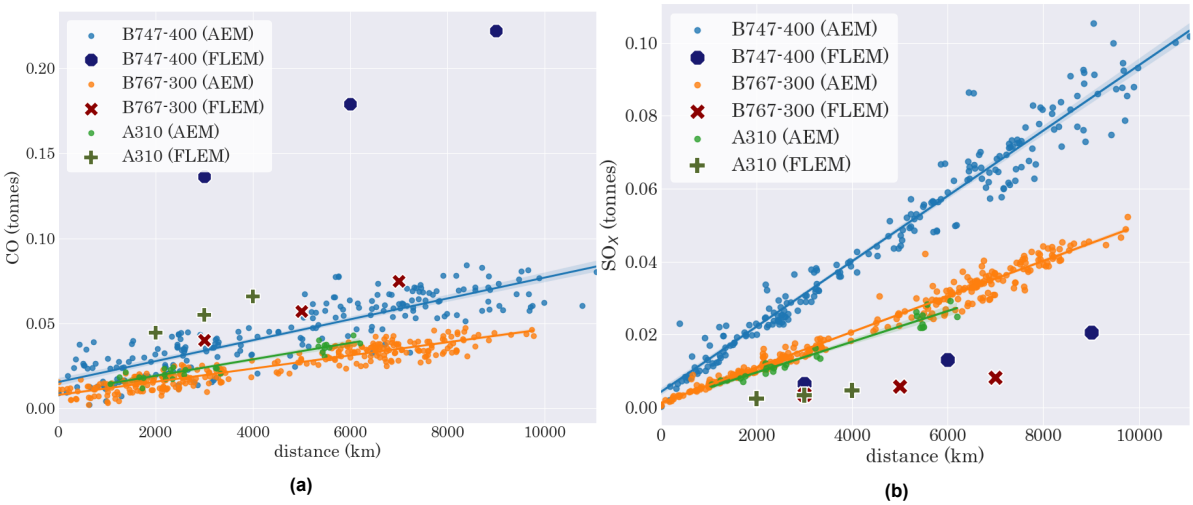

(a) (b)

Figure H.2. Modeled carbon monoxide emissions **(a)** and sulfuric oxides emissions**(b)** as a function of distance flown for three aircraft types - B747-400, B767-300, and A310(-200) - shown as small dots. The AEM output is compared with FLEM output (large dots).

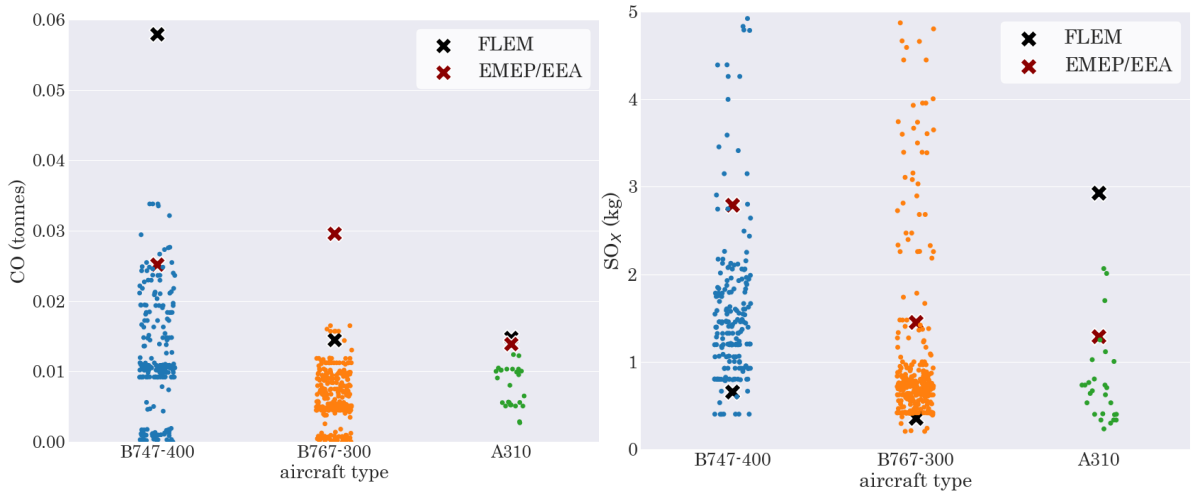

(a) (b)

Figure H.3. Modeled carbon monoxide emissions **(a)** and sulfuric oxides emissions **(b)** for the same three aircraft types during the landing and take-off (LTO) phase. The AEM output (small dots) is compared with FLEM and EMEP/EEA data (large dots). Each individual flight from the AEM output is represented by a blue, orange or green dot.

Comparison Model Output with RIVM/DCMR Measurements

Go back to page 60.

Table I.1. Rural background measurement sites shown in Figure 6.3. The measured variables at each respective site is shown.

Station	NO_2	O_3	$PM_{2.5}$	Wind speed	Wind direction
Amsterdam-Spaarnwoude	X		X	X	X
Badhoevedorp-Sloterweg	X		X	X	X
Balk-Trophornsterweg	X	X		X	X
Barsbeek-De Veenen	X	X		X	X
Biest Houtakker-Biestsestraat	X	X	X	X	X
Cabauw-Wielsekade	X	X	X	X	X
De Zilk-Vogelaarsdreef	X	X	X	X	X
Eibergen-Lintveldseweg	X	X		X	X
Fijnaart-Zwingelspaansedijk	X			X	X
Hellendoorn-Luttenbergerweg	X	X		X	X
Hoofddorp-Hoofdweg	X			X	X
Huijbergen-Vennekenstraat	X	X		X	X
Kollumerwaard-Hooge Zuidwal	X		X	X	X
Oude Meer-Aalsmeerderdijk	X			X	X
Philippine-Stelleweg	X			X	X
Posterholt-Vlodropperweg	X	X		X	X
Valthermond-Noorderdiep	X	X		X	X
Vredepeel-Vredeweg	X	X	X	X	X
Wekerom-Riemterdijk	X	X	X	X	X
Westmaas-Groeneweg	X	X		X	X
Wieringerwerf-Medemblikkerweg	X	X	X	X	X
Zegveld-Oude Meije	X	X		X	X
Zierikzee-Lange Slikweg	X	X		X	X

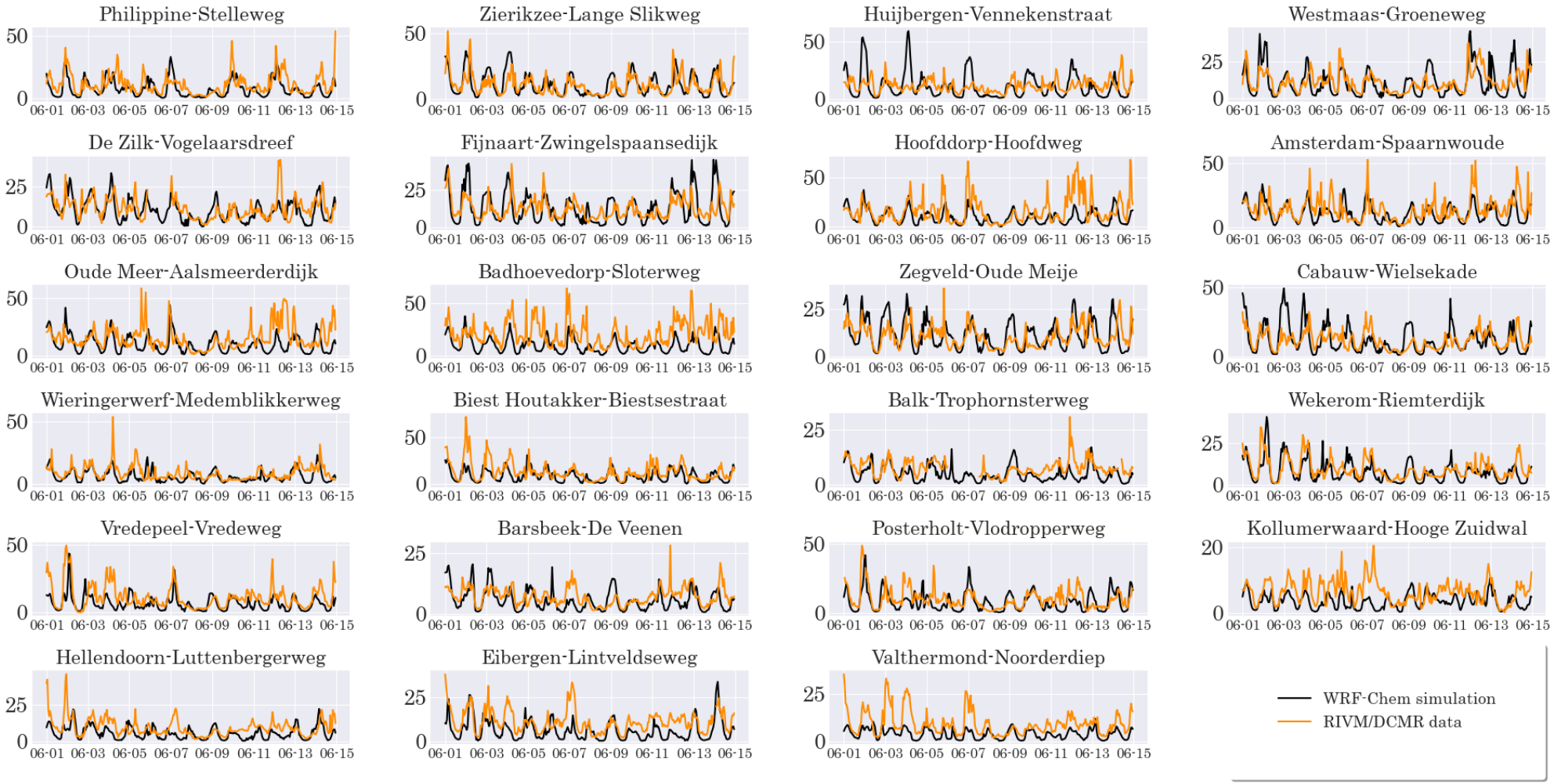

Figure I.1. Nitrogen dioxide (NO_2) concentrations ($\mu g\ m^{-3}$) shown at 23 measurement sites from the WRF-Chem output. At all the sites the NO_2 concentrations are measured. The time series span the first two weeks of June 2019. Measurement data is retrieved from RIVM, DCMR and others [2021].

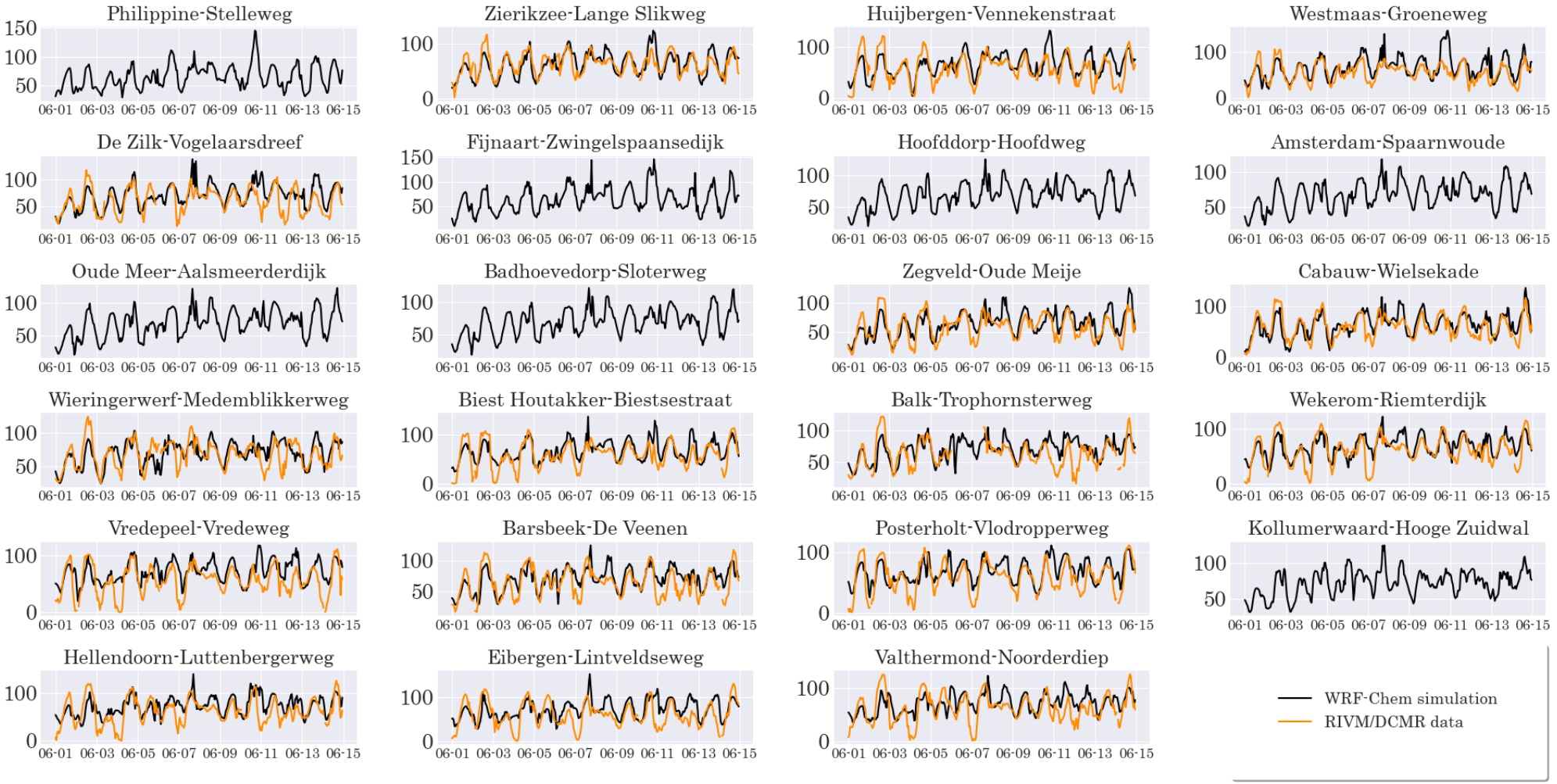

Figure I.2. Ozone (O_3) concentrations ($\mu g\ m^{-3}$) shown at 23 measurement sites from the WRF-Chem output. At 16 sites the O_3 concentrations are measured. The time series span the first two weeks of June 2019. Measurement data is retrieved from RIVM, DCMR and others [2021].

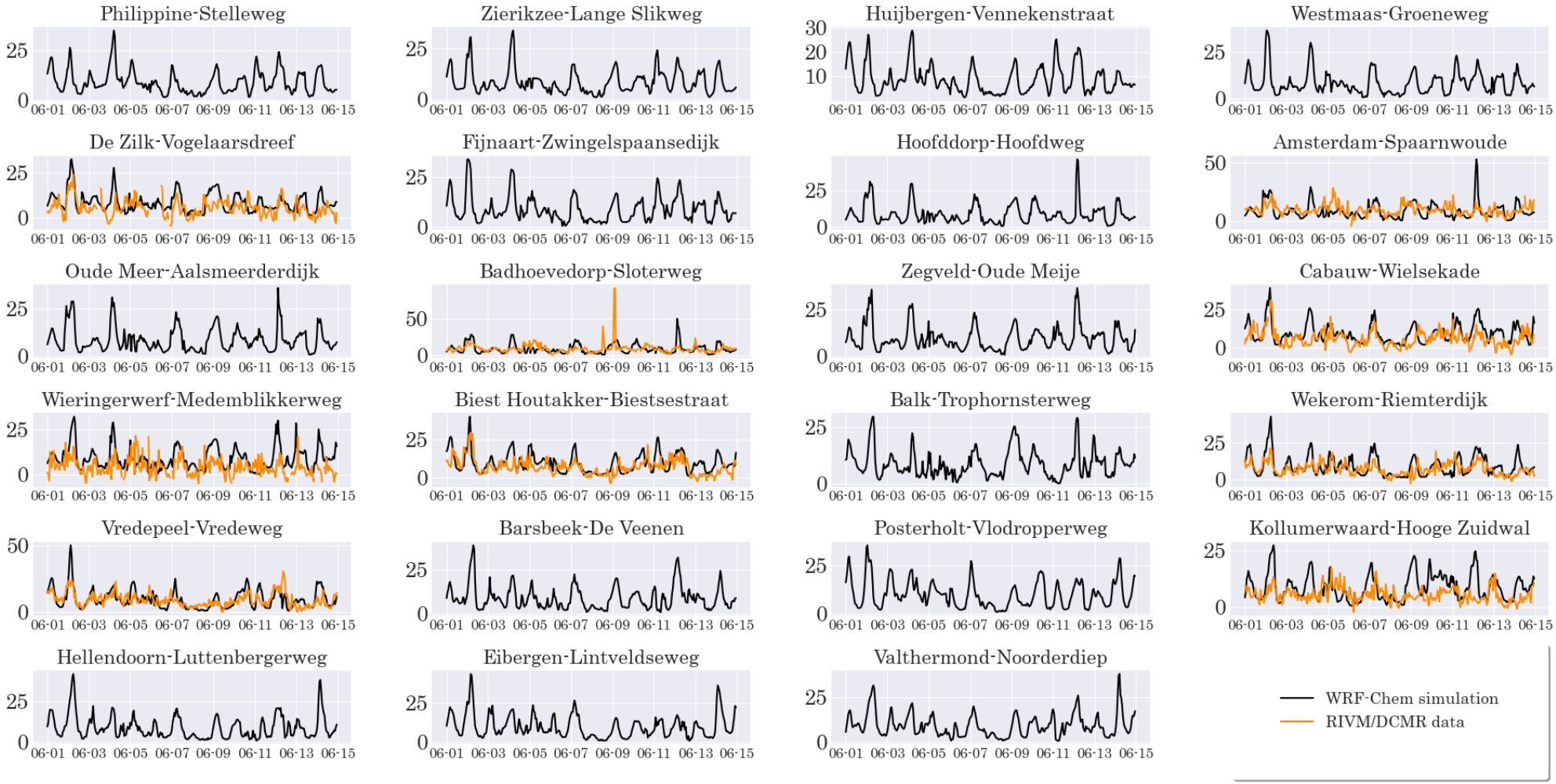

Figure I.3. Fine particulate matter ($PM_{2.5}$) concentrations ($\mu g\ m^{-3}$) shown at 23 measurement sites from the WRF-Chem output. At 9 sites the $PM_{2.5}$ concentrations are measured. The time series span the first two weeks of June 2019. Measurement data is retrieved from RIVM, DCMR and others [2021].

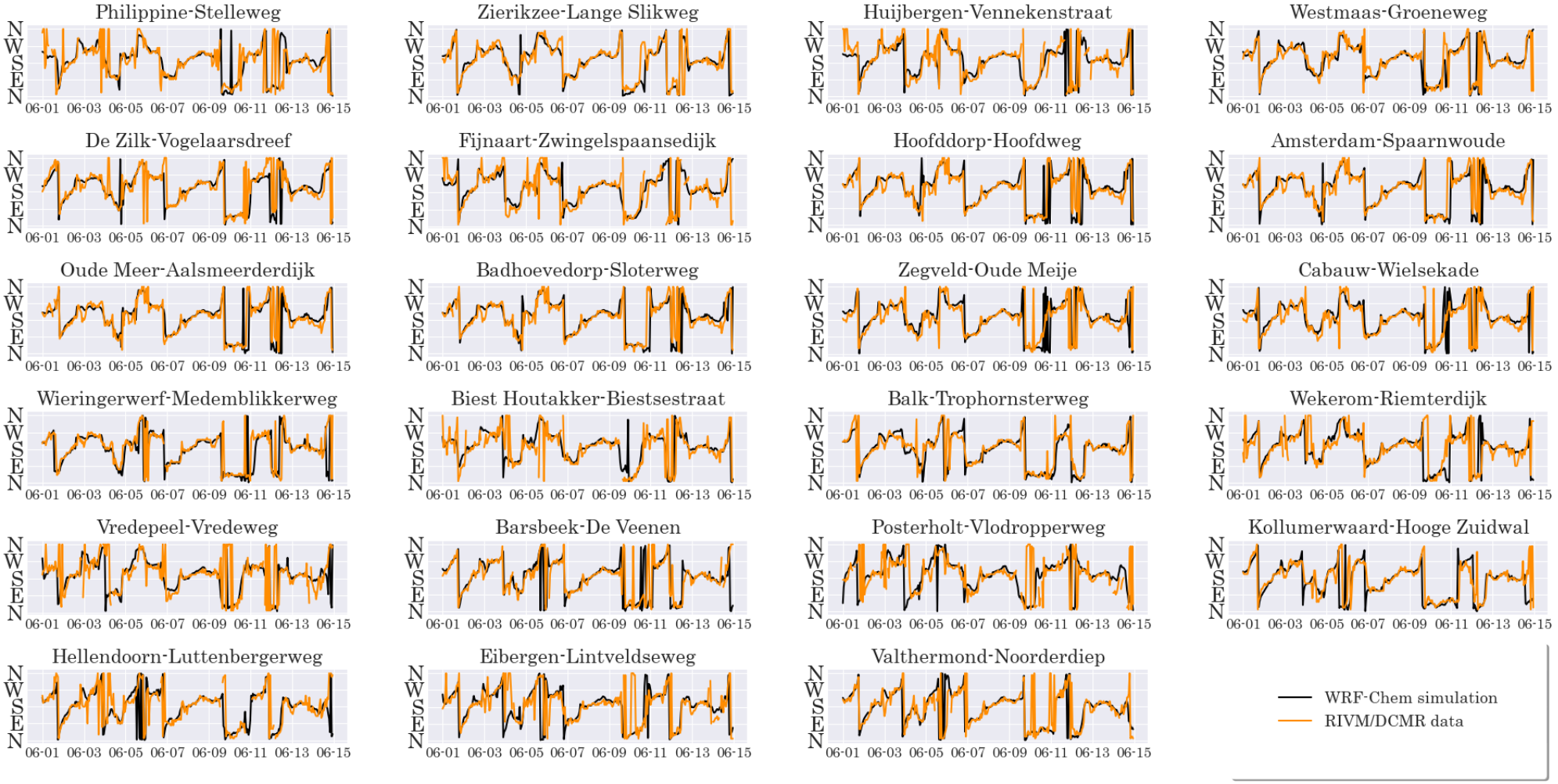

Figure I.4. Wind direction (°) shown at 23 measurement sites, compared between WRF-Chem model output and observations. At all 23 locations the wind direction is measured. The time series span the first two weeks of June 2019. Measurement data is retrieved from RIVM, DCMR and others [2021].

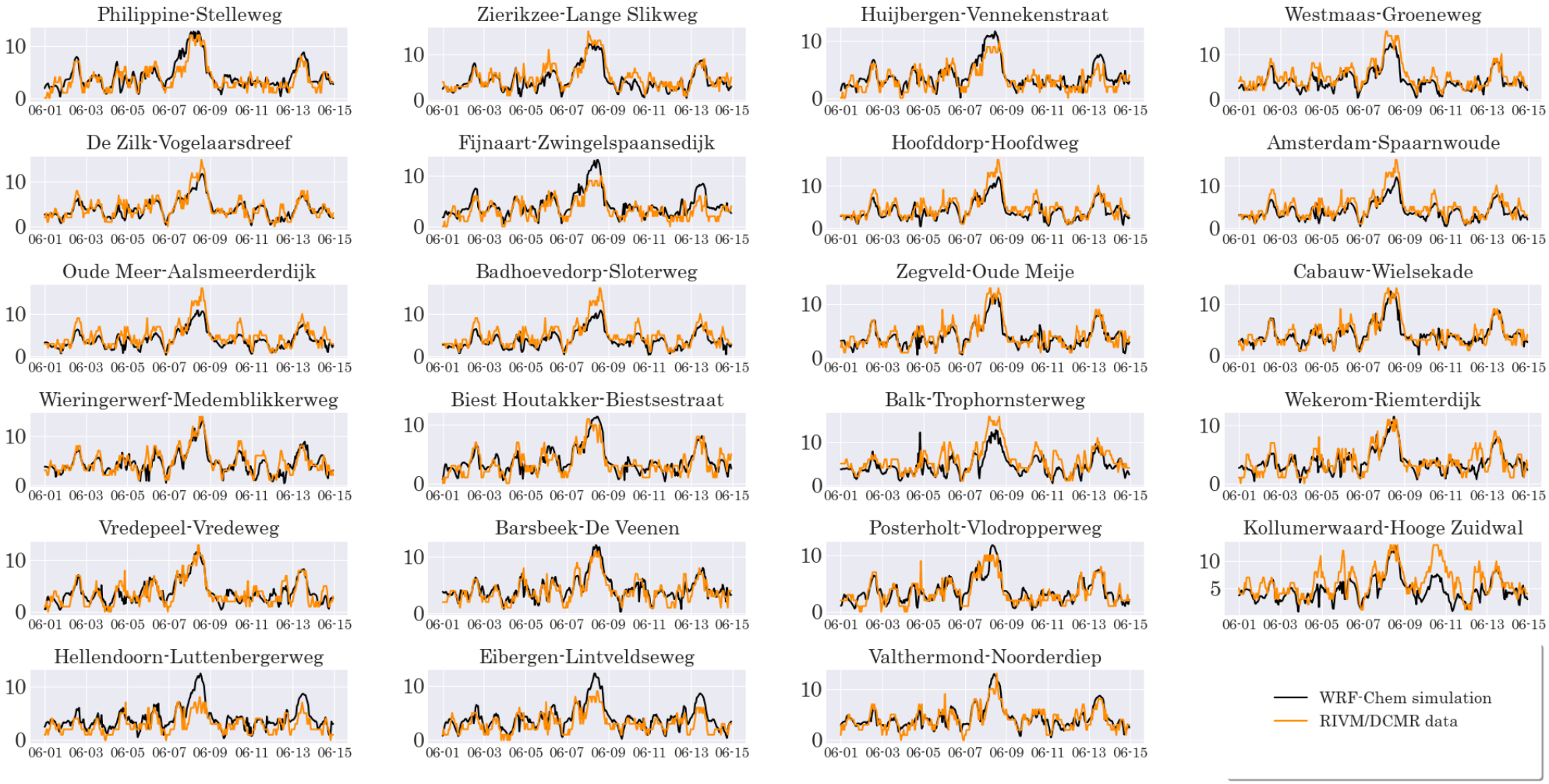

Figure I.5. Wind speed (m/s) shown at 23 measurement sites, compared between WRF-Chem model output and observations. At all 23 locations the wind speed is measured. The time series span the first two weeks of June 2019. Measurement data is retrieved from RIVM, DCMR and others [2021].